

ISSN 0288-4534  
CODEN:KONAE7

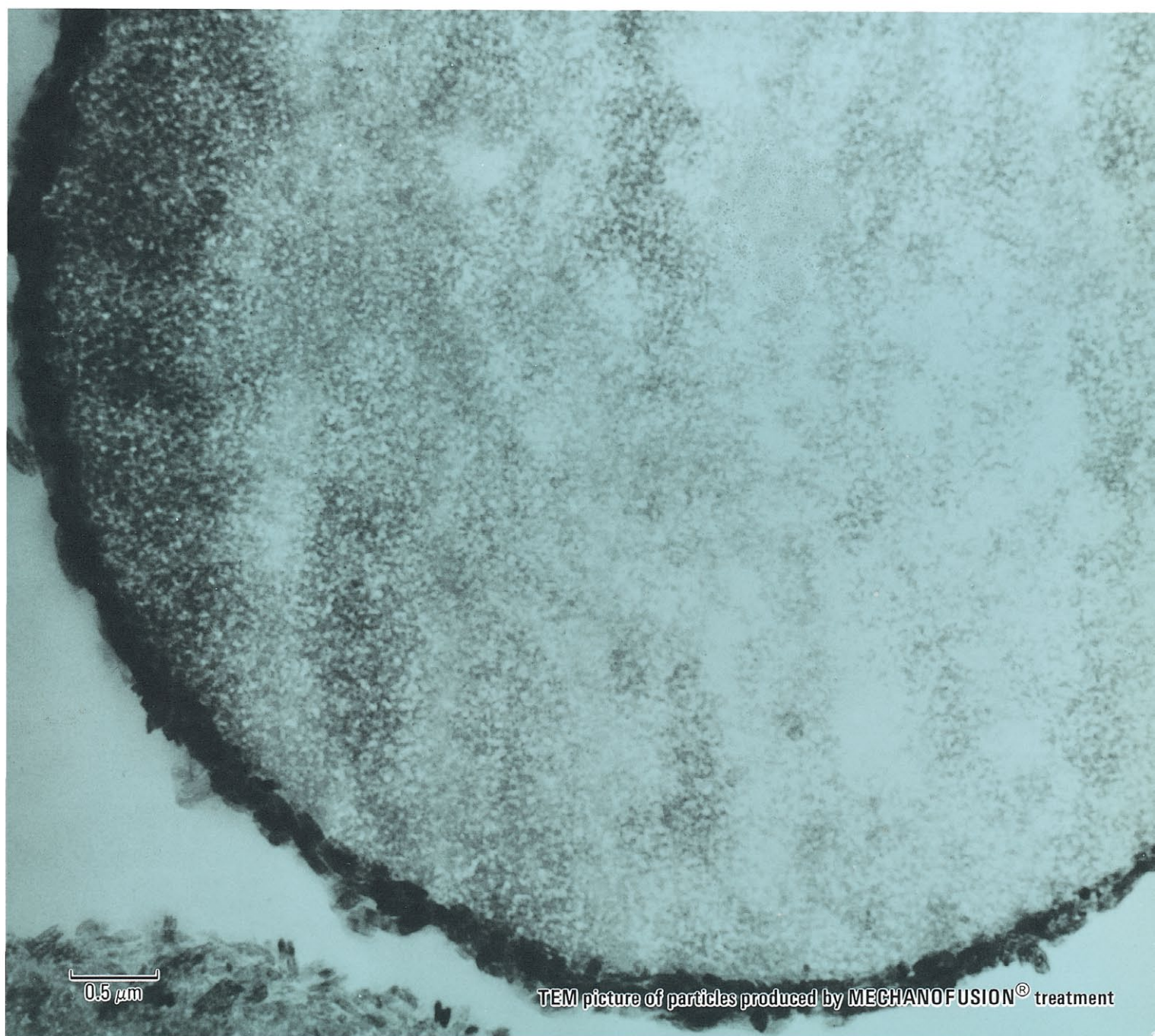
粉

# KONA

POWDER SCIENCE AND  
TECHNOLOGY IN JAPAN

## NO. 5 (1987)

Published by The Party of Powder Technology (JAPAN)



0.5 μm

TEM picture of particles produced by MECHANOFUSION® treatment

KONA is aimed, as its subtitle indicates, to introduce annually the recent works on powder science and technology in Japan to the interested parties in the world. It consists of the English version of reports and reviews carefully selected out of the latest papers which were originally written in Japanese.

KONA is distributed without charge to senior researchers, institutions and libraries in this field throughout the world under the sponsorship of Hosokawa Micron Corporation. Within these limits the editors are always glad to consider the addition of names to the mailing list.

#### Explanation of the Cover

“粉”; This Chinese character is pronounced as “KONA” in Japanese and means “Powder”.  
“粉” on the front page was written by the late Mr. Eiichi Hosokawa, founder of Hosokawa Micron Corporation.

#### Editorial Board

<b>Naoya Yoshioka</b>	(Professor of Okayama University of Science) Editor in Chief.
<b>Masafumi Arakawa</b>	(Professor of Kyoto Institute of Technology)
<b>Masuo Hosokawa</b>	(President of Hosokawa Micron Corp.)
<b>Koichi Iinoya</b>	(Professor of Aichi Institute of Technology)
<b>Genji Jimbo</b>	(Professor of Nagoya University)
<b>Yasuo Kousaka</b>	(Professor of University of Osaka Prefecture)
<b>Kei Miyanami</b>	(Professor of University of Osaka Prefecture)
<b>Takeo Yano</b>	(Professor Emeritus of University of Osaka Prefecture)
<b>Tetsuo Yoshida</b>	(Technical Director of Hosokawa Micron Corp.)
<b>Tohei Yokoyama</b>	(Director of Hosokawa Micromeritics Laboratory)

#### Editorial Assistants

<b>Teruaki Suzuki</b>	(Hosokawa Micron Corp.)
<b>Fumio Nakagawa</b>	(Hosokawa Micron Corp.)
<b>Minako Matsui</b>	(Hosokawa Micron Corp.)



Hosokawa Micron Corporation and its R&D Center

**Publication Office and Owner of Copyright**

**The Party of Powder Technology (Japan)**  
in **Hosokawa Micron Corporation**

No.9, 1-chome, Shoudai Tajika, Hirakata-shi, Osaka 573 Japan

(Complimentary Copy)

Printed in Japan



## Contents

### < Original Report >

The Aerosol Classification Performance of a Rectangular Jet Virtual-Impactor	<i>Hiroaki Masuda, Eiji Yasuki and Satoshi Kawaguchi</i> . . . . .	2
A Technique for Measuring Broad Size Ranges of Aerosol Particles by the Laser Beam Scattering Method Combined with Condensation Nuclei	<i>Satoshi Okuda, Hiroshi Takano and Takeshi Iwamoto</i> . . . . .	10
The Submicron Grinding of BaTiO <sub>3</sub> by Ball Milling	<i>Kenji Tanaka, Kiichi Minai, Kikuo Wakino and Isao Uei</i> . . . . .	18
The Spontaneous Ignition of Dust Deposits –Ignition Temperature and Induction Time –	<i>Hua Liang and Tatsuo Tanaka</i> . . . . .	25
Mechano-chemical Effects of One-dimensional Explosive Shock Treatment on the Characteristics of Si <sub>3</sub> N <sub>4</sub>	<i>Fumikazu Ikazaki, Kunio Kamiya, Kunio Uchida, Akihiro Goto, Mitsutaka Kawamura, Katsumi Tanaka and Shuzo Fujiwara</i> . . . . .	33
The Visualization of Flow Patterns on a Sphere in a Packed Bed	<i>Yutaka Tsuji, Yoshinobu Morikawa, Masahiko Nakao and Naoyuki Nakatsukasa</i> . .	43
 < Review >		
Particle-precipitation Aided CVD	<i>Hiroshi Komiyama and Hisatsugu Kaji</i> . . . . .	50
The Mechanofusion System and Its Applications	<i>Tohei Yokoyama, Kiyoshi Urayama, Makio Naito, Masashi Kato and Toyokazu Yokoyama</i> . . . . .	59
Spherical Crystallization as a Novel Particle Design Technique for the Development of Pharmaceutical Preparations	<i>Yoshiaki Kawashima</i> . . . . .	69
The Evaluation of Activity and Reactivity of Mechanically Treated Fine Powdered Materials	<i>Mamoru Senna</i> . . . . .	76
Information Articles . . . . .		82

# The Aerosol Classification Performance of A Rectangular Jet Virtual-Impactor<sup>†</sup>

Hiroaki Masuda, Eiji Yasuki  
and Satoshi Kawaguchi

Department of Chemical Engineering  
Hiroshima University\*

## Abstract

*The aerosol classification performance of a newly constructed rectangular jet virtual-impactor has been studied both theoretically and experimentally. It is found that the performance is well represented by potential flow calculations with modifications for the effects of the acceleration jet and flow separation at the slit. The sharpness of the classification is not as good as that of a round jet impactor, and the variable range of the cut size is smaller. In the rectangular jet impactor, however, a higher flow rate of aerosol can be treated without changing the cut size. It is also found that higher degrees of sharpness are obtained and that the cut size is variable within a certain range by introducing clean air flows as in the round jet impactor previously developed by the authors. The separation characteristic is found to be well explained by assuming perfect mixing between the aerosol flow and the clean-air flows at both ends of the rectangular jet. The maximum inertia parameter limited by the sound velocity is also discussed, and an empirical equation representing the pressure drop of the impactor is presented.*

## Introduction

Particles rebound or will be reentrained by air flow when a collision type impactor is used for the measurement of particle size or for the classification of fine particles. To avoid these phenomena, a virtual-impactor (hereinafter, referred to as “V. impactor” or only “impactor”) has been developed, and its classification mechanism has been studied<sup>1,4,7).</sup>

The disadvantage of the V. impactor is that the separation efficiency cannot be lowered to less than the ratio of the undeflected flow rate

over the total flow rate, even if it is assumed that fine particles possess zero inertia. We have studied and shown that the efficiency of the impactor can be improved by introducing clean air into the core and sheath of the aerosol flow, and the 50% cut size and gradient of the separation efficiency curve can be adjusted within a specific range<sup>5).</sup> Moreover, we have shown that testing aerosols possessing relatively uniform particle sizes can be generated using the two-stage type V. impactor<sup>6).</sup> All of the impactors tested are of the round jet type.

The round jet virtual impactor, however, has an inherent disadvantage in that it cannot be scaled-up while maintaining constant classification performance parameters. Consequently, the quantity being treated cannot be increased. In this study, a rectangular jet impactor was constructed and its classification performance was investigated both theoretically and experimentally using mono-disperse aerosol particles.

\* Shitami, Saijo, Higashi-Hiroshima, Hiroshima, 724  
TEL. 0824 (22) 7111

† This report was originally printed in *Kagaku Kogaku Ronbun-shu*, 10, 561-567 (1984) in Japanese, before being translated into English with the permission of the editorial committee of the Soc. Chemical Engineers, Japan.



## 2. Impactor configuration and theoretical calculation

### 2.1 Impactor configuration, and separation efficiency when introducing clean air

Figure 1 shows the outline of the constructed rectangular jet impactor. The total length of the brass-made impactor is approx. 20 cm. The jet (4) (width: 1 mm, length: 10 mm) is positioned facing the nozzle (5) in the slit, and particles are classified there. The impactor is designed so that aerosol is introduced through (1) and clean air through (2) and (3). The aerosol and air are then accelerated by the jet (4). Particles are classified according to their aerodynamic diameters, as coarser aerosol having larger inertia discharges through (7) and finer aerosol having smaller inertia discharges through (6). The slit gap between the acceleration jet (4) and the collection nozzle (5) can be adjusted using the adjustment screw (8) and the spacer (10). Two flow laminators are positioned in the laminator (9), each with six 3 mm inner diameter holes, which streamline the clean air flow.

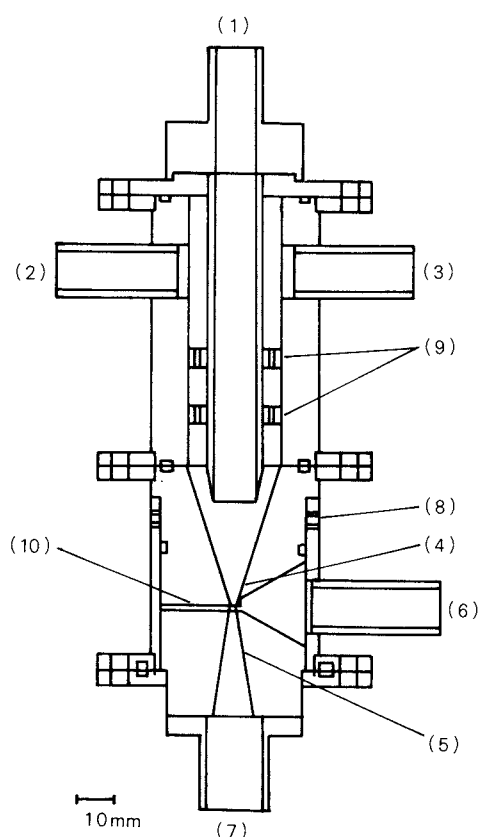


Fig. 1 Rectangular jet virtual-impactor

Figure 2 illustrates a schematic diagram of the aerosol classification mechanism of the rectangular jet impactor when clean air is introduced. Mono-disperse aerosol particles accelerated by the jet are separated to the right and left of the critical particle trajectory illustrated by the broken line. The separation efficiency  $\eta$  is given as follows :

$$\eta = \frac{\int_0^{B_c} l \cdot u \cdot n \cdot dx}{\int_0^B l \cdot u \cdot n \cdot dx} \quad (1)$$

If the number concentration of aerosol particles  $n(x)$  satisfies the following equation in the  $x$  direction of the jet width;

$$n(x) = \begin{cases} 0 & : 0 \leq x < B_a \\ \text{const} & : B_a \leq x \leq B_b \\ 0 & : B_b < x \leq B \end{cases} \quad (2)$$

When the critical particle trajectory is within the right or left of the clean air flow, the first and third equations of Eq. (2) give the separation efficiency as follows;

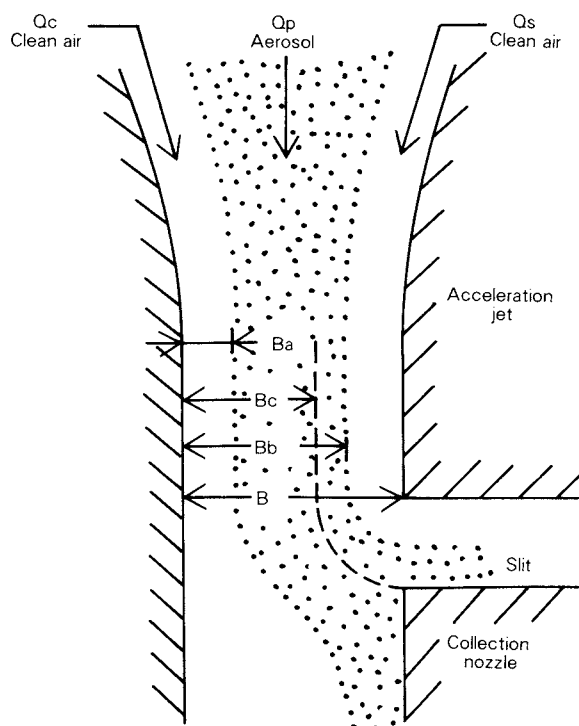


Fig. 2 Schematic diagram of aerosol flow

$$\eta = 0 \text{ for } 0 \leq B_c < B_a \quad (3)$$

$$\eta = 1 \text{ for } B_b < B_c \leq B \quad (4)$$

On the other hand, when the critical particle trajectory is within the aerosol flow as shown in Fig. 2, the second equation of Eq. (2) gives,

$$\eta = \frac{\int_{B_a}^{B_c} u dx}{\int_{B_a}^{B_b} u dx} \text{ for } B_a \leq B_c \leq B_b \quad (5)$$

assuming that  $n(x)$  does not change in the direction of the jet length  $l$ . Eq. (5) is rewritten as follows;

$$\begin{aligned} \eta &= \frac{\int_0^{B_c} u dx}{\int_{B_a}^{B_b} u dx} - \frac{\int_0^{B_a} u dx}{\int_{B_a}^{B_b} u dx} \\ &= \frac{\int_0^B u dx}{\int_{B_a}^{B_b} u dx} \cdot \frac{\int_0^{B_c} u dx}{\int_0^B u dx} - \frac{\int_0^{B_a} u dx}{\int_{B_a}^{B_b} u dx} \end{aligned} \quad (6)$$

where

$$l \cdot \int_0^B u dx = Q_t, \quad l \cdot \int_{B_a}^{B_b} u dx = Q_p, \quad l \cdot \int_0^{B_a} u dx = Q_c$$

The number of particles that flow on the left side of the critical particle trajectory are collected in the collection nozzle. If the flow rate is denoted by  $Q_x$ , Eq. (6) is represented by:

$$\eta = \frac{Q_t}{Q_p} \cdot \frac{Q_x}{Q_t} - \frac{Q_c}{Q_p} \quad (7)$$

where  $Q_x/Q_t$  is the separation efficiency  $\eta_0$  wherein clean air is not introduced. When flow rate ratios  $\alpha$  and  $\beta$  are defined by the flowing equations,

$$\alpha = \frac{Q_t}{Q_p}, \quad \beta = \frac{Q_c}{Q_p} \quad (8)$$

Eq. (7) reads:

$$\eta = \alpha \eta_0 - \beta \quad (9)$$

Eq. (9) suggests that the impactor may have a sharp classification performance by selecting appropriate flow rate ratios  $\alpha$  and  $\beta$ .

## 2. 2 Numerical analysis of separation efficiency $\eta_0$

This section describes separation efficiency  $\eta_0$  when clean air is not introduced. Using the finite difference method described in the previous report<sup>7)</sup>, separation efficiency was obtained by assuming that the air flow was represented by a potential flow. The flow in the impactor is, however, two-dimensional and therefore, the dimensionless stream function  $\bar{\varphi}$  shown below was used:

$$\frac{\partial^2 \bar{\varphi}}{\partial \bar{x}^2} + \frac{\partial^2 \bar{\varphi}}{\partial \bar{y}^2} = 0 \quad (10)$$

The dimensionless velocity components in the  $x$  direction (right angle to the flow direction) and in the  $y$  direction (flow direction) are given by:

$$\bar{u}_x = \frac{\partial \bar{\varphi}}{\partial \bar{y}}, \quad \bar{u}_y = -\frac{\partial \bar{\varphi}}{\partial \bar{x}} \quad (11)$$

The area including the jet acceleration zone was divided into 1180 triangular elements (number of nodes: 660) and was numerically calculated by the finite element method. (Details of the calculation are omitted.) The approximation analysis, obtained by using the same method as in a previous report<sup>6)</sup>, and the numerical analysis of the acceleration jet effect satisfactorily coincided. This coincidence suggests that the effect of the acceleration jet deflects the particles toward the center line. This effect is caused by particle inertia at the converging zone where the particles enter from the inversed triangle acceleration zone to the straight flow channel. The inversed triangle acceleration zone and straight flow channel are smoothly connected by a curvature radius of 10 mm. If it is assumed that the mean air velocity in the jet is  $u_c$ , the deviation  $\delta$  of the particle trajectory at the jet inlet can be approximated using the following equation:

$$\delta = \tau u_c \tan \theta \quad (12)$$

where  $\tau$  is the particle relaxation time, and  $\theta$  is the half angle (20 deg.) of the converging zone of acceleration jet. The air flow on both sides  $\delta$ , given by Eq. (12) in the straight flow channel (width  $B$ ), does not include aerosol particles. Therefore, by permitting the separation

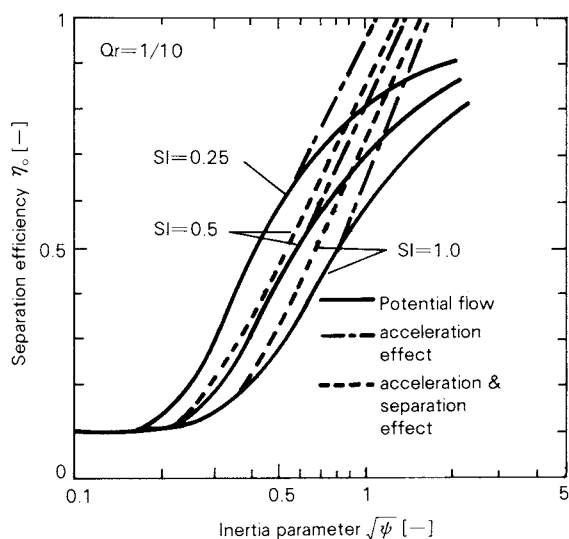


Fig. 3 Calculated separation efficiencies

efficiency to be  $\eta_0'$  when not affected by the acceleration jet, and to be  $\eta_0$  where there is acceleration jet, the following equation is obtained:

$$\eta_0 = \frac{B_c - \delta}{B - 2\delta} = \frac{\eta_0' - \bar{\delta}}{1 - 2\bar{\delta}} \quad (13)$$

where  $\bar{\delta}$  is a dimensionless deviation defined by:

$$\bar{\delta} = \frac{\delta}{B} = \frac{u_c}{u_0} \psi \tan \theta \quad (14)$$

$\psi$  is the particle inertia parameter. Since the flow separates from the lower edge of the jet when the flow enters from the jet to the slit<sup>2,3,7)</sup>, this effect should be considered. In this study, the flow separation effect using an enlarged transparent model was observed, and a numerical analysis was done assuming the interface to be a rigid wall. However, since the flow separation effect can be ignored when the slit width ratio is 0.25, the calculation, taking into account the separation effect, was done when the slit width ratio was 0.5 and 1.0. **Figure 3** summarizes the results of these analyses\*.

### 3. The apparatus of the experiment and the method used

**Figure 4** outlines the apparatus of the experiment. In this study, latex suspension was appropriately diluted, and the aerosol for testing was generated by spraying the suspension

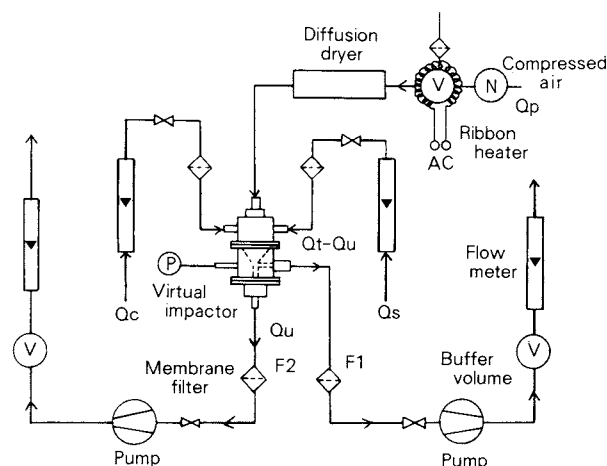


Fig. 4 Apparatus of the experiment

with a nebulizer. The generated aerosol was fed into the impactor via the ribbon heater and diffusion dryer. The flow rate at each location was measured using rotameters calibrated in advance with a gas meter. Ambient air was filtered with a glassfiber filter (GB-100R produced by TOYO ROSHI Corp.) and introduced into the impactor as clean air. Aerosol particles classified with the impactor were collected using Sartorius-Membrance filter F1 or F2 and were subjected to the process described in the previous report<sup>6)</sup>. They were then observed and counted by means of a microscope.

**Table 1** lists the conditions of the experiment. Experiments were carried out for slit width ratios  $S_l$  of 0.25, 0.5, and 1.0, and a flow rate ratio  $Q_r (= Q_u/Q_t)$  of 0.1. All experiments done by introducing clean air were conducted by fixing the slit width ratio at 0.5. The pressure at the slit exit and the ambient pressure were measured using a vacuum gauge, and Cunningham's slip correction was carried out.

\* The square root of the inertia parameter was used as the abscissa of the figure in order to make it easy to understand the correspondence between the separation efficiency and particle size. In the following description,  $\sqrt{\psi}$  is also designated as an inertia parameter to simplify the description. To avoid confusion, the symbol  $\sqrt{\psi}$  has also been included.



Table 1 Conditions of the experiment

Aerosol*	PSL ( $\rho_p = 1.05 \times 10^3 \text{ kg/m}^3$ $D_p = 0.804, 1.091 \mu\text{m}$ ) PVT ( $\rho_p = 1.03 \times 10^3 \text{ kg/m}^3$ $D_p = 2.020 \mu\text{m}$ )
Number concentration of aerosol	$31 - 1590 \times 10^6$ [particles/m <sup>3</sup> ]
Total flow rate	$Q_t = 8 - 104$ [l/min]
Mean air velocity in jet	$u_0 = 12 - 166$ [m/s]
Mean air velocity in slit	$u_{sl} = 19 - 288$ [m/s]
Interial parameter	$\sqrt{\psi} = 0.2 - 1.5$ [-]
Flow Reynolds number	$Re = 1500 - 19700$ [-]
Jet dimmension	$B = 0.102$ [cm], $l = 1.022$ [cm]
Slit width ratio	$Sl = 0.25, 0.5, 1.0$
Flow rate ratio	$Q_r = 1/10$

\* PSL = Polystyrene Latex  
PVT = Polyvinyltoluene

#### 4. Results of the experiment and discussion

Figure 5 shows the relationship obtained between the inertia parameter and separation efficiency when no clean air flowed into the jet. The figure shows that the smaller the slit width ratio  $Sl$  is, the smaller the inertia parameter  $\sqrt{\psi_{50}}$  is in order to obtain 50% separation efficiency. The separation efficiency curves of slit width ratios of 0.25, 0.5, and 1.0 are almost parallel. That is, the sharpness of the classification performance does not depend on

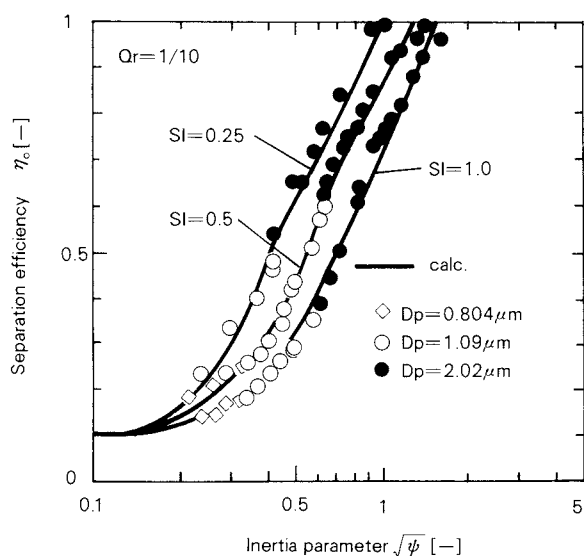


Fig. 5 Comparison between calculation and experimental separation efficiencies

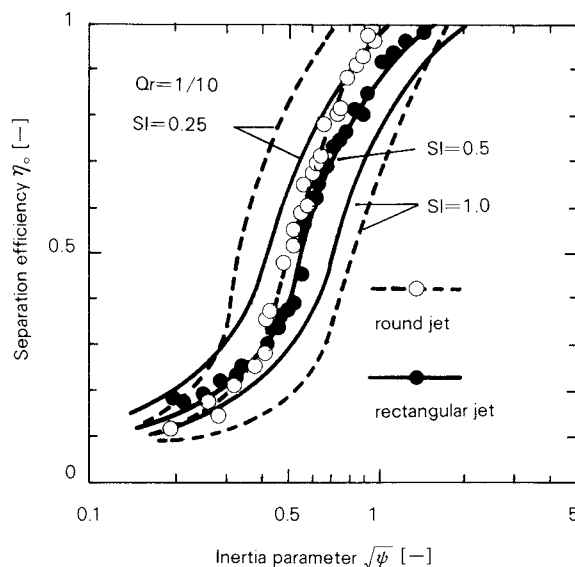


Fig. 6 Separation characteristics of the rectangular jet impactor compared with those of the round jet impactor

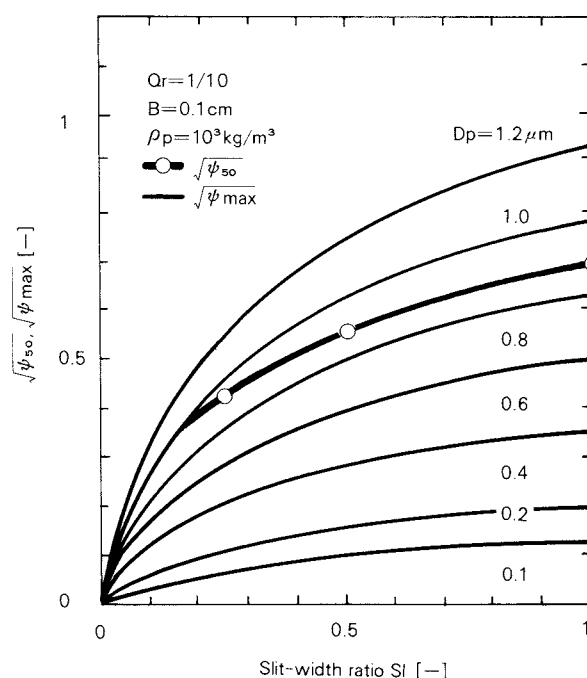


Fig. 7 Inertia parameters as a function of the ratio of slit gap to jet breadth

the slit width ratio. Solid lines in Fig. 5 represent the numerical-analysis results shown in Fig. 3, wherein the calculation results, in which the air flow is assumed as a potential flow, are modified based on the effects of the acceleration jet and the flow separation at the slit. The

figure reveals that the calculation and results of the experiment agree satisfactorily.

**Figure 6** shows the relationship between the inertia parameter  $\sqrt{\psi}$  and separation efficiency  $\eta_0$  of rectangular- and round-jet-impactors having the same slit width ratio. The solid and broken lines represent the results of the experiment using rectangular and round jet impactors. Only the data of  $S_l = 0.5$  was plotted to obtain a clear figure. The data on the round impactor were quoted from the previous report<sup>6)</sup>. The figure shows that the round jet impactor can obtain sharper classification performance and that its inertia parameter  $\sqrt{\psi_{50}}$  for obtaining 50% separation efficiency varies depending on the slit width ratio. The smallest particle that the present impactor can classify without using clean air is discussed next.

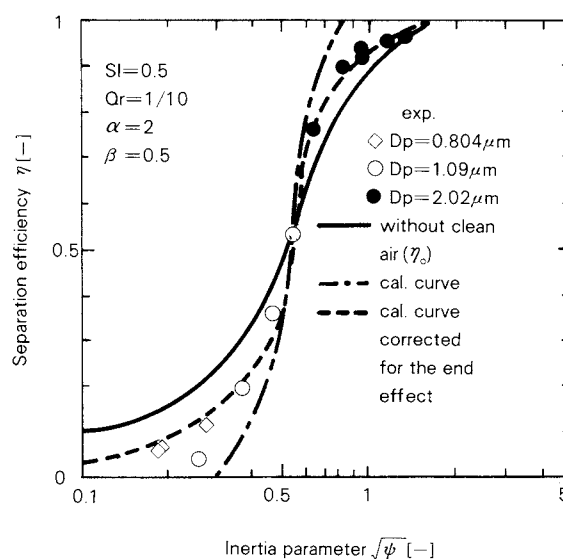
**Figure 7** illustrates the dependencies of both the calculated maximum inertia parameter  $\sqrt{\psi_{\max}}$ , limited by the sound velocity (described below), and the experimentally obtained inertia parameter  $\sqrt{\psi_{50}}$ , to obtain 50% separation efficiency, in which the slit width ratio of an impactor has a jet width of  $B = 1$  mm.

The maximum inertia parameter limited by the sound velocity represents an inertia parameter for the mean air velocity in jet  $u_0$  when either the jet velocity or slit velocity reaches acoustic velocity. In this experiment, since the slit width ratio  $S_l$  is smaller than 1, the critical condition is obtained when the slit velocity reaches the acoustic velocity. However, since flow separation occurs at the slit as described above, the effects of the flow separation should be corrected. In this study,  $S'_l \times (\text{sound velocity})/0.9$  was entered into the mean air velocity in jet  $u_0$  using the theoretical calculation result reported by Forney et. al.<sup>2)</sup>, where the correction coefficient 0.9 means that 90% of the total flow rate  $Q_t$  was drawn into the slit side ( $Q_r = 0.1$ ).  $S'_l$  is the value of the slit width ratio corrected for flow separation. ( $S'_l = 0.128, 0.248, 0.339, 0.400, 0.455$  correspond to  $S_l = 0.2, 0.4, 0.6, 0.8, 1.0$ . The ratio  $S'_l/S_l$  is 0.640, 0.620, 0.563, 0.500, 0.455.) The results reported by Forney et. al. agree with the observed results of flow separation using the enlarged transparent model.

If the curve of the maximum inertia parameter  $\sqrt{\psi_{\max}}$  limited by the sound velocity of a specific particle size is below the curve of in-

ertia parameter  $\sqrt{\psi_{50}}$  for obtaining 50% separation, it is impossible for more than 50% of the particles of a specific size to move directly into the coarser particle zone. Accordingly, it can be understood that the present impactor can classify particles of an aerodynamic diameter of 1 micron, but it cannot classify particles of aerodynamic diameter of 0.8 micron or less, irrespective of the slit width ratio. The curve of  $\sqrt{\psi_{50}}$  varies parallel to the curve of  $\sqrt{\psi_{\max}}$ , as shown in **Fig. 7**. Therefore, the minimum particle diameter able to be classified at the maximum suction rate, when the mean air velocity in the slit reaches acoustic velocity, does not depend on the slit width ratio.

**Figures 8 and 9** show the relationships between the inertia parameter  $\sqrt{\psi}$  and the separation efficiency  $\eta$  when clean air is introduced into the jet. These experiments were carried out under the following conditions: the slit width ratio  $S_l$  was 0.5, and flow rate ratio  $Q_r$  was 1/10, where  $\alpha = 2$ , and  $\beta = 0.5$  represents that the sectional mean velocity ratio of clean air introduced from (2) to aerosol flow introduced from (1) to the clean air flow from (3) at the converging zone of the jet which is 1:1:1.  $\alpha = 2$ , and  $\beta = 0$  represents 0:1:2, and  $\alpha = 2$ , and  $\beta = 1$  represents 2:1:0. The solid lines represent the separation efficiency  $\eta_0$  when clean air was not introduced, and the chain lines represent the calculated separation efficiency



**Fig. 8** The effect of clean-air flows on the separation characteristics

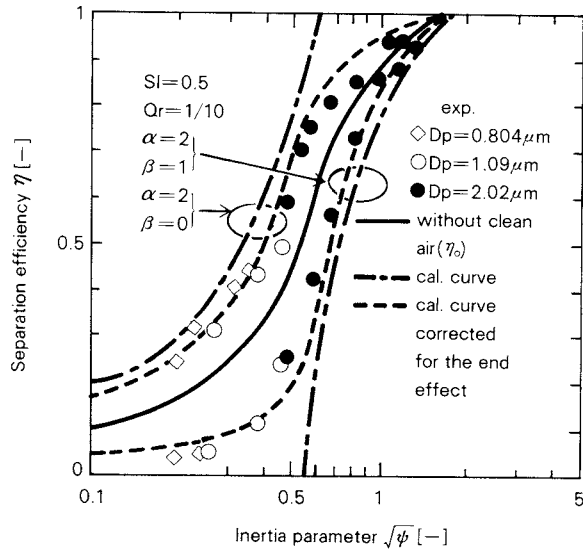


Fig. 9 The effect of clean-air flows on the separation characteristics

when clean air was introduced, obtained by substituting  $\eta_0$  represented by the solid line into Eq. (9). The broken line represents a calculation result assuming that the aerosol flow and clean air flow are not completely separated into three layers in the jet, and that they are mixed at both ends of the jet in the lengthwise direction. That is, by assuming they are completely mixed in the length  $\gamma$  times the jet width  $B$ , separation efficiency  $\eta_e$  is given by:

$$\eta_e = \frac{2\gamma}{l} \eta_0 + \frac{l - 2\gamma}{l} \eta \quad (15)$$

where  $l$  is the length of the rectangular jet.

The broken line represents the separation efficiency obtained by substituting  $\gamma = 2B$  into the above equation. When  $\alpha = 2$ ,  $\beta = 0.5$  (Fig. 8), that is, the aerosol flow and clean air flow are introduced at the same velocities, the sharpness of the classification performance is improved more than when clean air is not introduced, showing that the separation efficiency of finer particles (in the lower inertia region) decreases below the undeflected flow rate. These results are satisfactorily represented by the broken lines wherein the end effect is considered. When  $\alpha = 2$ ,  $\beta = 0$  (Fig. 9), that is, clean air flow at the opposite side of the slit is not introduced, the inertia parameter for obtaining 50% separation can be reduced without reducing the slit width ratio, however, the separation

efficiency in the lower inertia region becomes less sharp. These results are also satisfactorily represented by the broken lines wherein the end effect is considered. When  $\alpha = 2$ ,  $\beta = 1$ , that is, clean air flow at the slit side is not introduced, and the separation efficiency curve moves toward the right. These results are also satisfactorily represented by the broken lines wherein the end effect is considered.

The following empirical equation was obtained by measuring the differential pressure  $\Delta P$  between the static pressure at the exit of the present impactor and the atmospheric pressure. This was done by changing the mean air velocity in jet  $u_0$  and slit width ratio  $S_l$ , and by making a linear approximation on the double logarithm graph using the least squares method.

$$\Delta P = 2.82 S_l^{-0.84} \cdot \rho_i u_0^{2.00} \text{ [Pa]} \quad (16)$$

where  $\rho_i$  is air density at the impactor inlet.

The 68 items of data are obtained for the slit width ratios 0.25, 0.5, and 1.0, and the standard deviation of the estimated value in the above equation is  $1.8 \times 10^3$  Pa.

## 5. Conclusion

A rectangular jet virtual impactor was constructed to study aerosol classification performance both theoretically and experimentally, and the following results were obtained:

- 1) The separation efficiency curves (without introducing clean air) obtained by potential flow calculation with modifications of the effects of the acceleration jet and the flow separation at the slit, satisfactorily agree with the experimentally obtained results.
- 2) The sharpness of classification was not as good as that of a round jet impactor, and the variable range of the cut size was smaller.
- 3) The mean air velocity at the slit reaches the sound velocity earlier than at the jet in the present impactor. This differs from the round jet impactor. Therefore, the width and length of the jet should be determined with respect to this consideration. The minimum cut size at the maximum flow rate reaching the sound velocity does not depend on the slit width ratio.
- 4) Higher degrees of classification performance



sharpness were obtained by introducing clean air flows into both sides of the aerosol flow, and the cut size was variable with in a certain range by adjusting the flow rate of the introduced clean air flow.

- 5) The separation characteristics when clean air was introduced were well explained by assuming perfect mixing between the aerosol flow and the clean air flows at both ends (twice the jet width) of the rectangular jet.

## Nomenclature

$B$	: jet width	[m]
$B_a$	: left end of aerosol flow (Fig. 2)	[m]
$B_b$	: right end of aerosol flow (Fig. 2)	[m]
$B_c$	: critical position (critical trajectory, Fig. 2)	[m]
$C$	: Cunningham's correction factor	[-]
$D_p$	: particle diameter	[m]
$l$	: jet length	[m]
$n$	: number concentration of aerosol particles	[particles/m <sup>3</sup> ]
$\Delta P$	: pressure difference	[Pa]
$Q_c$	: clean air flow rate (Fig. 2)	[m <sup>3</sup> /s]
$Q_p$	: aerosol sample flow rate	[m <sup>3</sup> /s]
$Q_r$	: ratio of undeflected flow rate to total flow rate ( $=Q_u/Q_t$ )	[-]
$Q_s$	: clean air flow rate (slit side, Fig. 2)	[m <sup>3</sup> /s]
$Q_t$	: total flow rate	[m <sup>3</sup> /s]
$Q_u$	: undeflected flow rate through nozzle	[m <sup>3</sup> /s]
$Q_x$	: $\int_0^{B_c} u dx$	[m <sup>3</sup> /s]
$R_c$	: flow Reynolds number in jet ( $=Bu_0\rho_i/\mu$ )	[-]
$S_l$	: ratio of slit gap to jet width	[-]
$S_l'$	: $S_l$ corrected for flow separation	[-]
$u$	: air velocity	[m/s]
$u_c$	: mean air velocity at end point of converging zone of acceleration-jet	[m/s]

$u_0$	: mean air velocity in jet	[m/s]
$\bar{x}(=x/B)$		
$\bar{y}(=y/B)$	: dimensionless coordinates	[-]
$\alpha$	: $Q_t/Q_p$	[-]
$\beta$	: $Q_c/Q_p$	[-]
$\gamma$	: parameter in Eq. (15)	[-]
$\delta$	: deviation of particle trajectory at jet inlet	[m]
$\bar{\delta}$	: $\delta/B$	[-]
$\eta$	: separation efficiency	[-]
$\eta_0$	: separation efficiency (without clean air)	[-]
$\eta_0'$	: separation efficiency (without acceleration-jet, without clean air)	[-]
$\eta_e$	: separation efficiency corrected for end effect	[-]
$\theta$	: half angle of converging zone of acceleration-jet	[rad]
$\mu$	: air viscosity	[kg/m·s]
$\rho_i$	: air density at impactor inlet	[kg/m <sup>3</sup> ]
$\rho_p$	: particle density	[kg/m <sup>3</sup> ]
$\tau$	: particle relaxation time ( $=D_p^2\rho_p/18\mu$ )	[s]
$\bar{\varphi}$	: dimensionless stream function	[-]
$\psi$	: inertia parameter ( $=\rho_p D_p^2 u_0 C / 18\mu B$ )	[-]

## References

- 1) Conner, W. D.: *J. Air Pollut. Control Assoc.*, **16**, 35 (1966).
- 2) Forney, L. J., D. G. Ravenhall and D. S. Winn: *J. Appl. Phys.*, **49**, 2339 (1978).
- 3) Forney, L. J., D. G. Ravenhall and S. S. Lee: *Environ. Sci. Technol.*, **16**, 492 (1982).
- 4) Marple, V. A. and C. M. Chien: *Environ. Sci. Technol.*, **16**, 492 (1982).
- 5) Masuda, H., D. Hochrainer and W. Stöber: *J. Aerosol Sci.*, **10**, 275 (1979).
- 6) Masuda, H. and T. Motooka: *Kagaku Kogaku Ronbunshu*, **8**, 717 (1982).
- 7) Yoshida, H., K. Fujii, Y. Yonemoto, H. Masuda and K. Iinoya: *Ibid*, **4**, 419 (1978).

# A Technique for Measuring Broad Size Ranges of Aerosol Particles by the Laser Beam Scattering Method Combined with Condensation Nuclei<sup>†</sup>

Satoshi Okuda, Hiroshi Takano  
and Takeshi Iwamoto  
Department of Chemical Engineering  
Doshisha University\*

## Abstract

*In order to determine broad ranges of particle size distribution, a new measuring method combined both light scattering and electrostatic separation-condensation nuclei is experimentally investigated. From the experiments, it is confirmed that by using a sensitive optical particle counter connected to a digital computer system, the particle size range of 10nm to 10 $\mu$ m in diameter is adequately measurable. Furthermore, using the same criteria to count the number of particles over the entire size range, this method is found to be remarkably applicable as a practical means of more accurate measurement.*

## 1. Introduction

The measurement of particle size distributions dispersed in the atmosphere is usually performed by several different methods, such as optical diffraction, elastic or quasi-elastic light scattering, inertia impaction, electrostatic mobility analysis, diffusion battery, dark-field microscopy, and others<sup>1~3)</sup>. However, there is a basic limitation at approximately 0.1 $\mu$ m and 1.0 $\mu$ m in diameter which originates from each measuring principle and occurs in the measurable ranges of particle sizes and concentrations. Due to this, it has been suggested that a technique combining the above mentioned methods might be useful in extensively expanding the measurable size ranges from 1 nm to 10 $\mu$ m<sup>4)</sup>.

In some cases, these combinations cause practical difficulties in adopting the data reduction of the experimental results obtained from each method, because of the different size bases of the particles<sup>5)</sup>. It should also be noted that the quasi-elastic light scattering

method merely a way to broaden the size of measurement<sup>6)</sup>. It seems to be inaccurate for multi-mode particle size distributions.

As a result, a method which combines both sensitive optical particle counting and electrostatic separation-condensation nuclei is experimentally investigated for the purpose of detecting a broad range of sizes between 10nm and 10 $\mu$ m in diameter. In practice, particles larger than 0.1 $\mu$ m are ordinarily measured by the optical particle counter. On the other hand, particles less than 0.1 $\mu$ m are first separated into a certain narrow size range by the electrostatic force using a differential mobility analyzer, and then the separated particles are increased in size using condensation nuclei in order to count the number of particles. In either case, the number of particles of each size are measured by the same optical counting system, and the size distribution is then obtained in the number-size base. It should be noted again that a more sensitive optical particle counter such as that mentioned above is necessary to employ this method.

Even though this kind of combination might in principle be applicable for the measurement of aerosol particles having a broader size range, there have not been any adequate investigations to experimentally verify this idea. Therefore, theoretical considerations of this method

\* Karasuma Imadegawa, Kamigyo-ku, Kyoto, 602  
TEL. 075 (251) 3874

† This report was originally printed in *J. Soc. Powder Technology, Japan*, 23, 408-414 (1986) in Japanese, before being translated into English with the permission of the editorial committee of the Soc. Powder Technology, Japan.

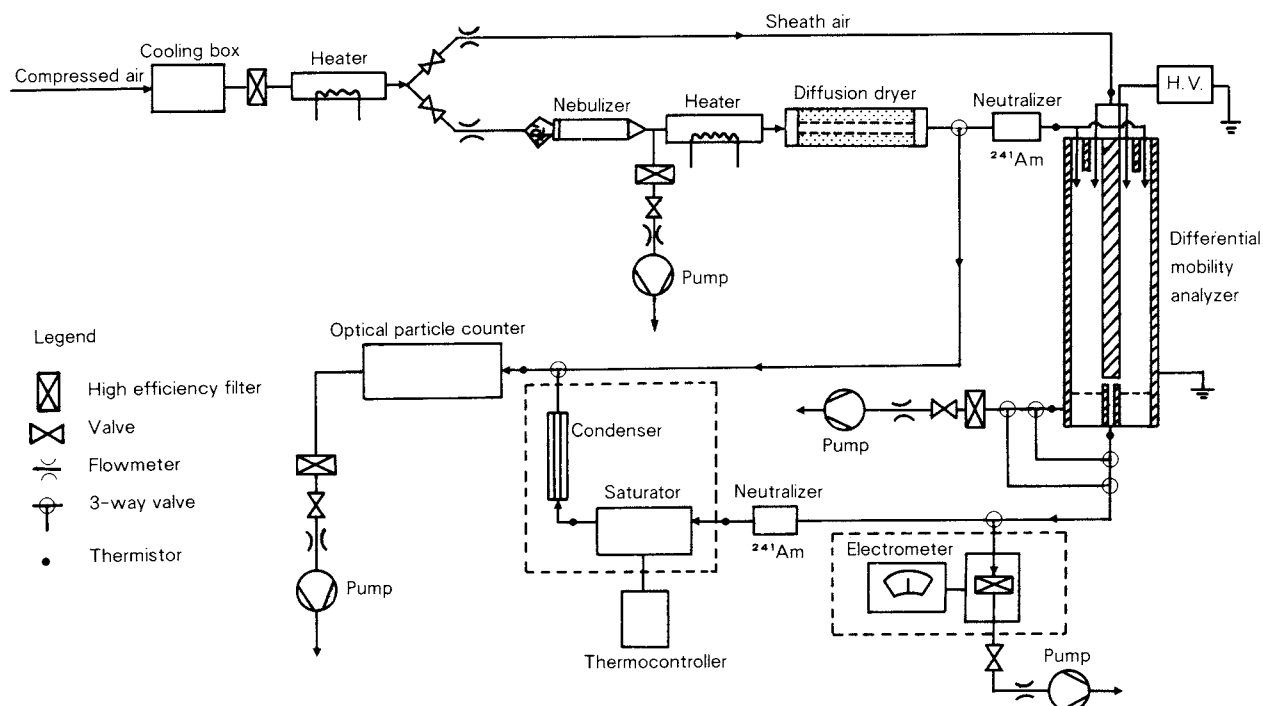


Fig. 1 Schematic diagram of the measuring system in the experiment

and some experimental results using ambient aerosols are discussed in relationship to the cross-sensitive error, counting efficiency, and the size distribution of the aerosol particles.

## 2. Theoretical Consideration

Figure 1 shows a schematic diagram of the experimental measuring system which consists of a differential mobility analyzer, condensation nuclei, and a sensitive optical particle counter. Using these instruments, the experimental procedures were divided in two ways at the particle size of  $0.1\mu\text{m}$  as follows: The particles larger than  $0.1\mu\text{m}$  were directly measured by the sensitive optical particle counter itself. Response curves were obtained for the optical particle counter as shown in Fig. 2. This numerical result indicates the well-known relationships for refractive indices of particles, wavelength of an incident light beam, and geometric optical conditions of the optical particle counter<sup>7)</sup>. In the smaller size range, electrical signals from the light scattering of aerosol particles become small in order to distinguish the noise from the signals because the scattering intensity is proportional to the 6th power of particle size in the region of Rayleigh scattering.

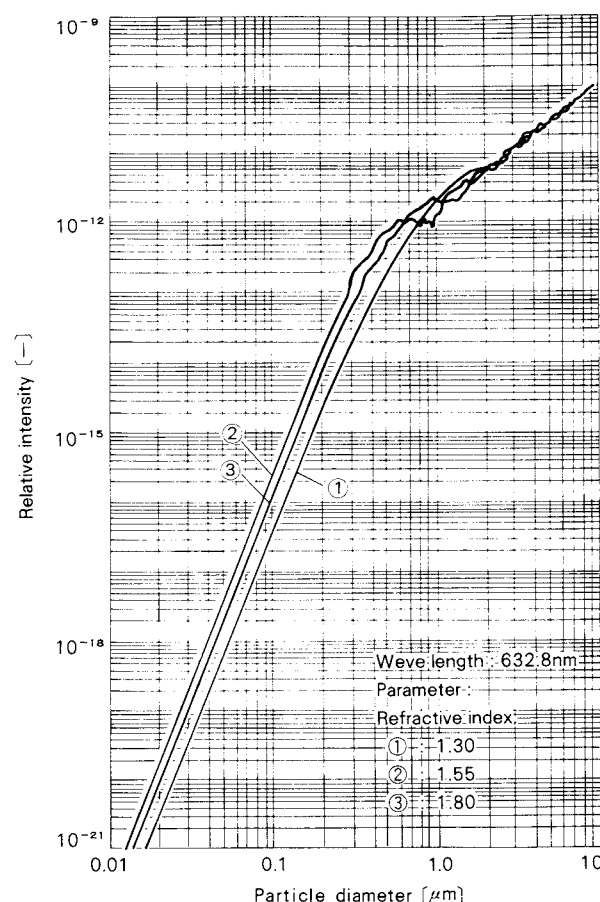


Fig. 2 Response curves between scattering intensity and particle diameter in relationship to refractive index



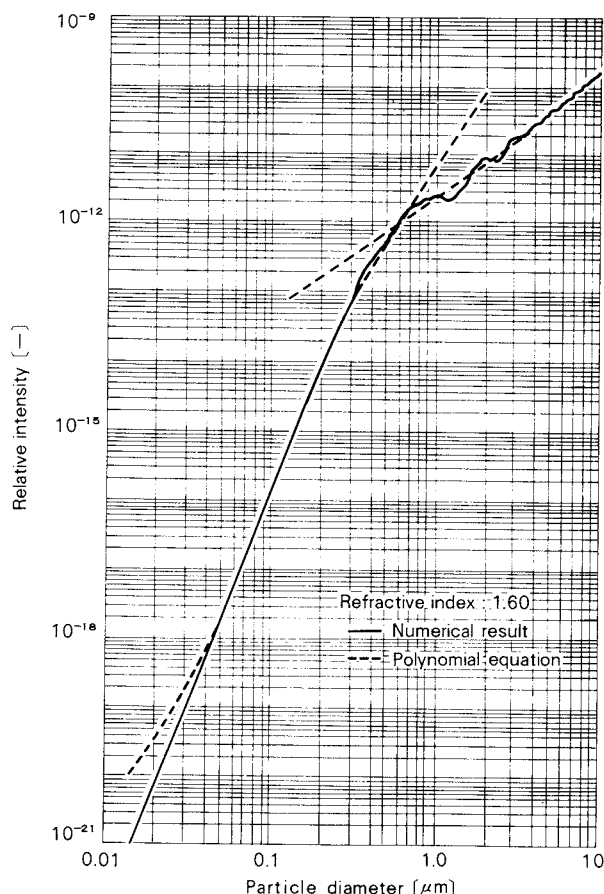


Fig. 3 An approximate method for converting the scattering intensity of the particle diameter

In the size range of  $0.1\mu\text{m}$  and  $10\mu\text{m}$ , an approximate polynomial equation, shown in Fig. 3, might be employed to determine the particle size from the data of light scattering intensity within an error of 5 percent. This equation is of course strongly dependent upon the refractive index of the aerosol particle, and so the measurable size range of the optical particle counter will usually change with materials of the particle. Moreover, in general, it has been pointed out that this method of approximation could not be applied to larger sized particles in the Mie resonance region. However, from the numerical estimation of the permissible error, it was noticed that the sensitive optical counter which was used in this experiment had a broad measurable size range of  $0.1 \sim 10\mu\text{m}$  with sufficient resolution of the particle size for refractive indices of 1.3 to 1.8<sup>8)</sup>. Therefore, in this experiment, the measurable

size range was numerically estimated to be  $0.1 \sim 10\mu\text{m}$ , as mentioned above.

For particles smaller than  $0.1\mu\text{m}$ , it is usually difficult to measure particle size distributions by the light scattering method. One useful way to measure those particles would be to combine both electrostatic separation by the differential mobility analyzer and particle counting after the condensation nuclei, which is performed by the same optical particle counter.

The differential mobility analyzer is a well-known instrument for separating particles much smaller than  $0.2\mu\text{m}$  in relationship to the electrostatic mobility of charged particles. In this procedure, the number of elementary charges on a single particle is the most important parameter for separating a certain size of particle by the applied voltage between electrodes. As shown in Fig. 4, a cross-sensitivity of the particle size based on the number of elementary charges occurs in all size ranges at a fixed applied voltage<sup>9)</sup>.

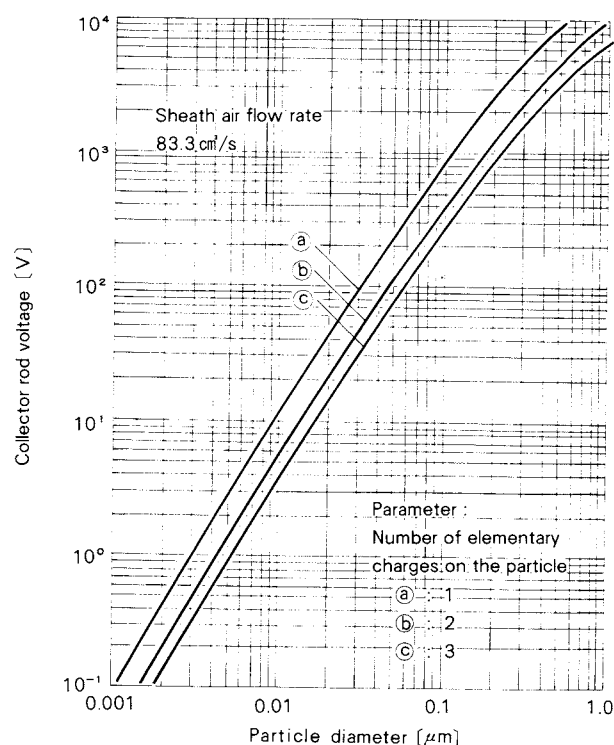


Fig. 4 Collector rod voltage of the differential mobility analyzer as a function of particle diameter

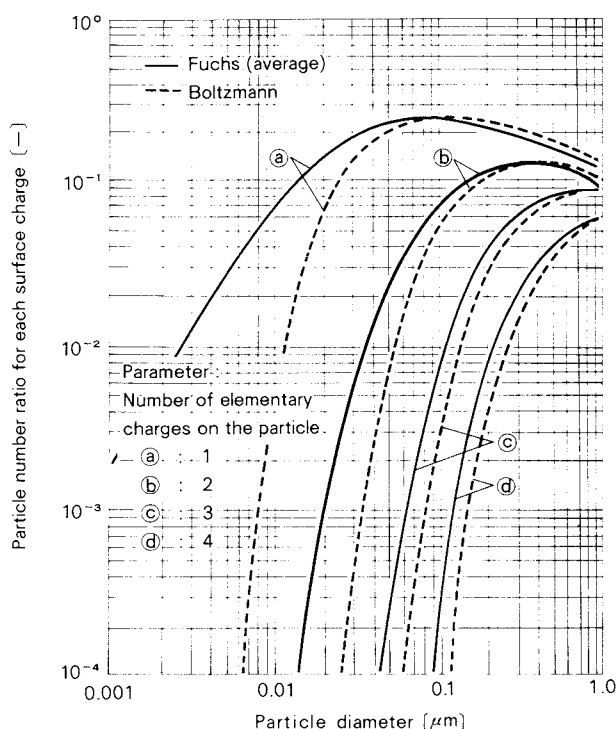


Fig. 5 Electrical charge distribution of neutralized aerosol particles

For bipolar charging, such as radioactive neutralization, the distribution of particle charges is induced on each size of particle as shown in Fig. 5. This indicates the difference between modified Fuchs' and Boltzmann equations. It has been noticed that the experimental results agreed better with the modified Fuchs' equation for the average of all particles than with the Boltzmann distribution for particles smaller than  $0.1\mu\text{m}^{10)}$ . In this size range, the ratio of the particle numbers having a positive single elementary charge to the total number of particles at the size of  $0.1\mu\text{m}$  was about 24.1 percent, and the ratios for the double and triple charges were 6.4 and 0.7 percent, respectively. Therefore, if the particle only has a single charge, the particle number should be estimated within an error of 7 percent. For particles larger than  $0.1\mu\text{m}$ , it is impossible to say this because the charge distribution becomes broad. This means that a certain value of electrostatic mobility no longer determines the particle size itself related to the applied voltage. It was also observed that the contribution of larger particles having many elementary charges was negligibly small.

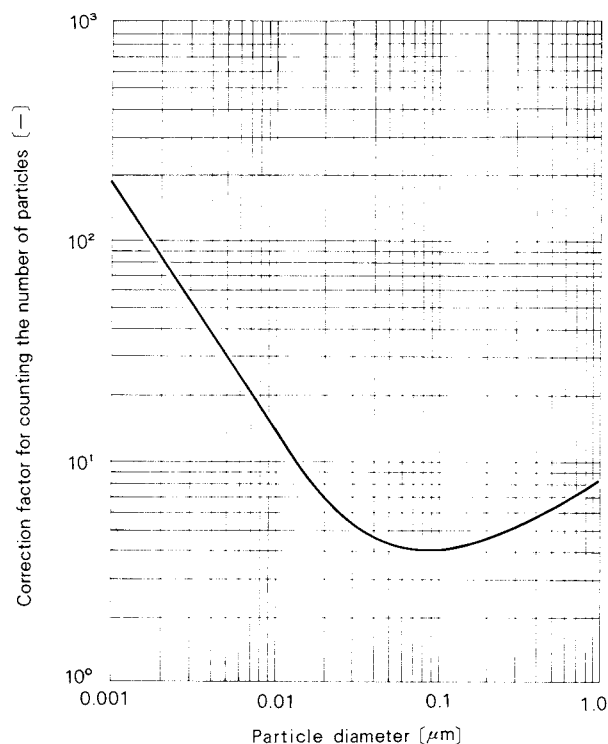


Fig. 6 Correction factor of the particle number for a single particle for use in the estimation of the total number of particles of a given particle size

Another factor in the small size region is the method for the conversion of the real number of particles for a given size in which a correction factor, shown in Fig. 6, is used where the neutralized particles have a charge distribution expressed as a modified Fuchs' equation. For sizes smaller than 10nm, this correction factor for determining the number of particles became extremely large, and the uncertainty in determining particle numbers may have increased. Moreover, the condensation efficiency of these particle sizes became smaller than unity in the nuclei chamber<sup>11)</sup>. Therefore, judging from both the technique for counting the loss of particles by the light scattering method and the condensation efficiency of particles smaller than 10nm, it may be reasonable to apply this correction factor to conversions for counting the number of particles under the limitation that particle sizes are between 10nm and  $0.1\mu\text{m}$  in diameter.

According to these considerations, it was theoretically concluded that this proposed method could be applied to the measurement of sizes ranging from 10nm to  $10\mu\text{m}$  within an error of 8 percent, and that the number-size

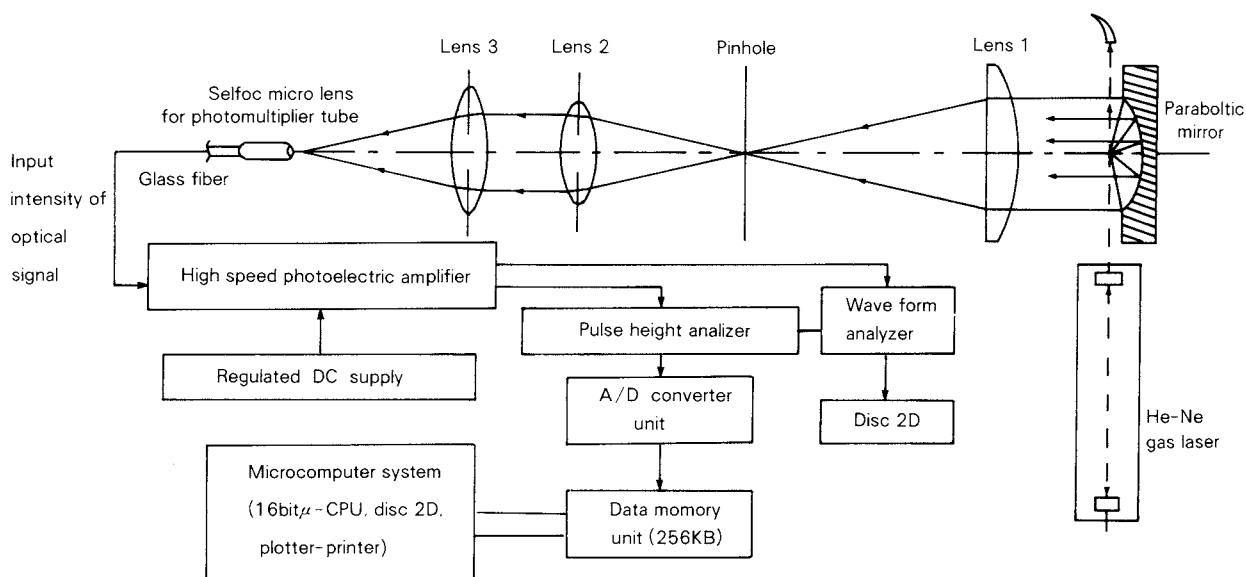


Fig. 7 Schematic diagram of the optical unit and signal analysis

distributions of particles could be obtained for whole particle sizes. This procedure, which has never been used in practice, would be useful for environmental field work and laboratory studies.

### 3. The System of Measurement and Procedures of the Experiment

A schematic diagram of the optical unit and signal analysis is shown in Fig. 7. The main measuring devices of this system consist of a particle counter and a wave form analyzer.

Figure 8 shows an on-line measuring system for a laser beam scattering particle counter that was constructed with an He-Ne gas laser of 20mW having a wavelength of 632.8nm (Toshiba, LAG-20), a parabolic mirror for focussing the scattered light, a high speed photoelectric amplifier (Eiko Electric, PEA-HCA using a side-on type photo-multiplier supplied by Hamamatsu Photonics, R928), and data memory with the large size of 256KB (Nippon Kanomax, Model-5211) in order to analyze the pulse height of scattering signals.

The light scattered by the aerosol particle from the laser beam was gathered by a parabolic mirror and then transferred to the photoelectric amplifier through a glass fiber (Nippon

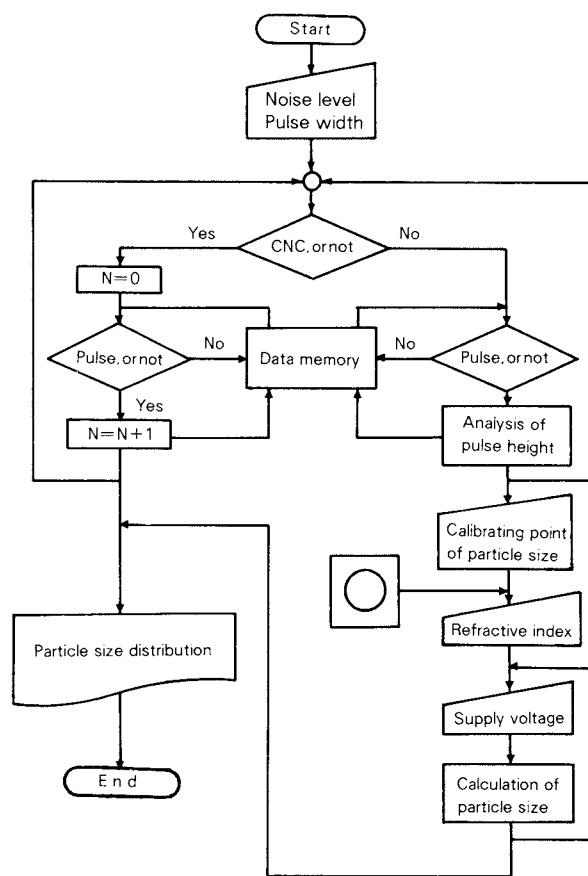


Fig. 8 Flow chart of software for data reduction



Itagarasu, core size of  $200\mu\text{m}$  and multimode with selfoc micro lens). After that, the scattering signal was stored in the data memory through an A/D converter (Nippon Kanomax, Model-1414, input range of  $\pm 2.5\text{V}$  and 10 bit/word) in order to analyze the pulse height for measuring the diameters and concentrations of the aerosol particles by the digital computer system (Nippon Kanomax, Realex-16). A software technique for this data analysis consisted of noise cancelling and counting of the particle number, which were performed in the size range between  $0.1\mu\text{m}$  and  $10\mu\text{m}$  in diameter. A wave form analyzer (Analogic, Data-6000, with a sampling rate of 36 MHz) was used to check the shape of the scattering signals.

The same data analysis was applied to measure the size distribution of particles smaller than  $0.1\mu\text{m}$ . After condensation nuclei, the smaller particle became large, and the numbers for each given particle size which were separated by the differential mobility analyzer were detected by means of the optical particle counter. The scanning of this particle size was performed over several particle sizes by changing with the applied voltage between the electrodes. In this experiment, it was noticed that the S/N ratio of the scattering to the noise signals was extremely high. In order to measure the broaden distribution of particle size, the voltage applied to a photomultiplier was changed with the size ranges. In spite of those complex procedures by using the combined method, data reduction performed by a software technique was sufficient to obtain the particle size distributions even for the broad distributions. Finally, figures of the size distribution were drawn by a X-Y plotter as one of the output modes.

In the experiments, some sample aerosol particles, such as monodispersed polystyrene latex (Dow Chemical;  $0.085\mu\text{m}$ ,  $0.109\mu\text{m}$  and  $0.913\mu\text{m}$ , with a refractive index of 1.595), acrylic acid resin powder (with a mean diameter of  $0.37\mu\text{m}$  and a geometric standard deviation of 1.17 measured by electron microscopy, and a refractive index of 1.38), and nylon powder (with a mean diameter of  $2.6\mu\text{m}$  and a geometric standard deviation of 2.17, and a refractive index of 1.41) were used for the calibration of some absolute levels of scattering intensities, in order to check the size distributions in the

size region less than  $1\mu\text{m}$ , and in the range larger than that, respectively. Moreover, the ambient aerosol particle was also employed for a sample having a broad size distribution.

Some other experimental conditions were as follows: The dilute liquid for polystyrene laticies was filtered water. In all procedures, the sampling and sheath air flowrates were constant,  $16.7\text{ cm}^3/\text{s}$  and  $83.3\text{ cm}^3/\text{s}$ , respectively. After neutralizations of the electrical charging of the particles using the radioactive source of  $^{241}\text{Am}$ , the electrostatic separation of smaller particles was done with the differential mobility analyzer. The applied voltage was set up as a digital value and scanned in a range of 1 mV to 3,000V using appropriate intervals. In the condensation chamber, the *n*-butyl alcohol was vaporized as a condensed liquid at a constant temperature of 413K, which was controlled by the PID method.

#### 4. Results of the Experiment and Discussion

Measured data for the size distribution of

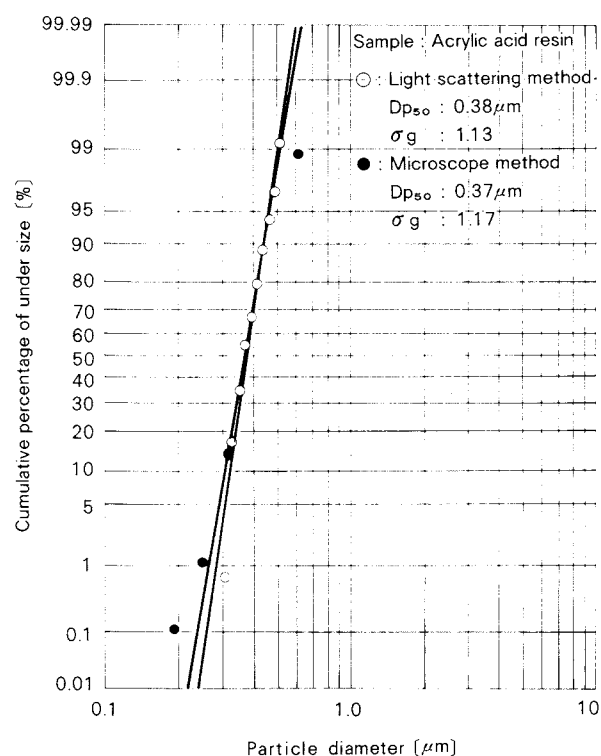


Fig. 9 Particle size distribution of acrylic acid resin powder in comparison to the data measured by the electron microscope method

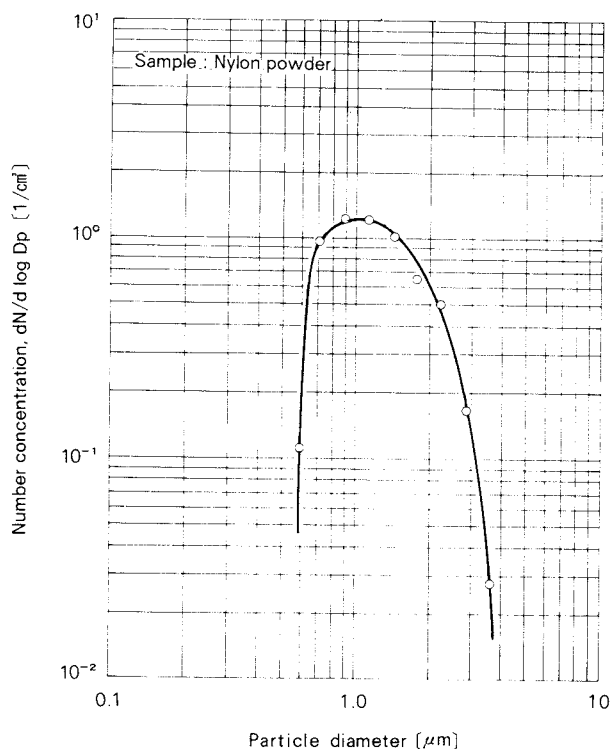


Fig. 10 Particle size distribution of nylon powder in number concentration as a sample aerosol sized near 1.0  $\mu\text{m}$  in diameter

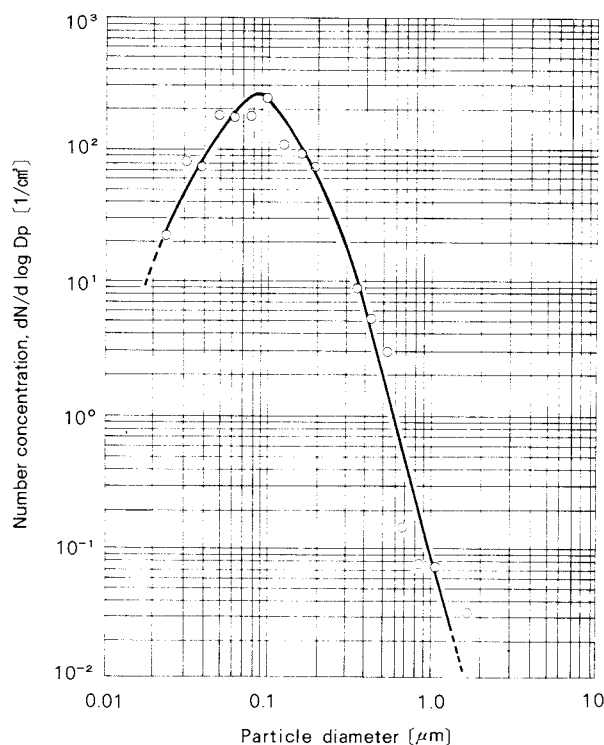


Fig. 11 The result of measuring the particle number distribution of the ambient aerosol particles having a broad range of sizes

acrylic acid resin powder indicated that the mean diameter and the geometric standard deviation were 0.38  $\mu\text{m}$  and 1.13, respectively, as shown in Fig. 9. This was similar to the result of the experiment when using obtained by the electron microscope method. It has also been confirmed that the accuracy of this optical particle counter was sufficient to measure particles larger than 0.1  $\mu\text{m}$ , judging from some previous data on the calibration using polystyrene latices and response curves of the particle size<sup>8)</sup>.

The particle size distribution of nylon powder is shown in Fig. 10, and indicates that the results of the experiment were qualitatively similar to the data obtained by the centrifugal sedimentation method (Shimadzu, SA-CP2). These number-mean diameters were slightly different from each other. It was also noticed that the particle number concentration did not agree with the data from the cascade impactor. For samples having a broad particle size distribution, these facts could be fundamentally explained by different bases of measuring

principles and by an error which occurred due to the conversion of the volume-mean diameter to a number-mean one. However, the S/N ratio of the scattering signal was extremely high for all experimental conditions despite differences between the volumetric and counting methods. Therefore, it was decided that this optical particle counting method could be used to measure particle sizes up to 10  $\mu\text{m}$ , taking into account the complicated effects of both the accuracy of the response curve in size and of light diffraction on the scattering intensity for larger size of particles.

Ambient aerosol was used, because it has a broad range of sizes. This shows the effectiveness of this combined method in the experiments. The result of the size distribution of the sample particles, shown in Fig. 11, was similar to the data from previous investigations<sup>2)</sup>. It was also recognized that the S/N ratio of the scattering signal was high enough, as was the case of nylon powder, and that the connection of the experimental data for the size 0.1  $\mu\text{m}$  was smooth and precise in counting the particle

numbers. Therefore, it was concluded that this combined method was effective in the measurement of a broad size distribution of aerosol particles between 10nm and 10 $\mu$ m in diameter.

In addition, it might be possible to extend this combined method to sizes smaller than 10nm when considering the condensation efficiency of such tiny particles, which has been experimentally obtained<sup>11)</sup>. However, if this method is expanded to those smaller sizes, it should be recognized that inaccuracies in the data on particle number concentration will increase with the particle counting loss, because the correction factor becomes excessively large.

## 5. Conclusion

In order to determine broad ranges of particle size distribution, a new method of measurement which combined both the light scattering and electrostatic separation-condensation nuclei was experimentally investigated by means of a sensitive optical counter connected to a digital signal processor. The number concentration of particles for each size was measured by dividing the counting of the particles in two ways at the size of 0.1 $\mu$ m. The size distribution of particles was finally obtained by integrating these number concentrations of particles using the on-line measuring system.

In conclusion, the experimental results for some sample aerosols indicated that the particle sizes between 10nm and 10 $\mu$ m were reasonably determined in relationship to the S/N ratio of the scattering signal and correction factor of the counting efficiency. Therefore, in comparison to other measuring systems, it should be noted that this combined method is sufficiently accurate and useful in measur-

ing the particle size distribution in the same number-size base.

## Acknowledgement

The authors would like to express their appreciation to Y. Nakajima for his help in the experiments. The numerical calculation of the scattering intensity to determine the particle size was performed by large-scale computer systems, both the HITAC M280H at Doshisha University and the FACOM VP-200 at Kyoto University.

## References

- 1) Liu, B. Y. H. (Ed.): "Fine Particles-Aerosol Generation, Measurement, Sampling and Analysis", Academic Press (1976).
- 2) Lundgren, D. A., et al. (Ed.): "Aerosol Measurement", University Press of Florida (1979).
- 3) Kousaka, Y.: The 2nd Symposium on Aerosol Science and Technology, Japan, p. 1 (1984).
- 4) Whitby, K. T., et al.: *J. Colloid and Interface Science*, **39**, 136 (1972).
- 5) Tohno, S. and K. Takahashi: *J. Soc. Powder Technology, Japan*, **17**, [10], 565 (1980).
- 6) Ito, Y. and K. Takahashi: The 1st Symposium on Aerosol Science and Technology, Japan, p. 55 (1983).
- 7) Kerker, M.: "The Scattering of Light and Other Electromagnetic Radiation", Chap. 4, Academic Press (1969).
- 8) Okuda, S., H. Takano, H. Kawamura and T. Iwamoto: The 3rd Symposium on Aerosol Science and Technology, Japan, p. 192 (1985).
- 9) Okuda, S., F. Lee and H. Takano: Proceedings of the 2nd International Conference on Electrostatic Precipitators, p. 653 (1985).
- 10) Kousaka, Y., K. Okuyama and M. Adachi: *Aerosol Science and Technology*, **4**, 209 (1985).
- 11) Bartz, H., et al.: *J. Aerosol Science*, **16**, 443 (1985).

# The Submicron Grinding of BaTiO<sub>3</sub> by Ball Milling<sup>†</sup>

Kenji Tanaka, Kiichi Minai,  
Kikuo Wakino and Isao Uei  
Murata Mfg. Co., Ltd.\*

## Abstract

*The submicron grinding of BaTiO<sub>3</sub> powder was studied by a ball mill with small alumina balls of 0.75 mmφ to 30 mmφ. BaTiO<sub>3</sub> clinker, which was obtained by calcining an equimolar mixture of TiO<sub>2</sub> and BaCO<sub>3</sub>, was preground to 1.8 micron. Submicron grinding of the BaTiO<sub>3</sub> powder was possible by ball milling with several mmφ balls. For a ball diameter of 2 mm, the specific surface area was maximized.*

*An attempt was made to represent the specific surface area in terms of volume per ball and total surface area of used balls, and the following experimental equation with a time term was obtained,*

$$\ln(SS) = -0.247 \ln r^3 - 0.738/r + 0.429 \ln t + 1.57$$

*where SS is the specific surface area, r is the ball radius, and t is time. The multiple correlation coefficient R was found to be 0.982 when calculated by a computer.*

## 1. Introduction

Conventionally, a rotary ball mill has been used to grind electronic materials. Mixing solid-phase synthesized BaTiO<sub>3</sub> (main material of dielectric ceramic) with subsidiary materials requires a grinding process of several hours to several tens of hours (the process becomes too costly if the processing time exceeds these periods) to obtain a particle diameter of 1.6 to 2.3 microns.

According to the report by Nakazumi<sup>1)</sup>, when BaTiO<sub>3</sub> powder, coarsely atomized in advance, is ground with a wet ball mill, the particles saturate at a diameter of 1.3 microns or thereabout and cannot be ground finer than the above diameter even when continuing the grinding operation. This diameter represents an apparent grinding limit and is called the equilibrium state of grinding<sup>2)</sup>. The advantages of ball mill grinding are that the grinding method

causes less contamination from the grinding balls, and it is easy to increase the processing volume and facilitate mass-production. The disadvantage of requiring a longer processing period is compensated for by mass-production.

It is only recently that smaller-sized and more finely configured electronic parts have been produced, thus requiring more finely ground raw materials for electronic ceramic materials. As a result, expensive barium titanate powder, produced by vapor- or liquid-deposit method, has been introduced to the market.

Conventionally, various types of fine grinding machines have been developed, introduced, and used based on their applications. In mass-production factories of ceramic materials for electronic use, grinding machines for pretreatment prior to ball mill processing have been developed and used.

Recently, Medium-Stirring mills<sup>3)</sup> have been introduced and widely used in the ceramics industry. In this type of grinding machines, grinding balls of 2 mmφ, made of hard glass or ceramic material, are put into a cylinder. A core rod provided with blades rotates at a high speed in order to stir a continuously fed slurry that contains particles of several microns, and thus the particles are ground. The grinding

\* 4-4-1, Higashi-Okino, Yokaichi-shi, Shiga, 527  
TEL. 07482 (2) 5500

† This report was originally printed in *J. Soc. Materials Science, Japan*, 35, 54-58 (1986) in Japanese, before being translated into English with the permission of the editorial committee of the Soc. Materials Science, Japan.



mechanism mainly reduces the size of particles. Increasing the number of times the slurry passes through the mills further reduces the size of particles.

A ball milling, in which hard balls or super-alloyed steel balls of several tens mm $\phi$  are stirred<sup>4)</sup>, attempts to obtain finer particles in a short period of time by means of impact and shear forces, in addition to the grinding mechanism. In this type of ball mills, considerable heat generation occurs during operation. When grinding balls made of ceramic are used, an appropriate stirring speed should be selected based on the strength of ceramic balls.

These types are variations of the ball mill, and their feature is to use small grinding balls of 2 mm to 5 mm $\phi$ . They permit submicron grinding if contamination due to grinding balls is allowed.

Although authors have used ball mills in our laboratory or factory for an extended period of time, and there are many reports by predecessors<sup>5~7)</sup>, consideration has not been given to the size of grinding balls.

Most reports recorded "the grinding time of a ball mill", but few of them reported the size of the grinding balls. We have not found one report where grinding balls of 5 mm $\phi$  or smaller are consciously used to grind raw materials such as ceramics for electronic use.

These phenomena are thought to be caused because, conventionally, particle sizes of micron order have been satisfactorily accepted when grinding a large quantity of ceramic material with a ball mill. Moreover, it has been assumed that using grinding balls of a small size results in excessive contamination due to the abrasion of grinding balls.

We studied the grinding characteristics of a rotary ball mill using grinding balls of various sizes, ranging from 30 mm $\phi$  to 0.75 mm $\phi$ , under the same grinding conditions. The diameter of the obtained particles was studied utilizing the Coulter Counter method, specific surface area, and electron microscope photographs. As a result, it was proved that submicron grinding is possible by using small-sized grinding balls. In addition, apprehension regarding increased contamination due to abrasion was proved to be unnecessary; In fact, the contamination was actually reduced, as shown in a preceding report<sup>8)</sup>.

## 2. Experiments

### 2. 1 Raw materials

The raw materials were prepared as follows: The same moles of TiO<sub>2</sub> and BaCO<sub>3</sub> were mixed and synthesized at 1150°C to obtain BaTiO<sub>3</sub>. The obtained BaTiO<sub>3</sub> clinker was preliminarily ground using a Super Micron Mill. The specific surface area of the preliminarily ground particles was 1.19 m<sup>2</sup>/g, and the mean diameter was 1.85 microns. The particle size distribution is shown at the uppermost portion of Fig. 2.

### 2. 2 Grinding

The sample was wet-ground using a resin pot having a capacity of 31 and using a small-sized ball mill for experimental application. The grinding conditions used were as follows: Preliminarily ground BaTiO<sub>3</sub> of 375g and pure water of 1.5 l were poured into the pot that was rotated at a speed of 115 rpm. In all experiments, grinding balls made of alumina were poured into the pot in amounts of 1.5l; the value was 1/2 of the total contents. The selected diameters of the grinding balls were 0.75, 1, 2, 5, 10, 20, and 30 mm $\phi$ , and the grinding time periods were 3, 6, 12, 24, 48, 96, and 192 hours. The diameter of particles ground under each experimental condition (diameter of grinding ball and grinding time period) was measured using the slurry immediately after being ground and using the samples obtained by drying the slurry at 110°C.

### 3. Particle size measurement

The particle sizes were investigated using the Coulter Counter method, specific surface area, and electron microscope photographs. The Coulter Counter method, conventionally used for measuring sizes of fine particles, is a very convenient method because it can simultaneously obtain the diameter of particles and their distribution. However, when the diameter of the particles to be measured is 0.5 microns or less, the method cannot detect the size. Moreover, this method may determine, as one particle, a cohered particle group consisting of several to several tens of particles, unless the particles are satisfactorily dispersed. As a result, the particle size obtained by this method

does not coincide with the result obtained when using the specific surface area as a measurement. An electron microscope can satisfactorily observe submicron particles. However, the observed field is limited to a relatively small area. Therefore, the values obtained when using the specific surface area as a measurement are more relevant, thus the values were simultaneously reported.

#### 4. Results and discussion

By varying the diameter of grinding balls from 30 mm $\phi$  to 0.75 mm $\phi$  and the grinding time period from 3 hours to 192 hours for each grinding ball diameter, BaTiO<sub>3</sub> particles were ground, and the sizes of particles ground under each of the grinding conditions were measured by the Coulter Counter method. **Figure 1** shows the mean particle size ( $D_{50}$ ) obtained from each grinding condition. By reducing the diameter of the grinding balls from 30 mm $\phi$ ,  $D_{50}$  is reduced and has a minimum value at the ball diameter of 2 mm $\phi$ . By reducing the ball diameter from this value,  $D_{50}$  shows an inclination to slightly increase. To obtain submicron particles, it took approximately 192 hours with grinding balls of 15 mm $\phi$  diameter, approximately 70 hours with 10 mm $\phi$  balls, approximately 18 hours with 5 mm $\phi$  balls, and 5 hours with 2 mm $\phi$  balls (the minimum time period). When smaller balls of 1 mm $\phi$  and 0.75 mm $\phi$  were used, longer time periods (approximately 8 and 18 hours, respectively) were required in order to obtain submicron particles. **Figure 2** shows the dependency of the variation of particle size distribution upon the diameter of grinding balls using the data after 24 hours of grinding. As shown in this figure, the entire size area of the particles ground using balls of 20 and 10 mm $\phi$  was measured; however, some sizes of particles ground with balls ranging from 5.0 mm $\phi$  through 0.75 mm $\phi$  could not be determined by the applied method of measurement. As a result, only a part of the distribution curve of these particle sizes is shown in the figure. However, each  $D_{50}$  of distribution curves of particles ground with 5 mm $\phi$  through 0.75 mm $\phi$  balls shows that those particles are ground up to submicron sizes. **Figure 2** also shows that the grinding balls of 2 mm $\phi$  have the highest grinding speed.

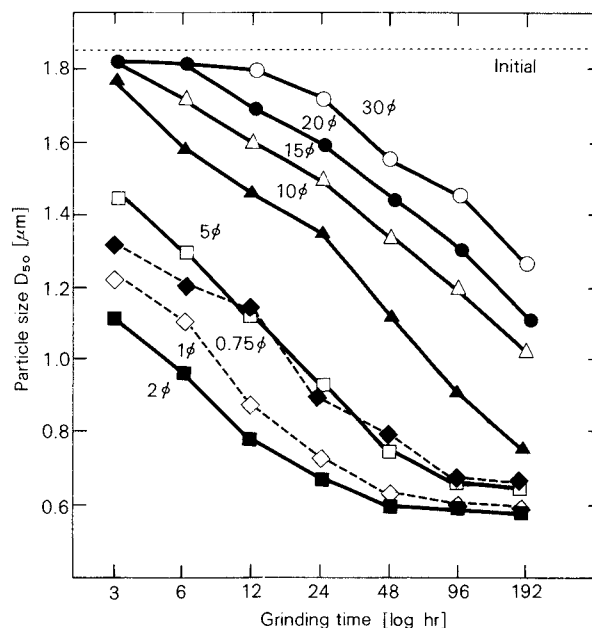


Fig. 1 Variation in particle size after grinding

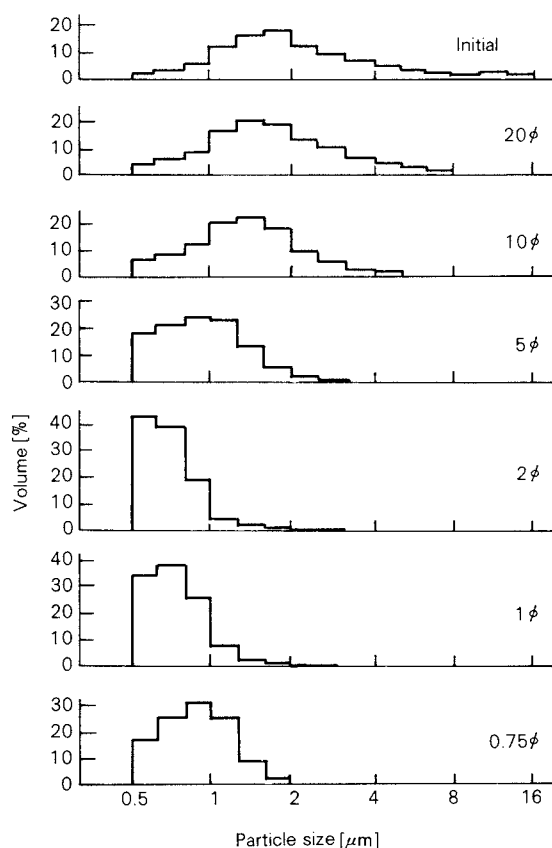


Fig. 2 Variation in particle size distribution after grinding for 24 hr

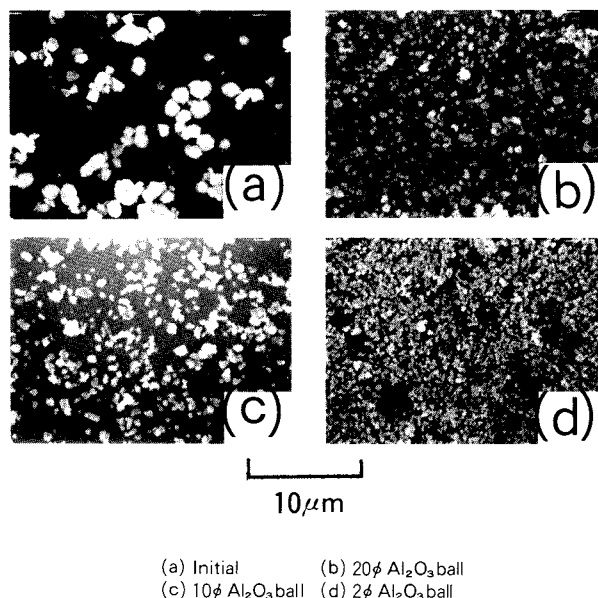


Fig. 3 Scanning electron micrographs of a particle after grinding for 192 hr

Figure 3 shows the scanning electron micrographs of the initial material and particles ground with balls of 20 mm $\phi$ , 10 mm $\phi$ , and 2 mm $\phi$  for 192 hours. As clearly shown in these micrographs, reducing the ball diameter has the effect of obtaining submicron particles.

Figure 4 shows the effect of grinding time on the particle size distribution. As shown in this figure, the accumulated particle size distribution curves sequentially move toward the side containing finer particles. This suggests that only the particles having specific diameters

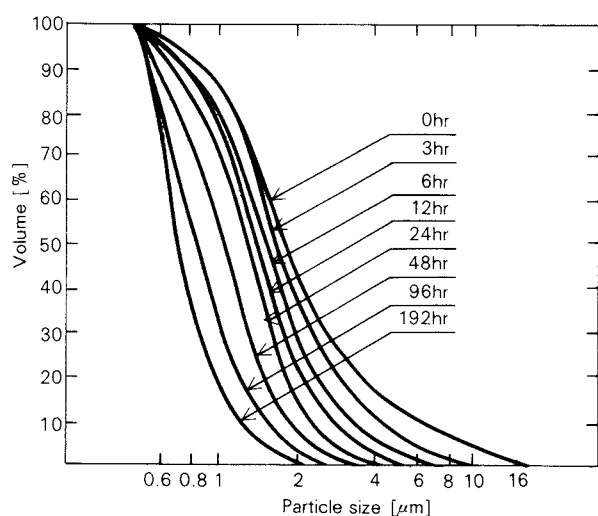


Fig. 4 Effect of grinding time on particle size distribution

are not selectively ground, and that the particles within the entire diameter distribution area are ground at the same time. This observation coincides with the model of surface grinding proposed by Hüttig, et al.<sup>9)</sup>, wherein solid particles crack at their surfaces, the cracks do not propagate into the inside of the particles, and the particles' finer parts are peeled off of the surface; thus each particle is gradually, entirely, finely ground.

Mori, Jimbo, et al.<sup>10)</sup> reported that grinding speed is proportional to the weight per ball. However, this theory cannot explain the fact that the maximum grinding speed is obtained by using the 2 mm $\phi$  balls.

In a study on ball mill grinding, H. E. Rose<sup>11)</sup> reported that particles pinched between the balls are ground, however, some particles pinched by the balls may be rejected without being ground. Therefore, the probability of ball collisions is inversely proportional to the square of the particle diameter and irrespective of the ball diameter. This theory also cannot satisfactorily explain the maximum grinding speed with balls of a 2 mm $\phi$ .

Since the measuring device used for the Coulter Counter method was revealed to have limitations, the specific surface area of particles ground under various conditions was measured using the BET method. The results are shown in Fig. 5. As shown in this figure, the specific surface area of particles ground with balls of each diameter increases with the increase in grinding time. The maximum grinding speed is

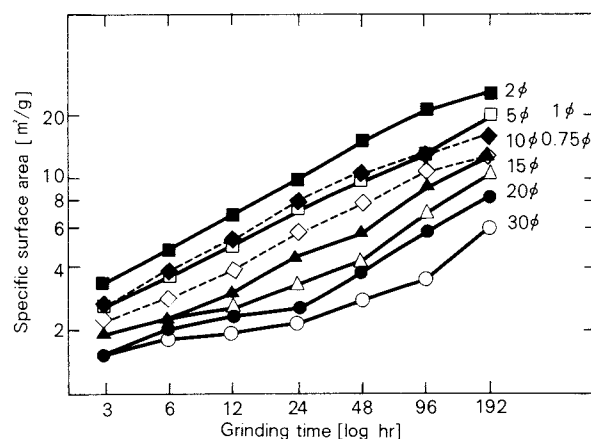


Fig. 5 Relationship between specific surface area and grinding time

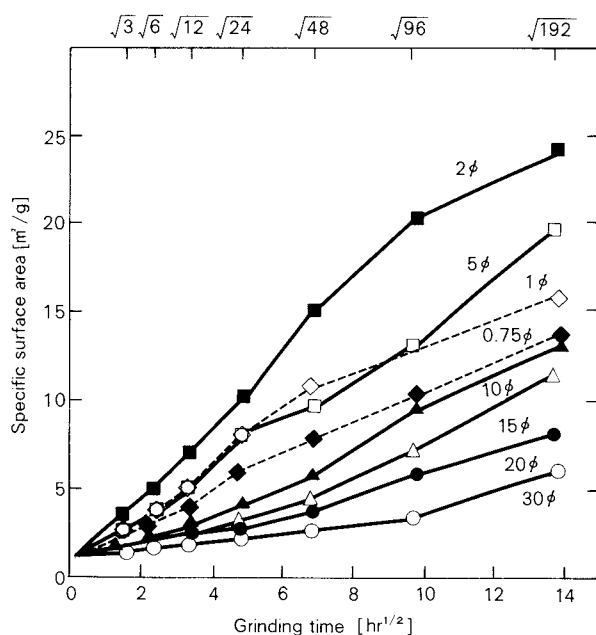


Fig. 6 Relationship between specific surface area and grinding time

obtained with balls of 2 mm $\phi$ , showing the same inclination as the  $D_{50}$  values obtained by the Coulter Counter method.

Rose<sup>12)</sup> reported that the increased value in the specific surface area of particles during the grinding operation with a ball mill is proportional to the  $\alpha$ -th power of the grinding time, where  $\alpha = 2$  is for soft materials, and  $\alpha = 0.22$  for hard materials. Kiesskalt<sup>13)</sup> reported a value of  $\alpha = 1/2$  for the later stage of grinding brittle materials.

Since the BaTiO<sub>3</sub> used as the initial material was brittle and mechanically ground in advance, the specific surface area data obtained were plotted for  $t^{1/2}$  (as reported by Kiesskalt) as shown in Fig. 6. By assuming that the grinding speed (slopes of the curves shown in Fig. 6) is a function  $f(r)$  of the diameter ( $r$ ) of the grinding balls, and by plotting the slopes on a double logarithm graph, an upwardly convex curve shown in Fig. 7 was obtained showing the maximum value at  $r = 1$ .

Where  $SS = at^{1/2} + b$ , and the slope  $f(r) = SS/t$ , the following is obtained:

$$\ln f(r) = \ln(SS) - 1/2 \cdot \ln t \quad (1)$$

The convex curve shown in Fig. 7 is supposed to be a composite form of components that in-

crease or decrease the grinding speed with the increase of the ball diameter. The former increasing components are the circumference length ( $2\pi r$ ), which is proportional to the ball diameter  $r$ , surface area ( $4\pi r^2$ ), which is proportional to  $r^2$ , and ball volume ( $4/3 \cdot \pi r^3$ ) and ball weight ( $4/3 \cdot \pi r^3 \cdot \rho$ ), both of which are proportional to  $r^3$ . The latter decreasing components are the ball surface area per unit packing volume ( $1.81/r$  in hexagonal coarse packing), which is proportional to  $1/r$  and the number of balls per unit packing volume ( $0.141/r^3$  in hexagonal coarse packing), which is proportional to  $1/r^3$ .

Judging from the shape of the graph shown in Fig. 7,  $f(r)$  is represented by combining the increasing components  $r^\alpha$  ( $\alpha = 1, 2, 3$ ) and decreasing components  $1/r^\beta$  ( $\beta = 1, 3$ ).

$$\begin{aligned} \ln f(r) &= A \ln X_1 + B \ln X_2 \\ &= A \ln r^\alpha + B \ln e^{-1/r^\beta} \quad (2) \end{aligned}$$

$$\begin{aligned} &= A \alpha \ln r - B \cdot 1/r^\beta \\ &= m \ln r - n \cdot 1/r^\beta \quad (3) \end{aligned}$$

In the first term of the right side of Eq. (2), the exponent  $\alpha$  of  $r$  may be 1, 2, or 3, selectively. Modifying this term results in Eq. (3). Thus, this equation is irrespective of the  $\alpha$  value when entering and calculating the experimental data. However,  $\beta$  should be 1 or 3 in the second term of Eq. (3), therefore,  $\ln f(r) = m \ln r - n/r$  (4) or  $\ln f(r) = m \ln r - n/r^3$  (5)

To calculate the difference between the theoretical and experimental values using Eq. (4) or

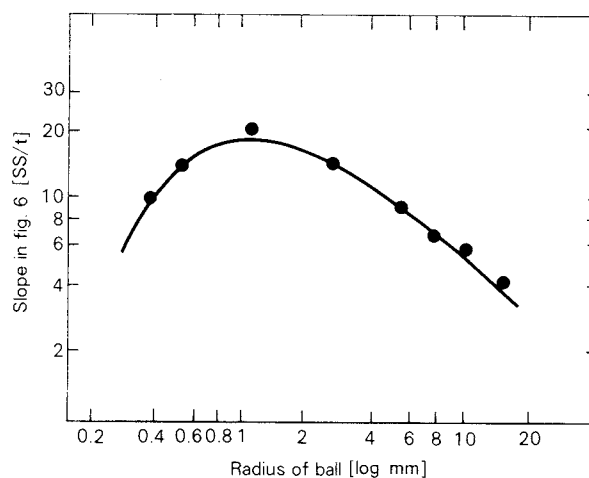


Fig. 7 Relationship between the slope ( $SS/t$ ) in Fig. 6 and the radius of a ball



Table 1 Coefficient of equation (6) and (7)

	$m$	$n$	$p$	$q$	$R$
Eq. (6)	-0.740	0.738	0.429	1.570	0.982
Eq. (7)	-0.478	0.060	0.429	0.918	0.878

(5), the time term should be contained. Therefore, Eqs. (1), (4), and (5) are combined to obtain Eqs. (6) and (7).

$$\ln(SS) = m \ln r - n/r + p \ln t + q \quad (6)$$

$$\ln(SS) = m \ln r - n/r^3 + p \ln t + q \quad (7)$$

To obtain coefficients  $m$ ,  $n$ ,  $p$ , and  $q$  in Eqs. (6) and (7) using  $r$  and  $t$  (experimental conditions), and the  $SS$  value of the specific surface area obtained by the BET method, the data obtained was subjected to multiple regression analysis with a computer. Differences between each experimental equation and the data obtained by the actual measurement were determined by obtaining and judging the multiple correlation coefficient  $R$ . Table 1 lists the obtained coefficients of Eqs. (6) and (7). The experimental expression of  $R = 0.982$  of Eq. (6), satisfactorily agrees with the experimental data. By comparing the  $R$  values of Eqs. (6) and (7), it was determined that the contribution of  $1/r$  to  $\ln(SS)$  is larger than that of  $1/r^3$ . Therefore, the specific surface area of ground particles was more dependent upon the total surface area of the grinding balls than on the number of the grinding balls.

The exponent  $\alpha$  of  $r$  of the first term on the right side of Eq. (2) is considered to relate to the behavior of the grinding balls in the ball mill. Assuming  $\alpha = 2$ , the first term on the right side in Eq. (2) represents the surface area of one ball, and the second term represents the total surface area of balls poured into the pot. As a result, both terms represent the same contents. Assuming  $\alpha = 1$ , the first term represents the circumferential length of the ball. Since the particles are ground by being pinched between the balls, it is assumed that the parts (grinding zone) of grinding balls, where the balls collide with each other and grind the particles, have a specific area. Therefore, it is incorrect to express the area with the circumference of  $\alpha = 1$ . Assuming  $\alpha = 3$ , the first term, or the increasing component of grinding speed, becomes  $\ln r^3$ , representing the volume or weight of the

grinding balls. With regard to the effect of the ball diameter on the particle to be ground, the change in ball diameter, that is, the impact force when the balls collide with each other, is primary when the diameter of grinding balls is smaller than 2 mm $\phi$ . However, when the diameter of balls is larger than 2 mm $\phi$ , the particles to be ground receive an impact force larger than a specific value, thus the effect of the ball diameter diminishes. Therefore, by selecting  $\alpha = 3$ , the experimental expression and grinding mechanism can be satisfactorily explained.

As described above, when BaTiO<sub>3</sub> particles were ground with a ball mill, a maximum specific surface area of particles appeared when balls of a 2 mm $\phi$  were used. The maximum value is represented by combining one component, the ball volume that increases with the increase in ball diameter, with another component, the total of surface area of balls that decreases with the increase in ball diameter. Including the time term, an experimental expression was obtained as follows:

$$\ln(SS) = -0.247 \ln r^3 - 0.738/r + 0.429 \ln t + 1.57 \quad (7)$$

(Units:  $SS$ ; m<sup>2</sup>/g,  $r$ ; mm,  $t$ ; hr)

Where the multiple correlation coefficient  $R = 0.982$ .

Figure 8 shows the relationship between the experimental equation (7) and the measured data when balls of a 20 mm $\phi$ , 5 mm $\phi$ , or 2 mm $\phi$  were used. They satisfactorily agree with each other.

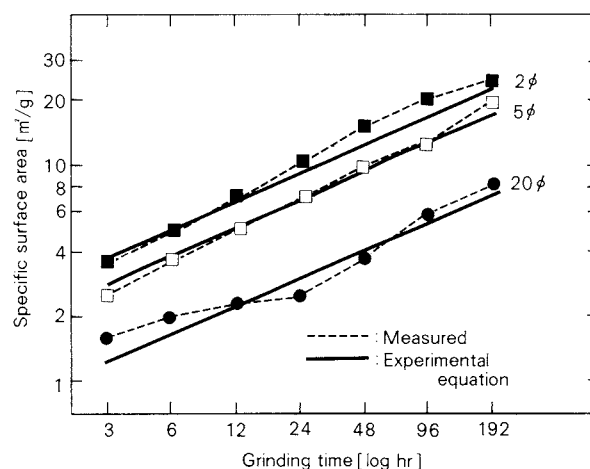


Fig. 8 Relationship between experimental equation (7) and the measured data

## 5. Conclusion

An attempt was made to grind preliminarily ground BaTiO<sub>3</sub> particles to the submicron level using a ball mill with grinding balls of a small diameter. The following results were obtained:

(1) It was demonstrated that submicron grinding is possible in a short duration by using balls of several mmφ in diameter.

(2) The accumulated distribution curves of particle sizes moved toward the finer particles size side with the elapse of grinding time suggesting that grinding proceeds during the entire range of the particle size at the same time as the surface grinding mechanism.

(3) The minimum value of the ground particle size and the maximum value of the specific surface area appeared when 2 mmφ grinding balls were used.

(4) The appearance of the maximum value of the specific surface area was represented by combining an increasing term with the increase in ball diameter, which is the term of volume of one ball, and a decreasing term with the increase of ball diameter, which is the total surface area of the balls.

(5) By multiple regression analysis, the following experimental equation was obtained,

$$\ln(SS) = -0.247 \ln r^3 - 0.738/r + 0.429 \ln t + 1.57$$

(Unit: SS; m<sup>2</sup>/g, *r*; mm, *t*; hr)

where the multiple correlation coefficient *R* = 0.982. The experimental equation and measured data satisfactorily agree with each other.

## References

- 1) Nakazumi, J., K. Miyanaga, and M. Shindo: "Annual Report on Application Study of BaTiO<sub>3</sub>", Vol. 11-II, 109 (1963).
- 2) Kubo, K.: "Introduction to Mechano-chemistry", Tokyo-Kagaku-Dozin (Tokyo) p. 87 (1987).
- 3) Koishi, M., and Y. Tsuritani: "Introduction to Dispersion Technology", Nikkan-Kogyo-Shinbun (Tokyo) p. 145 (1977).
- 4) "Data Book on Dispersion Technology", p. 449 (1978) Keiei-Kaihatsu-Center (Tokyo).
- 5) Perry, J.H.: "Chemical Engineer's Handbook", p. 1130 (1963) McGraw-Hill.
- 6) Coghill and Devabey: *US Bur Mines, Tech. Pub.*, p. 581 (1973).
- 7) Clyde Orr, Jr.: "Particulate Technology", p. 69 (1966).
- 8) "Kagaku-Kougaku Binran" *The Soc. of Chem. Engrs., Japan*, p. 1030 (1968).
- 9) Hüttig, G.F.: *Z. für Elektrochemie*, 57, 534 (1953).
- 10) Mori, Y., and G. Jimbo: "*J. Chem. Eng., Japan*", 23, 138 (1959).
- 11) Rose, H.E.: *Trans. Inst. Chem. Engrs.*, 35, 98 (1957).
- 12) Rose, H.E.: *Trans. Inst. Chem. Engrs.*, 35, 87 (1957).
- 13) Kiesskalt, S.: *Ibid.*, 97, 11 (1955).

# The Spontaneous Ignition of Dust Deposits<sup>†</sup> — Ignition Temperature and Induction Time —

**Hua Liang and Tatsuo Tanaka**

*Department of Chemical Process Engineering  
Hokkaido University\**

## Abstract

*The temperature distribution in the combustible dust deposits placed in hot environments is described by a differential equation according to the thermal theory. The temperature profiles of the dust deposits at any time could be calculated at various ambient temperatures by solving the equation using the finite element method. Thus, the minimum ambient temperature for ignition, which is defined as the ignition temperature, and the induction time to ignition could be determined. With the cylindrical cork dust deposits, the resulting temperature distribution in the radial direction at any time, and the self-ignition temperature as well as the induction time to ignition, by varying the size of the deposit, agree well with the experimental data reported by Leuschke, except at extremely high ambient temperatures. Therefore, it is practicable to estimate the spontaneous ignition behavior of dust deposits by computer simulation.*

## 1. Introduction

If the ambient temperature is sufficiently high and the storage time is sufficiently long, combustible dust deposits may spontaneously ignite. Since such spontaneous ignition may result in an explosion causing extreme damage, it is important to reveal the mechanism of spontaneous ignition and to find safety measures to prevent it.

Many studies on the spontaneous ignition of dust deposits have been done, however, most of them are purely theoretical and too difficult for engineers to thoroughly understand, thus they cannot readily be applied. For the above described reasons, Leuschke<sup>5,6)</sup> has recently reported the results of well-organized and purely experimental studies. The dust used, however, was limited to a specific material, the properties of which were unknown.

Therefore, the results cannot be adequately applied to actual problems.

Using the finite element method, this study analyzes the partial differential equation for heat balance in a cylindrical coordinate system of cork dust deposits; the cork dust being only one specimen in Leuschke's experiments, the properties of which (thermal diffusivity, frequency factor of oxidation rate, activation energy, etc.) are well-known. The study also investigates the possibility of the computer simulation of the spontaneous ignition of dust deposits by comparing the results obtained with variation per time in the temperature distribution of dust deposits, first experimentally established by Leuschke.

## 2. Bases of the calculation

According to the ignition thermal theory<sup>1)</sup>, combustible dust deposits have two heat fluxes; one is heat generation caused by the reaction of dust itself, and the other is the heat loss dissipated to the surrounding area. If it can be assumed that the reaction substance loss can be neglected and the reaction rate is in accordance with the zero order equation by Arrhenius

\* Nishi 8-chome, Kita 13-jo, Kita-ku, Sapporo, 060  
TEL. 011 (716) 2111

† This report was originally printed in *J. Soc. Powder Technology, Japan*, **23**, 326-331 (1986) in Japanese, before being translated into English with the permission of the editorial committee of the Soc. Powder Technology, Japan.

(during the period of induction time prior to ignition), a rate  $q$  of heat evolution per unit volume at an absolute temperature  $T$  is given by,

$$q = Qfe^{-E/RT} \quad (1)$$

where  $Q$  : heat of reaction [ $\text{J} \cdot \text{kg}^{-1}$ ]  
 $f$  : frequency factor of chemical reaction rate [ $\text{kg} \cdot \text{m}^{-3} \cdot \text{h}^{-1}$ ]  
 $E$  : activation energy [ $\text{J} \cdot \text{mol}^{-1}$ ]  
 $R$  : gas law constant [ $\text{J} \cdot \text{mol}^{-1} \cdot \text{K}^{-1}$ ]  
 $q$  : [ $\text{J} \cdot \text{h}^{-1} \cdot \text{m}^{-3}$ ]

To compare our results to the experimental results of the dust deposits reported by Leuschke, a simulation concerning cylindrical dust deposits was done. Assuming that heat does not flow along the axial direction of the cylindrical dust deposits having a radius  $R_1$  and considering the heat balance of the system, the following differential equation is obtained:

$$\rho C \frac{\partial T}{\partial \theta} = \frac{k}{r} \frac{\partial}{\partial r} \left( r \frac{\partial T}{\partial r} \right) + Qfe^{-E/RT} \quad (2)$$

where  $r$  : radial distance in cylindrical coordinates [m]  
 $\rho$  : density of the sample [ $\text{kg} \cdot \text{m}^{-3}$ ]  
 $C$  : specific heat of the sample [ $\text{J} \cdot \text{kg}^{-1} \cdot \text{K}^{-1}$ ]  
 $\theta$  : storage time [h]  
 $k$  : thermal conductivity of the sample [ $\text{J} \cdot \text{m}^{-1} \cdot \text{h}^{-1} \cdot \text{K}^{-1}$ ]

Since this equation has no analytical solution, the finite element method is used to solve the equation with a large-scale computer.

To compare our results to the experimental results reported by Leuschke<sup>5)</sup>, Eq. (2) is solved when a cylindrical cork dust deposit is placed under an ambient temperature  $T_a$ . In this case, the following initial and boundary conditions are used:

- I.C.  $T(r, 0) = T_r = 293\text{K}$ , at  $\theta = 0$ ,  
 $0 \leq r \leq R_1$   
 B.C.  $-k \partial T / \partial r = h (T - T_a)$ , at  $r = R_1$ ,  
 $\theta > 0$

where  $R_1$  : radius of cylinder [m]  
 $T_r$  : room temperature [K]  
 $h$  : combined heat transfer coefficient of natural convection and radiation from sidewall [ $\text{J} \cdot \text{m}^{-2} \cdot \text{h}^{-1} \cdot \text{K}^{-1}$ ]

The following properties are used:

density  $\rho = 400 [\text{kg} \cdot \text{m}^{-3}]$   
 thermal conductivity of cork<sup>3)</sup>  
 $k = 0.645T + 158.9 [\text{J} \cdot \text{m}^{-1} \cdot \text{h}^{-1} \cdot \text{K}^{-1}] \quad (3)$   
 combined heat transfer coefficient of natural convection and radiation from sidewall<sup>1,2)</sup>  
 $h = 1.49 \times 10^4 (\Delta T / \sqrt{\pi} R_1)^{0.25} + 2.04 \times 10^4$   
 $\{ (T_a/100)^4 - (T_r/100)^4 \} / (T_a - T_r)$   
 $[\text{J} \cdot \text{m}^{-2} \cdot \text{h}^{-1} \cdot \text{K}^{-1}] \quad (4)$   
 specific heat of the sample<sup>3)</sup>  
 $C = 1.88 \times 10^3 [\text{J} \cdot \text{kg}^{-1} \cdot \text{K}^{-1}]$   
 $Qf^{1)} = 4.6 \times 10^{18} [\text{J} \cdot \text{m}^{-3} \cdot \text{h}^{-1}]$   
 activation energy  
 $E = 9.71 \times 10^4 [\text{J} \cdot \text{mol}^{-1}]$

where  $T_r$  : temperature at the external surface of the cylinder  $\Delta T = T_a - T_r$

The temperature distribution per time in the cork dust deposits was obtained by solving Eq. (2) using the above conditions, properties, and the finite element method.

### 3. Comparison between the calculation and experimental results and discussion

#### 3. 1 When the volume of dust deposit is constant

By placing cylindrical cork dust deposits, the diameter and height of which are 0.16 m, in an environment of a specific temperature, Leuschke measured the temperature  $T_m$  in the middle of the sample, the temperature  $T_b$  near the border of the sample, and the temperature  $T_h$  halfway between the middle and border of the sample. He defined the spontaneous ignition temperature as the average of the minimum value of the ambient temperature when the cork dust deposits spontaneously ignite, and the maximum value of the ambient temperature when the deposits do not spontaneously ignite. For instance, the spontaneous ignition temperature of the cork dust deposits having this volume was determined to be around 412 K. The following calculation was carried out based on the experimental conditions. Figures 1, 2 and 3 show the results of calculation when  $T_a$  (ambient temperature) = 408 K, and  $T_r$  (room temperature) = 293 K. Figure 1 shows variations of  $T_m$ ,  $T_b$ , and  $T_h$  during the time lapse. Figures 2 and 3 show the temperature profiles of cork dust deposits after 51 h and 175 h. These figures reveal that the temperature profiles of the cork dust de-



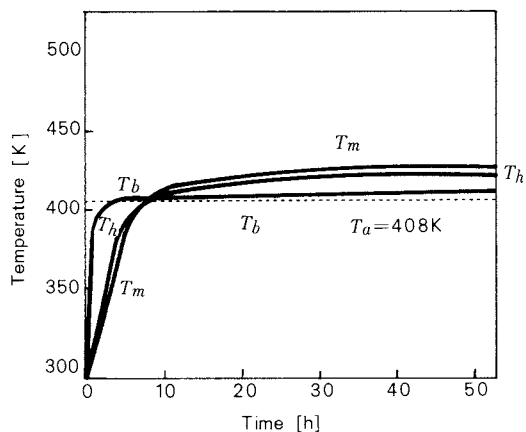


Fig. 1 Heat propagation in cork dust deposit in the lapse of time at  $T_a = 408$  K

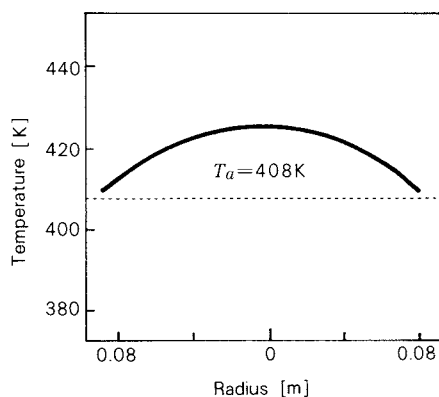


Fig. 2 Temperature profile of cork dust deposit after 51 h at  $T_a = 408$  K

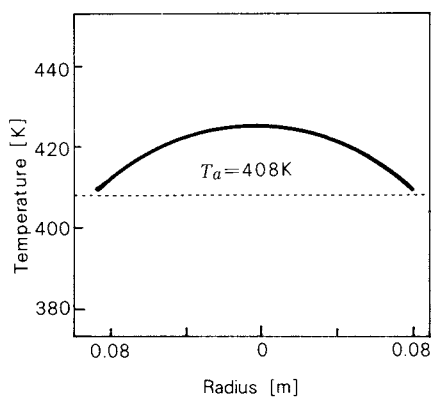


Fig. 3 Temperature profile of cork dust deposit after 175 h at  $T_a = 408$  K

posit saturate at a specific level after a certain time lapse, resulting in no spontaneous ignition.

Next, the same equation was calculated for  $T_a = 414$  K or  $444$  K using the same conditions as the experimental conditions used by Leuschke, and the results are shown in Figs. 4 (a) and 5 (a) (for  $T_a = 414$  K), and in Figs. 6 (a) and 7 (a) (for  $T_a = 444$  K). Figures 4 (a) and 6 (a) reveal that the temperature abruptly rises after a certain time lapse. This temperature rise is defined as the spontaneous ignition start. Figures 4 (a) and 5 (a) (showing the data of  $T_a = 414$  K) reveal that the ignition start begins inside the dust deposit as conventionally considered. As shown in Fig. 7 (a), the temperature profile for  $T_a = 444$  K totally differs from that of  $T_a = 414$  K. Therefore, the simulation results are compared to the experimental results reported by Leuschke in the following description.

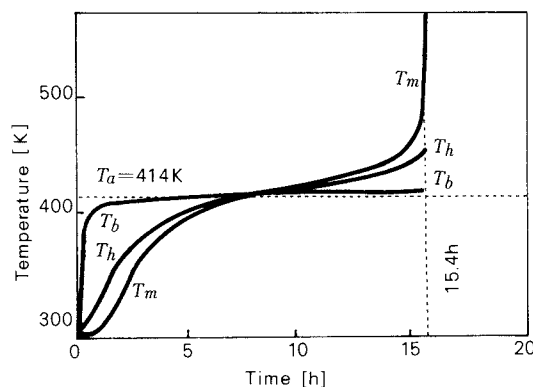


Fig. 4(a) Heat propagation in cork dust deposit in the lapse of time at  $T_a = 414$  K

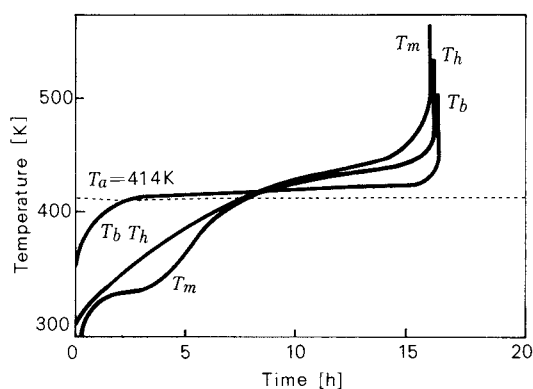


Fig. 4(b) The corresponding experimental data to Fig. 4(a) reported by Leuschke at  $T_a = 414$  K

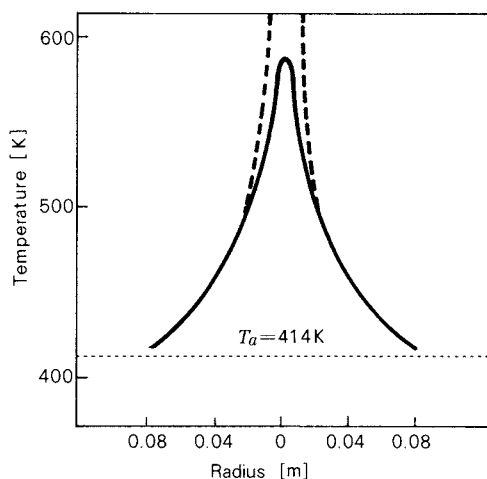


Fig. 5(a) Temperature profile of cork dust deposit showing the moment immediate before the ignition at  $T_a = 414\text{K}$ . Solid line refers to the values after 15.48 h; dashed line refers to the values after 15.49 h

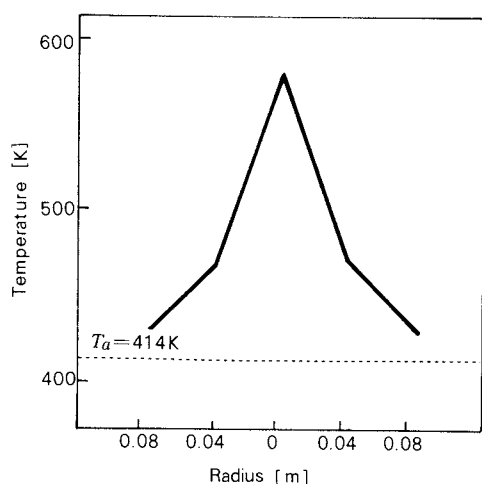


Fig. 5(b) The corresponding experimental data to Fig. 5(a) reported by Leuschke at  $T_a = 414\text{K}$

### 1) Temperature changes with time and the position of the ignition start

Figures 4 (a) and 6 (a) show the heat propagation in the cork dust deposit during the time lapse at  $T_a = 414\text{K}$  and  $444\text{K}$ . As shown in Fig. 4 (a), when  $T_a = 414\text{K}$ , the temperature near the border of the sample  $T_b$  is initially the highest ( $T_b > T_h > T_m$ ). With the lapse of time, the position of the highest temperature gradually becomes the center of the cylindrical dust deposit. Approximately 15 hours later, the temperature  $T_m$  in the middle of the sample

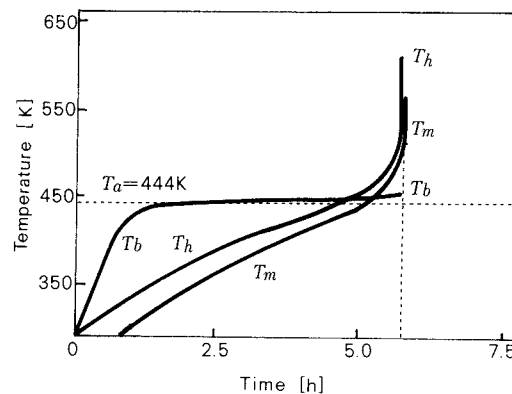


Fig. 6(a) Heat propagation in cork dust deposit in the lapse of time at  $T_a = 444\text{K}$

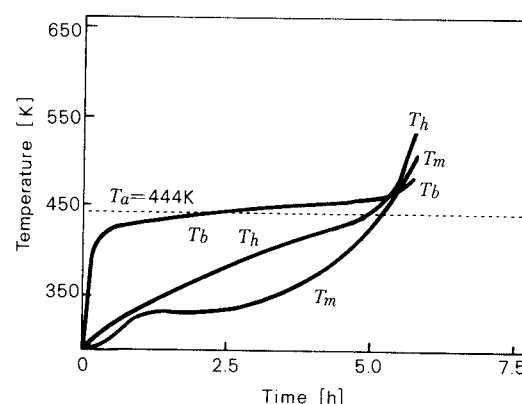


Fig. 6(b) The corresponding experimental data to Fig. 6(a) reported by Leuschke at  $T_a = 444\text{K}$

abruptly rises ( $T_m > T_h > T_b$ ), resulting in spontaneous ignition beginning from the center (Fig. 5 (a)). By comparing the results shown in Figs. 4 (a) and 5 (a) to the experimental results reported by Leuschke shown in Figs. 4 (b) and 5 (b), it is revealed that our calculation results satisfactorily agree with the experimental results and their inclination as reported by Leuschke.

On the other hand, when  $T_a = 444\text{K}$ , the temperature near the border of the sample is significantly high at the earlier stage ( $T_b > T_h > T_m$ ), as shown in Fig. 6 (a).  $T_m$  and  $T_h$  also gradually rise because of heat conduction, and  $T_h$  equals  $T_b$  at a certain point (after approximately 4.5 hrs). Following this, however, since the temperature  $T_h$  halfway between the middle and the border of the sample is sufficiently high, the reaction in this position is accelerated beyond the activation energy barrier more ra-

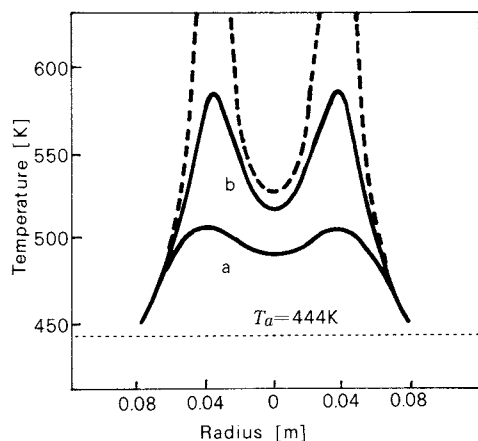


Fig. 7(a) Temperature profile of cork dust deposit showing the moment immediate before the ignition at  $T_a = 444$  K. Solid line a refers to the values after 5.45 h and b refers to the values after 5.5 h; dashed line refers to the values after 5.51 h

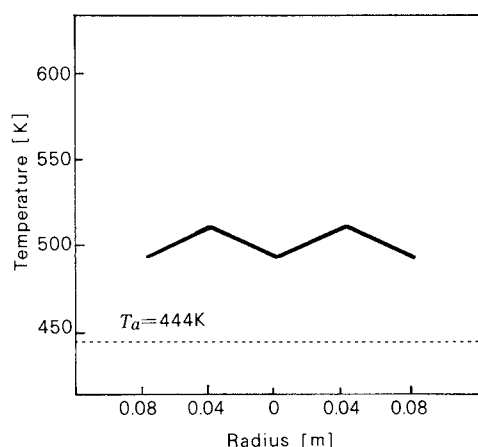


Fig. 7(b) The corresponding experimental data to Fig. 7(a) reported by Leuschke at  $T_a = 444$  K

pidly than in the other positions. Moreover, since the thermal conductivity is small,  $T_h$  abruptly increases ( $T_h > T_m > T_b$ ). As a result, spontaneous ignition occurs at the point half-way between the border and center of the sample (Fig. 7 (a)). By comparing Figs. 6 (a) and 7 (a) to Figs. 6 (b) and 7 (b), respectively, it is found that the calculation results compare satisfactorily with the experimental results reported by Leuschke. These results are the first reported in this field. In addition, it is very interesting that these results can be explained by the calculation of an equation as simple as Eq. (2).

When the ambient temperature is high

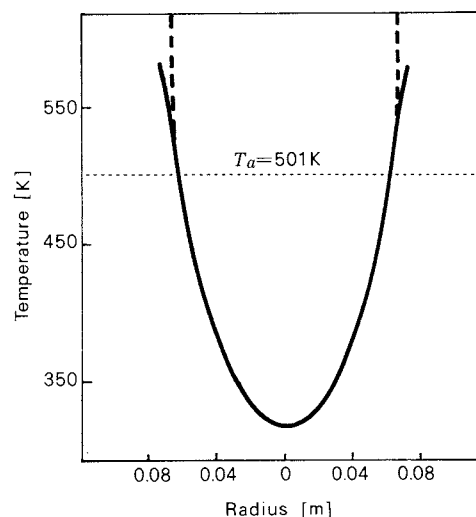


Fig. 8(a) Temperature profile of cork dust deposit showing the moment immediate before the ignition at  $T_a = 501$  K. Solid line refers to the values after 1.08 h; dashed line refers to the values after 1.086 h

enough (for instance, at  $T_a = 501$  K), appropriate simulation was not obtained for the reasons described below. However, the results of the calculation shown in Fig. 8(a) suggest some pertinent information. When  $T_a = 501$  K, the external surface of the cylindrical dust deposit is heated by the surrounding air, and its temperature rises high enough to accelerate the reaction. In addition, the thermal conductivity is very low. As a result, spontaneous ignition occurs at a position adjacent to the external surface. In this case, a very large value of  $h =$

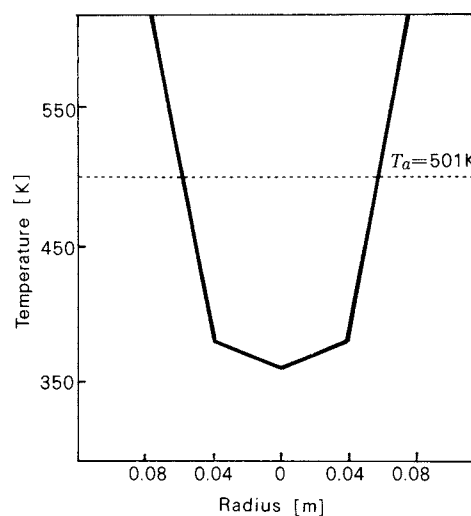


Fig. 8(b) The corresponding experimental data to Fig. 8(a) reported by Leuschke at  $T_a = 501$  K

$1.67 \times 10^6 \text{ J} \cdot \text{m}^{-2} \cdot \text{h}^{-1} \cdot \text{K}^{-1}$  was used so that the induction time would coincide with the measured value. However, the inclination of the graphs was independent of the  $h$  values used. Comparing Fig. 8(a) to (b) reveals that this inclination is similar to the inclination in the experimental results reported by Leuschke.

## 2) Induction time to ignition

The time that elapsed from when the deposit was placed in an environment the temperature of which is  $T_a$  to the time when spontaneous ignition occurred is defined as induction time  $\theta_i$ . The induction time 15.4 h at ambient temperature  $T_a = 414\text{K}$  is read from Fig. 4(a), and 5.5 h at  $T_a = 444\text{K}$  is from Fig. 6(a). By comparing these values to those shown in Figs. 4(b) and 6(b), it is found that  $\theta_i$  obtained by this method of calculation coincides approximately with that reported by Leuschke.

Simulation for the case when  $T_a = 501\text{K}$  is carried out using the combined heat transfer coefficient obtained by Eq. (4). Since the obtained induction time is longer than that reported by Leuschke ( $\theta_i \approx 0.7\text{h}$ ), values of the combined heat transfer coefficient (up to  $1.67 \times 10^6 \text{ J} \cdot \text{m}^{-2} \cdot \text{h}^{-1} \cdot \text{K}^{-1}$ ), larger than the  $h$  value obtained by Eq. (4), are used to recalculate the induction time. It was impossible to obtain a calculation value of the induction time equivalent to the experimental value by only increasing the  $h$  value. The most difficult problem is that under the calculation conditions used in this report, if  $T_a$  is higher than the ignition temperature by 100 K, the time period required for the temperature at the circumferential surface of the sample to reach a predetermined temperature of  $T_a$  is longer than that of the experimental data reported by Leuschke. This is in spite of extreme enlargement of the  $h$  value. Therefore, simulating a case using a relatively high ambient temperature is considered to be impossible at this stage. However, it was found that the temperature profiles at the moment immediately proceeding the ignition had the same inclination irrespective of the  $h$  values when  $T_a = 501\text{K}$ . Therefore, the qualitative explanation shown in Fig. 8(a) is applicable where the ambient temperature is relatively high.

The above calculation results show that

when the ambient temperature  $T_a = 408\text{K}$ , spontaneous ignition does not occur; however, if  $T_a$  rises to 414 K or higher, spontaneous ignition occurs. These calculation results satisfactorily agree with the experimental results. Therefore, a critical temperature  $T_{si}$  (self-ignition temperature) is considered to exist between 408 K and 414 K. When  $T_a < T_{si}$ , spontaneous ignition does not occur, but if  $T_a > T_{si}$ , spontaneous ignition does. This  $T_{si}$  is defined as the self-ignition temperature in this study, the same as in the report by Leuschke. Hereafter, the self-ignition temperature  $T_{si}$  and the induction time  $\theta_i$  are used as operational variables that directly suppress the danger of spontaneous ignition.

## 3. 2 Scaled-up dust deposits

### 1) Dependency of the self-ignition temperature on the dust deposit volume

The self-ignition temperature  $T_{si}$  was obtained by varying the volume of dust deposit from  $5.0 \times 10^{-5} \text{ m}^3$  (radius  $R_1 = 0.02 \text{ m}$ ) to  $10 \text{ m}^3$  (radius  $R_1 = 1.17 \text{ m}$ ). Figure 9 shows the relationship between the obtained self-ignition temperature and the dust volume. In this figure, the closed circles are experimental values reported by Leuschke<sup>6)</sup> and obtained by using cork dust deposits, and the open circles are the values simulated by the authors. The solid line expresses the simulated values. The simulated values satisfactorily coincide with the experimental values in a wide range of volumes.

### 2) Dependency of induction time on the dust deposit volume

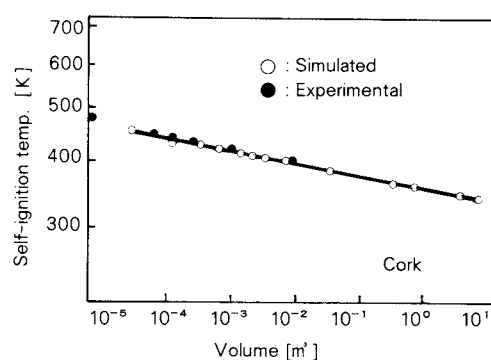


Fig. 9 Dependency of self-ignition temperature upon the cork dust volume



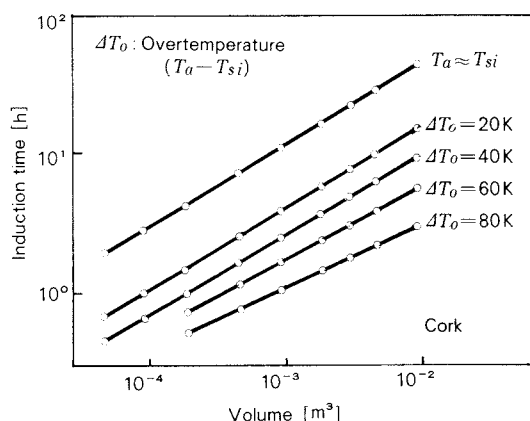


Fig. 10 The induction time to ignition simulated at different overtemperatures as a function of the cork dust volume

To compare our results to the experimental values reported by Leuschke, the difference ( $T_a - T_{si}$ ) is defined as an overtemperature  $\Delta T_o$ <sup>4)</sup>. The variation in the induction time  $\theta_i$  at a constant  $\Delta T_o$  is calculated by varying the dust deposit volume. **Figure 10** illustrates the results obtained. Since the relationship between the induction time and dust deposit volume is linear on a double logarithm graph,  $\theta_i$  is in proportion to a certain power of the dust deposit volume at a specific overtemperature  $\Delta T_o$ . On the other hand, Leuschke experimentally obtained the relationship between the dust deposit volume and  $\theta_i$  not only for cork dust but also for tobacco dust at a constant  $\Delta T_o$ . Since the experimental data for the cork dust is not disclosed in the report, the experimental data on tobacco dust is shown in **Fig.**

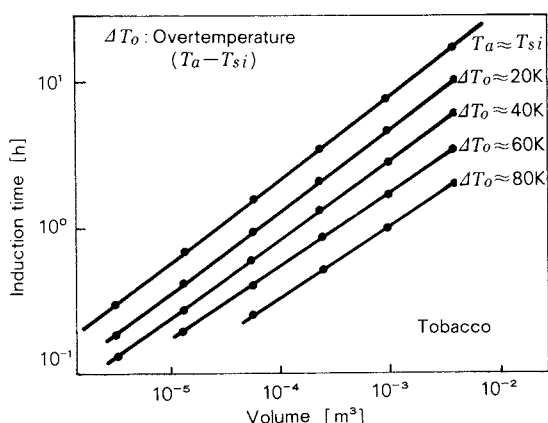


Fig. 11 The experimental induction time to ignition reported by Leuschke at different overtemperatures as a function of the tobacco dust volume

11. (Leuschke reported that the results obtained for the cork dust deposit had an inclination similar to the results obtained for the tobacco dust deposit.) Therefore, our simulation results cannot be directly compared to the experimental data reported by Leuschke, however, these figures show similar inclinations.

#### 4. Conclusions

The above described method of calculation can determine the self-ignition temperature with an approximate accuracy, except for cases where the ambient temperature is extremely high. If possible, it would be desirable to obtain  $T_{si}$  using an equation. The temperature profile is not stationary during the initial state but finally reaches a steady state, as shown in **Fig. 1**. It is necessary to discuss whether or not  $T_{si}$  is equal to  $T_a$ , obtained by replacing the left side of Eq. (2) with zero and by solving the quadratic ordinary differential equation.

The concept used in this study for the balance between heat generation and dissipation is basically the same as the stability criteria for the reaction apparatus. However, most studies on the criteria handle primary reactions as a perfectly mixed system. The analysis used in this study differs from those with respect to the method of analysis and its purposes.

As described above, the results obtained by our method of calculation satisfactorily agree with the results of the experimental data reported by Leuschke, thus suggesting that simulation of the spontaneous ignition of dust deposits is possible.

#### Acknowledgment

The authors wish to gratefully acknowledge the help and advice in this study of our colleague, Yōji Nakajima.

#### Nomenclature

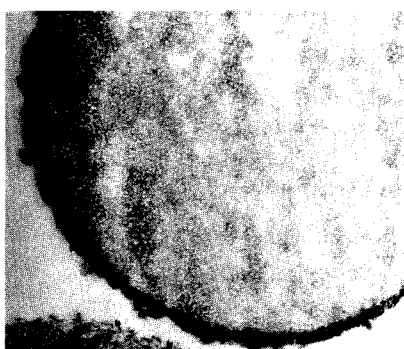
$C$	: specific heat of the sample	$[\text{J} \cdot \text{kg}^{-1} \cdot \text{K}^{-1}]$
$E$	: activation energy	$[\text{J} \cdot \text{mol}^{-1}]$
$f$	: frequency factor of chemical reaction rate	$[\text{kg} \cdot \text{m}^{-3} \cdot \text{h}^{-1}]$
$h$	: combined heat transfer coefficient	$[\text{J} \cdot \text{h}^{-1} \cdot \text{m}^{-2} \cdot \text{K}^{-1}]$
$k$	: thermal conductivity of the sample	$[\text{J} \cdot \text{h}^{-1} \cdot \text{m}^{-1} \cdot \text{K}^{-1}]$
$Q$	: heat of reaction	$[\text{J} \cdot \text{kg}^{-1}]$
$q$	: rate of heat evolution per unit	

volume	$[J \cdot h^{-1} \cdot m^{-3}]$
$R$ : gas law constant	$[J \cdot K^{-1} \cdot mol^{-1}]$
$R_1$ : radius of cylinder	$[m]$
$\tau$ : radial distance in cylindrical coordinates	$[m]$
$T$ : absolute temperature	$[K]$
$T_a$ : ambient temperature	$[K]$
$T_b$ : temperature near the border of the sample	$[K]$
$T_h$ : temperature halfway between the middle and border of the sample	$[K]$
$T_m$ : temperature in the middle of the sample	$[K]$
$T_r$ : room temperature	$[K]$
$T_R$ : temperature at the border of the sample	$[K]$
$T_{si}$ : self-ignition temperature	$[K]$
$\rho$ : density of the sample	$[kg \cdot m^{-3}]$
$\theta$ : storage time	$[h]$
$\theta_i$ : induction time to ignition	$[h]$

## References

- 1) Bowes, P. C. and S. E. Townshend: *Brit. J. Appl. Phys.*, **13**, 105 ~ 114 (1962).
- 2) Fujita, S.: "Kagaku-Kogaku I", Iwanami-Zensho (1963).
- 3) The Society of Chemical Engineers, Japan, ed.: "Kagaku-Kogaku Binran", Maruzen (1958).
- 4) Leuschke, G.: Vortrag auf dem 5. Internationalen Brandschutz-Seminar Karlsruhe, Band I, S. 145 ~ 159 (1976).
- 5) Leuschke, G.: 3rd Int. Symposium on Loss Prevention and Safety, Promotion in the Process Industries, Basle/Switzerland, 2, 647 ~ 656 (1980).
- 6) Leuschke, G.: *Inst. Chem. Eng. Symposium Series*, No. 68 (1981).
- 7) Segerlind L. J.: "Applied Finite Element Analysis", translated by Kawai, T., Maruzen (1978).

## Explanation of the cover photograph



Hosokawa Micron Corp. has recently developed the Mechanofusion<sup>®</sup> System. Mechanofusion<sup>®</sup> is a novel technology for creating new particulate materials. The mechano-chemical reaction upon two or more materials, through the application of mechanical energy, generates a new material with new physical and chemical properties.

The cover photograph, obtained by the transmission electron microscope (TEM), shows a cross-sectional view of fine particles after mechanofusion treatment. It shows the results of multi-layered mechanofusion treatment of ultrafine particles of titanium dioxide and red iron oxide on the surface of silica spheres.

(average particle diameter:  $5\mu m$ )

# Mechano-chemical Effects of One-dimensional Explosive Shock Treatment on the Characteristics of $\text{Si}_3\text{N}_4$ <sup>†</sup>

Fumikazu Ikazaki, Kunio Kamiya,  
Kunio Uchida, Akihiro Goto,  
Mitsutaka Kawamura, Katsumi Tanaka  
and Shuzo Fujiwara

National Chemical Laboratory  
for Industry, AIST, MITI,  
Tsukuba Research Center\*

## Abstract

*Direct consolidation of  $\alpha$ - and  $\beta$ - $\text{Si}_3\text{N}_4$  is conducted by the use of one-dimensional explosive shock treatment. The effect of shock pressure, phase and particle size distribution of a sample powder on the characteristics of the explosively shocked compact is examined by the measurement with X-ray diffraction (XRD), Electron spin resonance (ESR), and Infrared absorption (IR) among others. The following are the results:*

- 1) *Cracks exist in the shock compact. The apparent density and Vickers hardness increase with the increase in shock pressure. A compact of ca. 90% theoretical density is obtained.*
- 2) *Residual strain by XRD and spin density by ESR are reduced under higher shock pressures. This is considered to be attributed to the relaxation effect of high residual temperature. The shock compact of  $\alpha$ - $\text{Si}_3\text{N}_4$  receives more residual strain and spin density than that of  $\beta$ - $\text{Si}_3\text{N}_4$ .*
- 3) *The effect of particle size distribution of the sample powder on the characteristics of the shock compact is slight. The shock compact of larger particle size has more residual strain.*
- 4) *Metal impurities are not found except in the surface layer of the compact.*
- 5) *The solubility of the powder grinding shock compact in 1N-NaOH is higher than that of the as-received powder. This indicates that an active surface layer exists in the shock compact.*
- 6) *The tapping density of the powder grinding shock compact is much higher than that of the as-received powder.*

## 1. Introduction

When an explosive energy is applied to a layer of powder, the force that the layer receives reaches an extraordinarily high pressure

expressed in tens of GPa, which lasts about a microsecond. Attempts are being made to produce substances, which are not obtainable by any ordinary method, by utilizing dynamic extraordinarily powerful pressure. Such attempts are successful in synthesizing diamonds and cubic crystal  $\text{BN}$ <sup>1)</sup>. Besides this, explosive shocks are utilized to modify the characteristics of powder substances, as well as to improve sinterability, solidification, and the fusion of metals, etc.

\* 1-1, Higashi, Yatabe-cho, Tsukuba-gun, Ibaraki, 305  
TEL. 0298 (54) 4728

† This report was originally printed in *J. Soc. Powder Technology, Japan*, **23**, 250-257 (1986) in Japanese, before being translated into English with the permission of the editorial committee of the Soc. Powder Technology, Japan.

The modification of the characteristics and the change in the phase transition temperature of  $\text{TiO}_2$  and  $\text{ZrO}_2$  powders by the use of explosive shock treatment have already been reported on<sup>2,3)</sup>. This paper is concerned with the direct consolidation of silicon nitride ( $\text{Si}_3\text{N}_4$ ), which is believed to have a bright future as a high temperature resistant structural material. Graham et al.<sup>4)</sup> reported on the lattice defect of the crystal structure in the explosive shock treatment of  $\text{Si}_3\text{N}_4$  by using the X-ray diffraction (XRD) method and Electron Spin Resonance (ESR), while Beauchamp et al.<sup>5)</sup> described the influence of explosive shocks on the transition from phase  $\alpha$  to  $\beta$ . On the other hand, Kanno et al.<sup>6,7)</sup> reported, based on measurement by XRD, temperature controlled  $\text{NH}_3$  desorption that  $\text{Si}_3\text{N}_4$  powder is activated and that the mechano-chemical effect that the powder receives from the explosive shock treatment is different from that given by ball-mill grinding. However, none of these reports clarified the influences of shock pressure, crystal phase and particle size distribution of a sample powder upon the characteristics of an explosive shock compact or those of the powder grinding the compact. Nor has there been any mention of the amount of metal impurities in the shocked compact nor of the packing property of the powder grinding the compact.

This report provides data on the characteristics of an explosive shock compact and on its pulverized powder, particularly with respect to points which were previously unclarified.

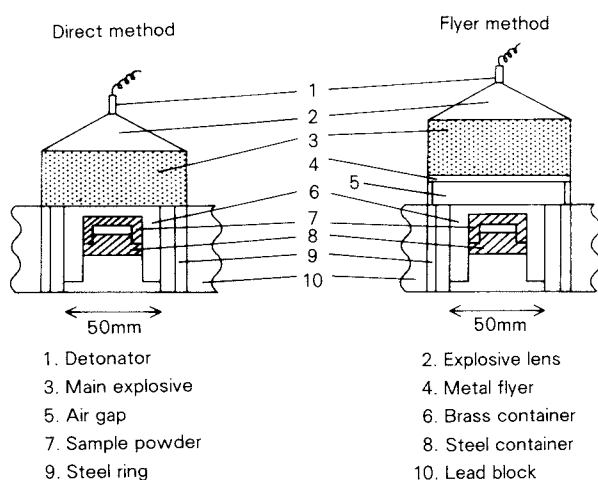


Fig. 1 Experimental setup

Table 1 Characteristics of  $\text{Si}_3\text{N}_4$

$\alpha\text{-Si}_3\text{N}_4$	$\beta\text{-Si}_3\text{N}_4$
$\alpha$	90% $\beta$
1.10 $\mu\text{m}$ (FSSS)	approx. 2 $\mu\text{m}$

## 2. Apparatus and method

Figure 1 illustrates the apparatuses used for one-dimensional explosive shock treatment. The method used in the experiment is the same as that in the previous paper<sup>2,3)</sup>. The shock pressures used are approx. 10 GPa by a direct method using nitromethane, approx. 20 GPa by a direct method using hexogen, and approx. 30 GPa by the Flyer method\*. Both  $\alpha$ - and  $\beta\text{-Si}_3\text{N}_4$  as sample powders were used, as shown in Table 1 for characteristics (given by companies). With a view to examining the influence of the particle size distribution, the  $\alpha$  phase sample was classified (Acucut by Donaldson Co.) into two different cut sizes, 1.5 microns and the 10 microns. The experiments were carried out with three kinds of sample powders including the as-received sample powder which was not subjected to the classification. The curves in Fig. 2 represent the particle size distributions of the three sample powders. The initial packing fractions of  $\alpha$ - and  $\beta\text{-Si}_3\text{N}_4$  in the steel sample container are 50% and 60%, respectively.

After explosive shock treatment, the compacted sample was recovered in the state of being packed in the steel sample container. This vessel was melted with nitric acid to examine the compact inside. The items examined and the methods applied were as follows:

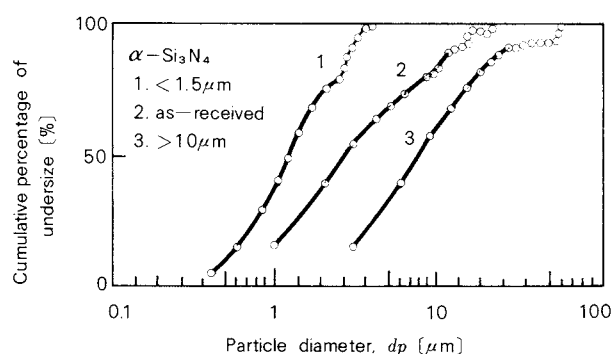


Fig. 2 Particle size distribution of sample powder

\* Only 20 GPa and 30 GPa were applied to the  $\alpha$  phase sample.

(1) The content of metal impurities . . . . . While Al, Fe, Mg, Ca, Na, K, etc. were analyzed by means of the inductively coupled plasma method (ICP) and atomic absorption method, the change in the concentrations of the impurities in the direction of the depth was measured by means of an X-ray microanalyzer (XMA) and ion microanalyzer (IMA).

(2) Hardness . . . . . After the shocked compact was polished with a diamond, the Vickers hardness was measured at room temperature.

(3) The apparent density . . . . . Archimedes method was applied using water as the solvent.

(4) The residual strain and crystallite size . . . . . Hall's method was applied by the use of an X-ray diffraction apparatus (Rotor Flex with a monochromator made by Rigaku Electric Co.). Silicon fired under nitrogen gas at 740°C for 15 hours was used as a standard material.

5) The lone pair electron (LPE) concentration . . . . . The LPE concentration was determined by ESR (E-12 with a twin cavity made by Varian Co.). 1-1-diphenyl-2-picrylhydrazyl (DPPH) was employed as a standard material. For the precision measurement of the spectroscopic splitting factor  $g$ -value, TEMPOL (2,2,6,6-tetramethyl-4-piperdinol) was used, because it is known to give split line profiles at points 15.36 Gauss away from the center where  $g = 2.0061$ .

(6) The infrared absorption spectrum . . . . . The KBr method<sup>8)</sup> using KSCN as an internal standard was used for the measurement.

(7) The analysis of the surface conditions . . . . . The surface was examined by SEM, and the O/N ratio was measured by the use of an X-ray photoelectron spectroscopy (XPS, model ASIX-1000 made by Shimadzu Co.)

### 3. Results and discussion

Shock-compacted silicon nitride assumed a dark shade when compared with the sample

$\alpha$ -Si<sub>3</sub>N<sub>4</sub>,  $\epsilon = 0.5$   
no classification  
Flyer, ca. 30 GPa

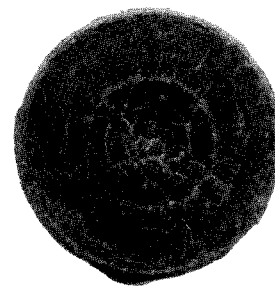


Fig. 3 Photograph of recovered Si<sub>3</sub>N<sub>4</sub>

powder. Cracks were observed on the surface of the shocked compact. **Figure 3** shows a photograph of such a compact after recovery.

#### 3. 1 Hardness and apparent density

**Table 2** shows the results. The hardness values shown represent averages obtained at 10 through 15 points. The Vickers hardness of both  $\alpha$ - and  $\beta$ -Si<sub>3</sub>N<sub>4</sub> increases with the increase in the shock pressure. The hardness of the  $\alpha$  type is larger on the whole than the  $\beta$  type. The influence of the particle size distribution of the starting powder was shown as an increase in Vickers hardness in accordance with the increase in the average particle size at the pressure of 20 GPa, but the Vickers hardness showed no difference when the shock pressure was 30 GPa. It is considered that, for the same shock pressure, the shock pressure at one contact point becomes larger when the average particle size is larger. Considering that the Vickers hardness of 2300 kg/mm<sup>2</sup> for a shock pressure of 30 GPa is larger than the value<sup>9)</sup> when Si<sub>3</sub>N<sub>4</sub> was hot pressed, probably the difference in particle size distribution did not have a significant effect on the Vickers hardness at 30 GPa. On the other hand, the value of the apparent density was not very accurate because of the existence of cracks, but these values showed that the sample powders can be

Table 2 Vickers hardness and apparent density of explosively shocked Si<sub>3</sub>N<sub>4</sub>

	Vickers hardness [kg/mm <sup>2</sup> ]				Apparent density [g/cm <sup>3</sup> ]			
	$\alpha$ -type		$\beta$ -type		$\alpha$ -type		$\beta$ -type	
	< 1.5 $\mu$ m	as-received	> 10 $\mu$ m	as-received	< 1.5 $\mu$ m	as-received	> 10 $\mu$ m	as-received
10 GPa	—	—	—	235	—	—	—	2.75
20 GPa	1650	1840	1930	553	—	—	—	2.95
30 GPa	2300	2390	2310	812	2.74	2.53	2.71	2.99



consolidated up to approx. 90% of their theoretical density ( $3.19 \text{ g/cm}^3$ ).

### 3. 2 Crystalline properties (Residual strain etc.)

**Table 3** shows the results of tests obtained using the X-ray diffraction (XRD) method. In **Table 3**,  $\alpha$ - $\text{Si}_3\text{N}_4$ , the recovered specimens at a pressure of 20 GPa applied to the as-received powder were too small to measure quantitatively. The crystalline property of the  $\beta$  type-intact was so perfect that no data was obtainable. When the  $\beta$ - $\text{Si}_3\text{N}_4$  (the stable phase at a high temperature) is compared with the  $\alpha$ , the crystallite sizes of the  $\beta$  are larger, and the residual strains are smaller. The differences are not conspicuous between the three sample powders having different particle size distributions. However, the residual strain, shown in the table, is largest where the particle size of the sample powder is the largest and is the smallest where the particle size is less than 1.5 microns. The same reason as mentioned above with respect to hardness seems to apply to this case as well. The table shows that the residual strain at 20 GPa was larger than that at 30 GPa. This is probably because of the relaxation effect that occurred as a result of the increase in the residual temperature caused by the shock. On the other hand, the residual strain of the  $\beta$  type was almost the same as for 20 GPa and 30 GPa. It follows from these results that the

residual strain does not necessarily increase when the shock pressure increases and that the relaxation effect which works when the residual temperature increases, must be taken into consideration as well. It is considered that because the initial packing fraction is different between the  $\alpha$  and  $\beta$  types, the residual temperature\* is higher when the  $\alpha$  type having a smaller packing fraction is shock-treated. The strain is probably reduced by using the Flyer method (30 GPa) on the  $\alpha$ - $\text{Si}_3\text{N}_4$  due to the relaxation effect that works depending on the residual temperature.

**Table 4** shows the results of lone-pair electron (LPE) concentration. What is measured is the first differential form of the absorption spectrum, an example of which is shown in **Fig. 4**. As will be seen from **Table 4**, the concentration has a tendency to lower when the shock pressure increases. A comparison of  $\alpha$  with  $\beta$  shows that the concentration of the former is higher. Accordingly, the tendency of the residual strain being taken into account,  $\beta$ - $\text{Si}_3\text{N}_4$  can be said to be more stable to shock pressure than  $\alpha$ - $\text{Si}_3\text{N}_4$ . The spin density (LPE concn-

\* The estimation of the residual temperature requires HUGONIOT data that describes the relationship between the shock pressure and the volume for the same sample powder at the same packing fraction. The approximate residual temperatures based on the HUGONIOT data for SiC, applied to the Flyer method using hexogen, were estimated to be 1800-2800K for a packing fraction of 60% and 1900-3300K for a packing fraction of 50% (No HUGONIOT data are available for  $\text{Si}_3\text{N}_4$ ).

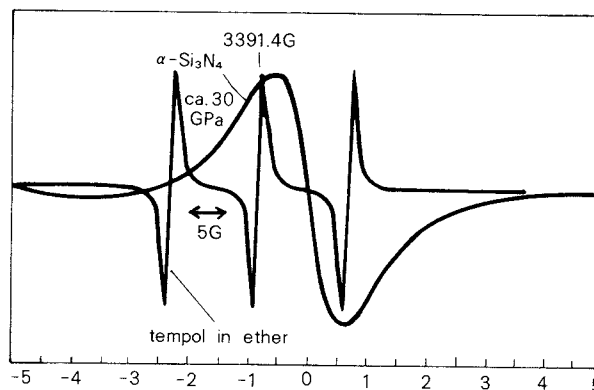


Fig. 4 ESR spectrum of explosively shocked  $\text{Si}_3\text{N}_4$

Table 3 Residual strain and crystallite size of explosively shocked  $\text{Si}_3\text{N}_4$

	$\alpha$ -type						$\beta$ -type	
	< 1.5 $\mu\text{m}$		as-received		> 10 $\mu\text{m}$		as-received	
	$d_c$ [ $\text{\AA}$ ]	$\epsilon$ [-]	$d_c$ [ $\text{\AA}$ ]	$\epsilon$ [-]	$d_c$ [ $\text{\AA}$ ]	$\epsilon$ [-]	$d_c$ [ $\text{\AA}$ ]	$\epsilon$ [-]
intact	750	$\cong 0$	740	$4.6 \times 10^{-4}$	720	$\cong 0$	—	—
10 GPa	—	—	—	—	—	—	2000	$1.5 \times 10^{-3}$
20 GPa	500	$5.0 \times 10^{-3}$	—	—	660	$6.0 \times 10^{-3}$	2000	$2.4 \times 10^{-3}$
30 GPa	460	$4.0 \times 10^{-3}$	630	$4.4 \times 10^{-3}$	660	$5.0 \times 10^{-3}$	1880	$2.4 \times 10^{-3}$

Table 4 Spin density,  $g$ -value and  $\Delta H_{p-p}$  of explosively shocked  $\text{Si}_3\text{N}_4$

		Spindensity [ $\times 10^{18} \text{g}^{-1}$ ]	$g$ -value	$H_{p-p}$ [G]
$\alpha$ - $\text{Si}_3\text{N}_4$	( $> 10 \mu\text{m}$ )			
	20 GPa	2.3	2.0014	12.3
	30 GPa	1.8	2.0011	13.1
	(as-received)			
	20 GPa		2.0013	13.0
	30 GPa	1.3	2.0012	12.3
	( $< 1.5 \mu\text{m}$ )			
	20 GPa	3.0	2.0014	13.0
	30 GPa	2.0	2.0025	10.8
$\beta$ - $\text{Si}_3\text{N}_4$	10 GPa	1.6	2.0021	7.1
	20 GPa	1.6	2.0021	7.3
	30 GPa	1.1	2.0020	7.4
SN 502	10 GPa	0.16	—	—
	30 GPa	0.11	2.0029	9.0

tration), being in the order of  $10^{18}$ , coincides as a whole with the values provided by Graham et al.<sup>6)</sup>. The ESR spectrum of the original sample of the  $\beta$ - $\text{Si}_3\text{N}_4$  was so weak that the concentration was not determined. According to Graham et al.<sup>6)</sup>, the value was in the order of  $10^{16}$ . The spin density became two orders of magnitude higher when using the shock treatment.

The  $g$  value as a spectroscopic splitting factor was not changed so much by the shock pressure. The value varies with the specimen, being 2.0029 when silicon nitride SN502 (a product of Sylvania Co.) was measured. Figure 5 shows the relationship between the spin density and the peak-to-peak magnetic field intensity of the measured spectrum ( $\Delta H_{p-p}$ ). This diagram clearly manifests the difference in ESR spectrum characteristics which exists depending on the starting material. The ESR spectrum of silicon nitride was compared with a spectrum of shock-treated Si to examine the cause of the former spectrum.  $\Delta H_{p-p}$  is larger, and the ESR spectrum of the shocked  $\text{Si}_3\text{N}_4$  contains the spectrum of Si, although the  $g$ -value ( $g$ -value of Si=2.0051) is clearly different. Considering this, it can be said that the dangling bond of Si alone, as in the case of a thin film of silicon nitride in the CVD method, is not the cause<sup>10)</sup>, but ESR absorption from the dangling bond of N also occurs.

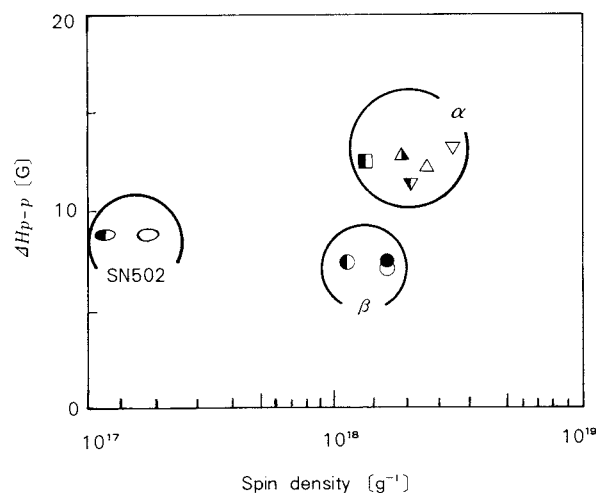


Fig. 5 Spin density vs.  $\Delta H_{p-p}$

### 3. 3 Metal impurities

One of the advantages of explosive shock treatment as a method of pulverizing materials is said that the process permits less impurities to enter the processed materials than other methods of pulverization. However, there has been no report which gives data through analysis concerning the content of impurities before or after the treatment. Table 5 shows the results of analysis in this respect. The values given in column A1 of the  $\alpha$  type represent the metal impurities of the original sample. A2 and A3 represent the corresponding values of classified sample powder. The classification by Acucut contaminated the original powder with Fe from the classification unit. B1 ~ B8 represent the values after the shock treatment. The values of Al, Fe and Mg, etc. are noticeably high. The pronounced increases in Al, despite the use of an iron vessel (D2), gave rise to a doubt. After analyzing the grinding balls made of silicon nitride, Al, Mg, etc. were found in substantial quantities, as shown by D1. It is considered that the metal impurities from the silicon nitride balls, which had been made with  $\text{Al}_2\text{O}_3$  and MgO as sintering additives, contaminated the original sample powder, as shown by B1 ~ B8. As a result of analyzing a shocked compact of a different kind of  $\text{Si}_3\text{N}_4$  powder (SN502) without grinding it, it was found that few metal impurities were present in the central part, and only Fe increased in the peripheral portions. This indicates that, even when harder grinding balls are used, pulveriza-

Table 5 Spectrochemical analysis of  $\text{Si}_3\text{N}_4$

[wt ppm]

No.	Sample	Al	Fe	Ca	Mg	Na	K	Ni
A1	$\alpha\text{-Si}_3\text{N}_4$ as-received	(82) 137	(90) 134	(109)	(8) 9	31	13	
A2	< 1.5 $\mu\text{m}$	182	431		12	58	17	
A3	> 10 $\mu\text{m}$	156	336		14	32	20	
B1	$\beta\text{-Si}_3\text{N}_4$ 10 GPa	1277	1426		62	134	77	
B2	20 GPa	1220	1545		15	260	61	
B3	30 GPa	1572	2655		119	245	119	
B4	$\alpha\text{-Si}_3\text{N}_4$ 20 GPa < 1.5 $\mu\text{m}$	609	3849	152	154	126	76	
B5	> 10 $\mu\text{m}$	755	3571	145	200	116	58	
B6	30 GPa as-received	1201	5037		258	293	105	
B7	< 1.5 $\mu\text{m}$	3272	5473		1023	184	86	
B8	> 10 $\mu\text{m}$	2148	5707	201	547	201	144	
C1	SN 502 center	47	94	47	9	90	54	54
C2	periphery	49	740	49	10	84	30	94
D1	grinding ball ( $\text{Si}_3\text{N}_4$ )	42023	4041	1778	12138	307	44	
D2	container (Fe)	23		17				
E1	grinding ball (stainless)	872	208333	291	43			40698
E2	after acid cleaning	125	62	156	20			62

Figures in the bracket are presented from the company.

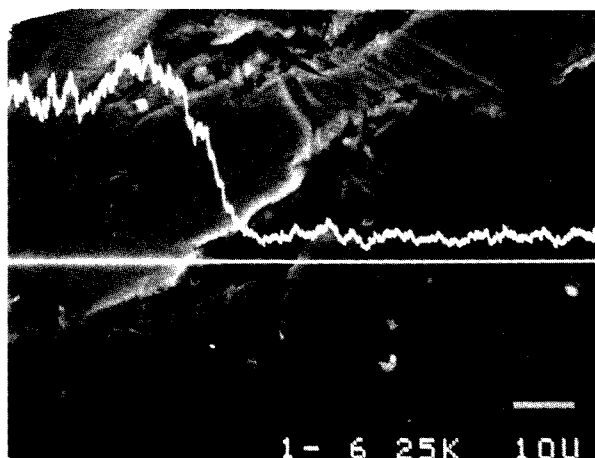


Fig. 6 Line analysis by XMA

tion is unavoidable as a result of friction of one against another of the same kind, and the ground product is mixed as impurities. A suitable method of grinding, therefore, is to grind with iron or stainless balls and to clean the ground product with acid. As shown by E1 and E2 in the table, the application of this method prevents the ground product from being mixed with metal impurities.

Besides the chemical analysis, analysis by the

use of XMA and IMA were also introduced in the studies on the presence of impurities. **Figure 6** shows an example of the results of line analysis by XMA. The vessel was made of stainless steel, and a technique of scanning analysis with Ni was employed. The Ni signal showed a sharp fall as the scanning moved from the vessel in the left to the specimen in the right. Scanning thus proved that the specimen was not mixed with impurities. However, since the analyzing beam of XMA has a diameter of only several microns, the analysis fails to observe the change at the surface of the shocked compact. **Figure 7** shows an example of the analysis by IMA that compensated for the failure. Concentrations in the depth direction are represented on the horizontal axis and considered to be in the order of several hundreds of angstroms at most. **Figure 7** indicates that impurities are present in various quantities from spot to spot, and the quantities decrease sharply in the depth direction. A judgment summarizing these results together with the results of the chemical analysis is that metal impurities are present to some degree at the surface but not present in the internal part.

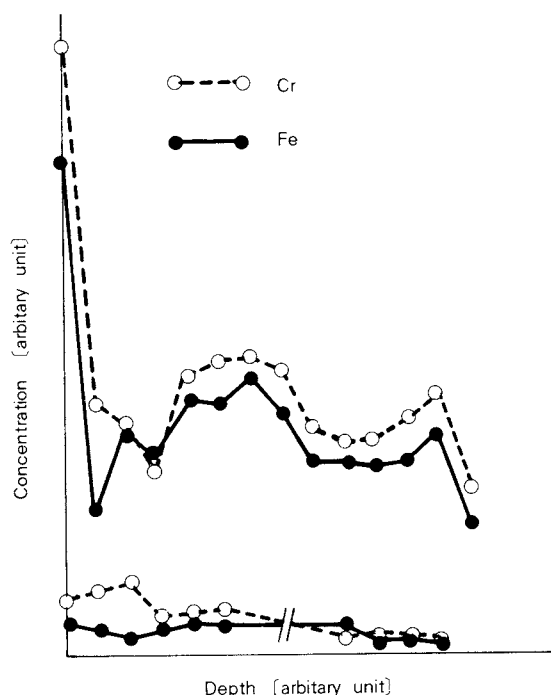


Fig. 7 Concentration of Fe and Cr in the depth — direction by IMA

### 3. 4 Observation of the surface and the presence of a surface-active layer

Figure 8 and 9 show photographs of the  $\beta$  type by SEM. There is no clear evidence of sintering of the original sample powder for explosive shock treatment at 10 GPa, but for treatment at 20 GPa or more there is clear evidence of sintering between particles and of grain boundaries.

The solubility of Si at the surface was examined. Approximately 100 mg of ground  $\alpha$ - $\text{Si}_3\text{N}_4$  was put in 10 ml of 1N-NaOH and was left standing for four hours at 90°C. Dissolved Si was analyzed by ICP. Dissolved Si of SN502 containing an amorphous phase was also analyzed. Table 6 shows the solubility of Si in 1N-NaOH. The solubility of Si increased through explosive shock treatment with respect to both  $\alpha$ - $\text{Si}_3\text{N}_4$  and SN502.

On the other hand, the shock-treated  $\alpha$ - $\text{Si}_3\text{N}_4$  and the sample powder were left standing in a 50% HF solution for a certain time and were then analyzed by the infrared absorption spectrum using the KBr method. Potassium thiocyanate (KSCN) was used as an internal

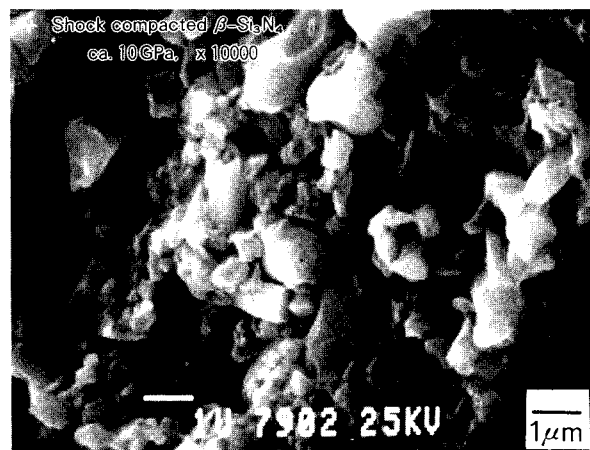


Fig. 8 SEM of explosively shocked  $\text{Si}_3\text{N}_4$  ( $\beta$ - $\text{Si}_3\text{N}_4$ , ca. 10 GPa)



Fig. 9 SEM of explosively shocked  $\text{Si}_3\text{N}_4$  ( $\beta$ - $\text{Si}_3\text{N}_4$ , ca. 30 GPa)

Table 6 Solubility of  $\text{Si}_3\text{N}_4$  in 1N-NaOH [%]

	$\alpha$ - $\text{Si}_3\text{N}_4$			SN 502
	< 1.5 $\mu\text{m}$	as-received	> 10 $\mu\text{m}$	
untreated	4.36	1.95	2.20	1.52
20 GPa	4.43	2.20	5.03	6.61
30 GPa	7.53	3.89	4.56	5.01

standard. Figure 10 shows the results. Both spectrums show absorption<sup>11)</sup> at 900 ~ 1000  $\text{cm}^{-1}$  and 400 ~ 600  $\text{cm}^{-1}$  peculiar to Si-N, but the shock-treated specimen shows smaller absorption. Figure 11 shows the absorbance ratio as a function of the standing time in the

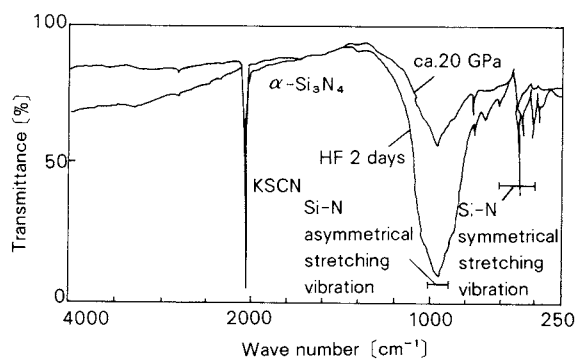


Fig. 10 IR spectrum of explosively shocked  $\text{Si}_3\text{N}_4$

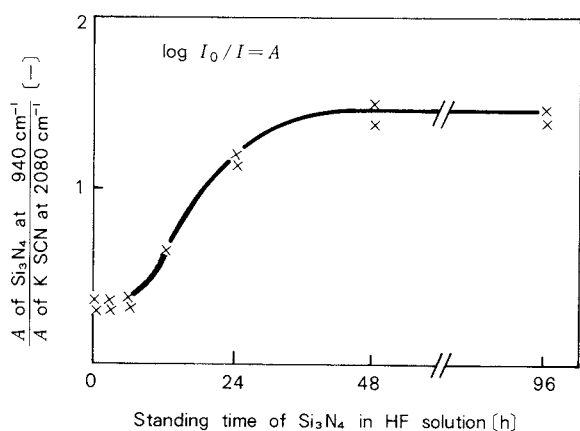


Fig. 11 Effect of standing time in HF solution of explosively shocked  $\text{Si}_3\text{N}_4$  on absorbance ratio

HF solution. The absorbance shows a recovery with time standing in the HF solution and becomes similar to the spectrum of the original sample which had not been shock-treated.

The shock-treated material did not show any noticeable increase in the quantity of oxygen but the solubility of Si of the shocked  $\text{Si}_3\text{N}_4$  increased. As a result, the change in the IR spectrum is not attributed to the oxidation layer but rather to the active layer (lattice defect layer) at and near the surface based on the strain caused by the explosive shock pressure.

The active layer weakened the intensity of the absorption spectrum peculiar to Si-N, but the surface conditions of the original sample were recovered as the surface-active layer was dissolved in HF.

### 3. 5 The influence of explosive shock treatment on the packing property of powders

Graham et al. reported<sup>4)</sup> that  $\text{Si}_3\text{N}_4$  powder obtained by pulverizing an explosive shock compact has a good fluidity. Also Bergmann et al.<sup>12)</sup>, clarified that the shocked treatment of  $\text{Al}_2\text{O}_3$ , Sic, etc., markedly increased the packing density. However, the improvement of the fluidity, as reported by Graham et al., is attributed to the large particle size of the powder (the median diameter is approx. 60 microns) after shock treatment as compared with 8.2 microns before the shock treatment. On the other hand, in the report of Bergmann et al., the particle size became smaller after the shock treatment. They said that the improvement of the packing property is due to the particle size distribution which has become suitable for packing after the treatment, but they have not yet clarified what distribution is suitable for packing.

To examine the packing properties, the tapping density was measured by the use of the  $\alpha\text{-Si}_3\text{N}_4$  powder with a particle size of 10 microns or more. The original sample powder has almost the same particle size as the ground powder of the shocked compact. Figure 12 shows the results. Certainly, the shock treated powders show larger tapping densities. As

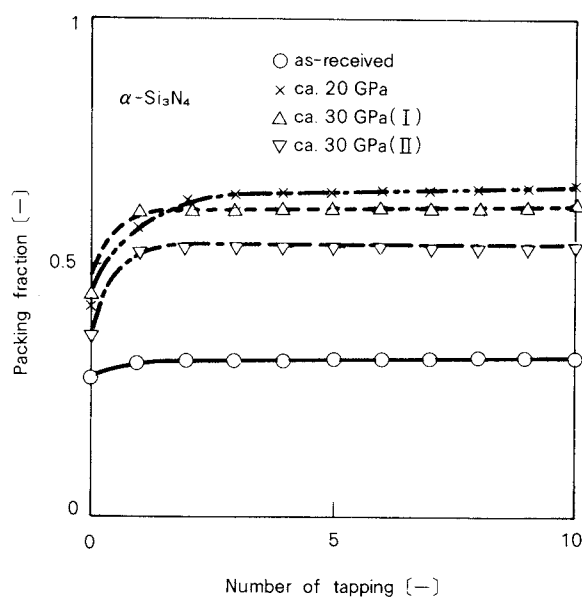


Fig. 12 Tapping density of as-received and explosively shocked  $\text{Si}_3\text{N}_4$



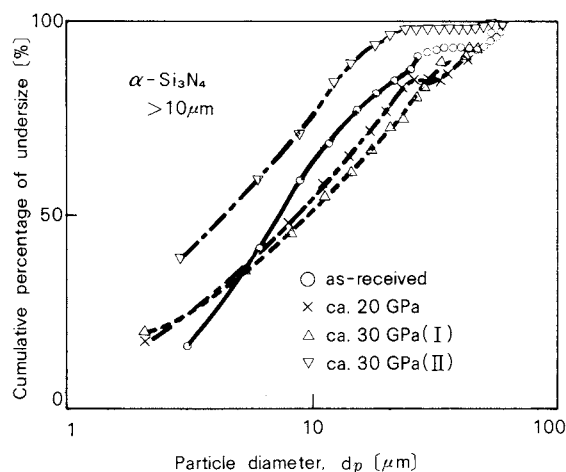


Fig. 13 Particle size distribution of as-received  $\text{Si}_3\text{N}_4$  and powder ground explosively shocked  $\text{Si}_3\text{N}_4$

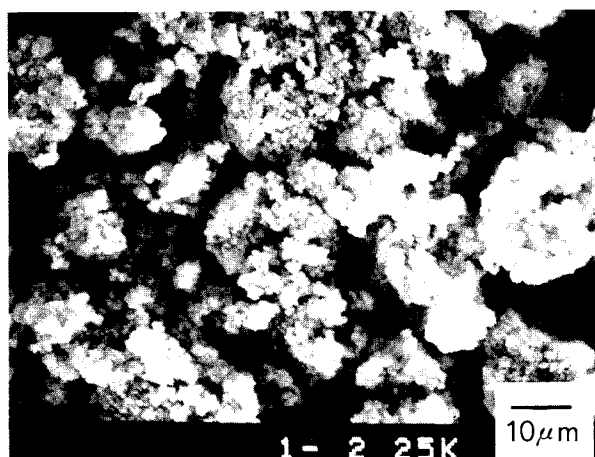


Fig. 14 Photograph of intact  $\text{Si}_3\text{N}_4$

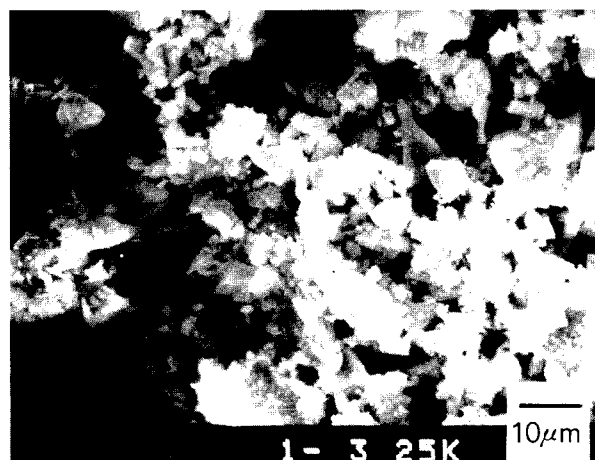


Fig. 15 Photograph of powder grinding explosively shocked  $\text{Si}_3\text{N}_4$

shown in Fig. 13, the particle size distributions of the shock-treated powder is wider. In Figs. 12 and 13, the mark  $\nabla$  indicates the tapping density and particle size distribution of shock-treated powder, the average particle size of which is smaller than the original sample. The tapping density is still higher than that of the original powder. SEM photographs of particles were taken to examine the shapes of the particles, and Figs. 14 and 15 show the photographs. Apparently, the shock-treated powder differs in shape from the as-received powder, being an aggregate of particles each of which is oval in shape and has edges, as often seen in various kinds of ground specimens. On the other hand, the as-received powder is a loose aggregate composed of particles which are finer in particle size, and the shock-treated powder forms a structure in which there are fewer pores between particles. The specimens were also tested with respect to water adsorption at the surface, and to the O/N ratio at the surface, etc., but there was little difference between the shock-treated powder and the as-received powder. Accordingly, the high packing density of the shocked powder is due to the wider particle size distribution, the shape of the particles, and the lower porosity of the aggregate.

#### 4. Conclusion

Silicon Nitride ( $\text{Si}_3\text{N}_4$ ) of both the  $\alpha$  and  $\beta$  types was explosively shock-treated by the one-dimensional method. The characteristics of the shocked compact etc. were analyzed. The following are the conclusions reached:

(1) Some of the shocked compacts showed a density of approx. 90% of the theoretical density.

(2) With respect to the influence of particle size distribution, provided that the initial packing fraction of the powder is constant, a powder with a larger average particle size produced a larger strain than a powder with a smaller average particle size, but the difference was slight.

(3) Vickers hardness, and residual strain, etc. indicated that the shock-treatment was more effective on the  $\alpha$  type.

(4) A strain of approx.  $10^{-3}$  was obtained, but it was not necessarily proportional to the shock pressure. The spin density was in the

order of  $10^{18}$ , and the spin density at 30 GPa was lower than that at 20 GPa.

(5) Only the peripheral portions of the shocked compact were contaminated with metal impurities.

(6) The solubility of  $\text{Si}_3\text{N}_4$  in NaOH and in HF solution indicated the presence of an active surface layer.

(7) The shock treatment increased the packing density of the powder.

### Acknowledgement

The authors want to express their gratitude to Dr. Kazuo Someno, Mr. Hiromichi Shimada and Mr. Shoji Kikuchi, all of National Chemical Laboratory for Industry, for their advice and co-operation in making the ESR, IMA and IR measurements, respectively.

### References

- 1) Sawaoka, A. and M. Araki: *Ceramics*, **10**, 297 (1975).
- 2) Ikazaki, F., K. Uchida, A. Goto, M. Kawamura and S. Fujiwara: *J. Soc. Powder Technol., Japan*, **20**, 615 (1983).
- 3) Ikazaki, F., K. Uchida, A. Goto, M. Kawamura and S. Fujiwara: *J. Soc. Powder Technol., Japan*, **20**, 717 (1983).
- 4) Graham, R. A., B. Morison, E. L. Ventrini, E. K. Beauchamp and W. F. Hammett: "Emergent Process Methods for High-technology Ceramics", (Ed. by R. F. Davis, et al.) Plenum Publishing Corporation, **17**, 719 (1984).
- 5) Beauchamp, E. K., R. E. Loehman, R. A. Graham, B. Morison and E. L. Venturi: *ibid*, **17**, 735 (1984).
- 6) Kanno, Y., Y. Kuwabara and S. Fujiwara: *Yogyo-Kyokaishi*, **92**, 617 (1984).
- 7) Kanno, Y.: *J. Soc. Powder Technol., Japan*, **21**, 697 (1984).
- 8) Widerley, S. E., J. W. Sprague and J. E. Campbell: *Analytical Chem.* **29**, 210 (1957).
- 9) Petrovic, J. J., B. W. Olinger and R. B. Roof: *J. Mat. Sci.*, **20**, 391 (1985).
- 10) Yokoyama, S., M. Hirose and Y. Osaka: *Japan. J. Appl. Phys.*, **20**, L 35 (1981).
- 11) Wannagt, U.: *Advances in Inorganic Chemistry and Radiochemistry*, **6**, 232 (1964).
- 12) Bergmann, O. R. and J. Barrington: *J. Am. Ceram. Soc.*, **49**, 502 (1966).

# The Visualization of Flow Patterns on a Sphere in a Packed Bed<sup>†</sup>

Yutaka Tsuji, Yoshinobu Morikawa,  
Masahiko Nakao and Naoyuki Nakatsukasa

Department of Mechanical Engineering for Industrial  
Machinery, Faculty of Engineering, Osaka University\*

## Abstract

*An experiment was made to visualize the surface flow pattern of spheres in a packed bed. Spheres, the surface of which were coated with benzoic acid, were set within a packed bed and exposed to water flow for a certain period of time. The flow patterns on the surface were observed by the patterns of dissolution of benzoic acid. The patterns were compared with the results of visualizations by other workers using a different method. It was found that the present results are in good agreement with those results in terms of the location of separation lines and singular points on the surface.*

## 1. Introduction

A packed bed is often used as an effective way of dust collection in a gas at high temperatures. When the basic mechanisms of dust capture are analysed in such a bed, the fluid motion within the bed should be taken into consideration. Also, in considering mass transfer in the packed bed, the flow around each particle is an important factor. However, there have been very few investigations of fluid motion within the bed, and a series of works by the Hanratty group (Jolls and Hanratty<sup>1)</sup>, Wegner et al.<sup>2)</sup>, Karabelas et al.<sup>3)</sup>) are the only ones which dealt with visualization of the flow around an individual particle in a bed. Since particles are in contact with each other in the bed, flow structure becomes very complicated even for spherical particles.

Wegner et al.<sup>2)</sup> made a test model of the packed bed consisting of transparent glass spheres. The fluid that they used in the experiment was a liquid which had the same refrac-

tive index as that of the glass. To visualize the flow, a small amount of dye was injected into the flow through a nozzle installed in the sphere. They related the flow pattern on the surface to the problem of singularity caused by three dimensional separation on the boundary layer. This kind of problem has been dealt with by Lighthill<sup>4)</sup>. Wegner et al.<sup>2)</sup> pointed out that the contact point between spheres becomes what is called the "saddle point" on the skin friction line. They also clarified the locations of the nodal and focal points.

The flow field in the present experiment was almost the same as that of Wegner et al.<sup>2)</sup>, but it was visualized in a way which was different from theirs. The method presented in this paper was based on the dissolution of solid chemicals in a liquid. That is, the sphere was coated with benzoic acid. The degree of dissolution of benzoic acid depends on the surface shear stress. As a result, the surface flow pattern was recorded in the form of streak lines. This method is easier to use than the dye injection method, particularly for a complicated flow field in a packed bed as in the present example.

In this paper, a technique of visualization using benzoic acid is described first, and then the results of the sphere in the packed bed are presented.

\* 2-1, Yamada-oka, Suita, Osaka, 565  
TEL. 06 (877) 5111

† This report was originally printed in *J. Soc. Powder Technology, Japan*, **22**, 599-605 (1985) in Japanese, before being translated into English with the permission of the editorial committee of the Soc. Powder Technology, Japan.

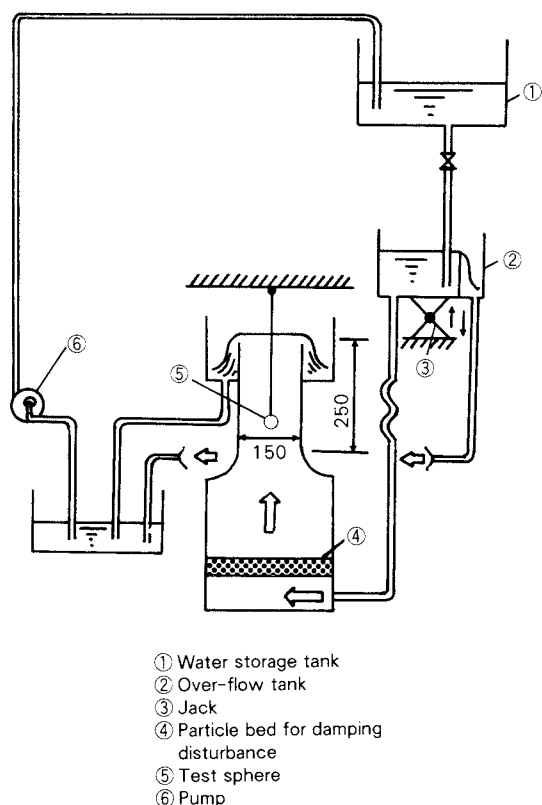


Fig. 1 Experimental equipment

## 2. Arrangement of the experiment

### 2. 1 Water tunnel

A water tunnel was specially designed, in which a uniform stream flowed vertically in the upward direction. The outline of the tunnel is shown in Fig. 1. The tunnel has a square test

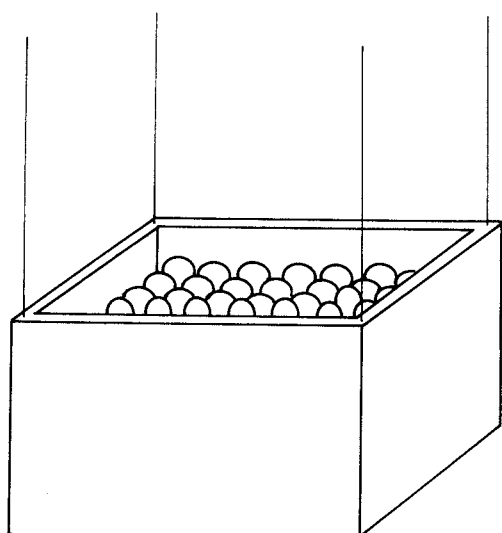


Fig. 2 Packed bed of particles

section of  $15 \times 15$  cm, and the length of the test section is 25 cm. Most parts of this tunnel are made of acrylic plates. The flow velocity can be adjusted arbitrarily by changing the height of the over-flow tank ②. Figure 1 shows a single sphere hung from a string in the test section. In the packed bed experiment, many steel balls are regularly packed in a wooden box, the bottom of which is made of a mesh screen. This box is hung from strings as shown in Fig. 2 and set up in the test section of the tunnel.

### 2. 2 Visualization technique

The present visualization technique was based on the phenomena of mass transfer from the surface of a body. As described above, the test sphere was coated with benzoic acid, and exposed to the flow for a certain period of time. The dissolution of benzoic acid is remarkable where the velocity gradient on the surface is steep. Therefore, the surface flow patterns could be observed at leisure after taking up and drying the test sphere.

The actual process of this kind of visualization is described next. The benzoic acid, which is a white powder at ordinary temperatures, was made molten by heating (its melting point is  $122.4^\circ\text{C}$ ). Three kinds of yet to be hardened steel bearing balls were used as the test spheres, the diameters of which were  $d = 10, 15$  and  $19.5$  mm. A metal string used as a support was attached to the sphere. First, the surface of the spheres was coloured white using spray lacquer, while benzoic acid was coloured differently from the sphere with ink. Coating with the benzoic acid was done by dipping the sphere in to the molten benzoic acid and taking it up quickly. The film of benzoic acid could be made thinner by pre-heating the sphere. In this experiment, the thickness of the film was about  $0.5$  mm. The metal string was cut and removed when the test sphere was set in the packed bed.

If the fluid velocity was high, the benzoic acid dissolved quickly even in pure water. However, the present velocity was so low that a means for promoting dissolution was necessary. Thus, methyl alcohol was added to the water at 40% in weight. The rate of dissolution was influenced by temperature, too. Therefore, a heater was set in the tank ① to keep the pipe-

line at a constant temperature by covering it with glass wool. When the temperature of the liquid was 23 to 26°C, about 10 to 15 minutes were needed for the flow patterns to be seen clearly on the spheres.

### 3. Results

#### 3. 1 Single sphere

The visualization method presented here was checked by using it for a certain well-known flow before it was applied to the packed bed. Such confirmation is particularly important at low fluid velocities. The fluid velocities in this work were adjusted to be so low that similarity in flow based on the Reynolds number could be obtained between the present packed bed and actual ones. That is, the particle size was 10 to 20 mm in the present flow, while it is much smaller in ordinary packed beds. The superficial fluid velocities were in the order of several cm/sec in this experiment. If the density of the coated material (benzoic acid) is different from that of the fluid, true flow patterns cannot be obtained at low velocities due to the effect of gravity. Therefore, a preliminary experiment was done in which the flow around a single sphere was visualized in a uniform stream by using the method presented here.

Figure 3 shows a photograph of the pattern

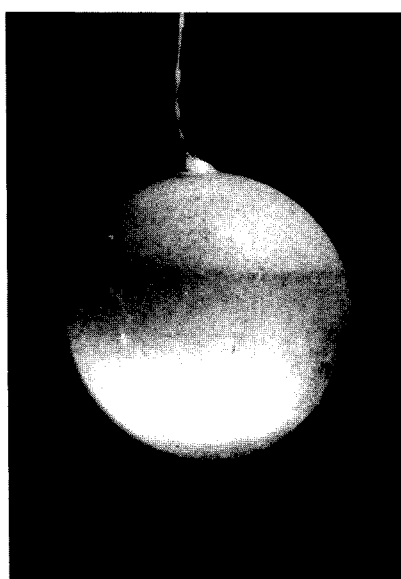


Fig. 3 Separation line on a single sphere

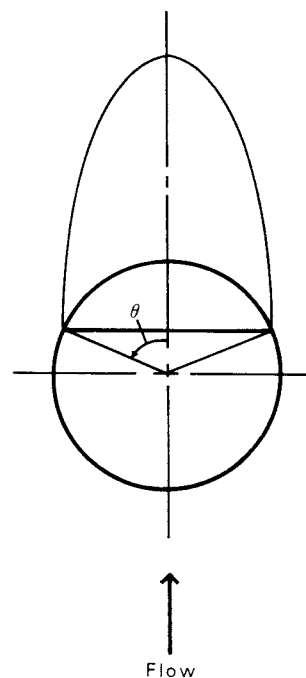


Fig. 4 Separation angle  $\theta$

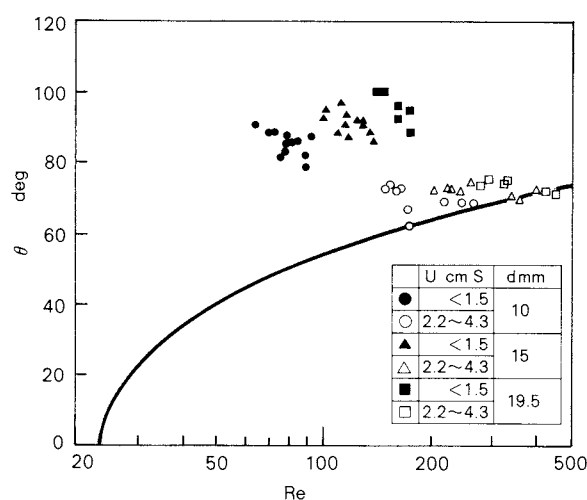


Fig. 5 Measured results of separation angle, —: Taneda<sup>5)</sup> 1956

on the sphere. The horizontal line observed on the sphere near the equator corresponds to the separation line of the flow. The measured results of the separation angle  $\theta$ , which is defined in Fig. 4, are shown in Fig. 5. The empirical curve given by Taneda<sup>5)</sup> is also presented in the figure for comparison. A group of white symbols nearly agrees with Taneda's curve, while the black symbols show a considerable disagreement. Experimental points of black



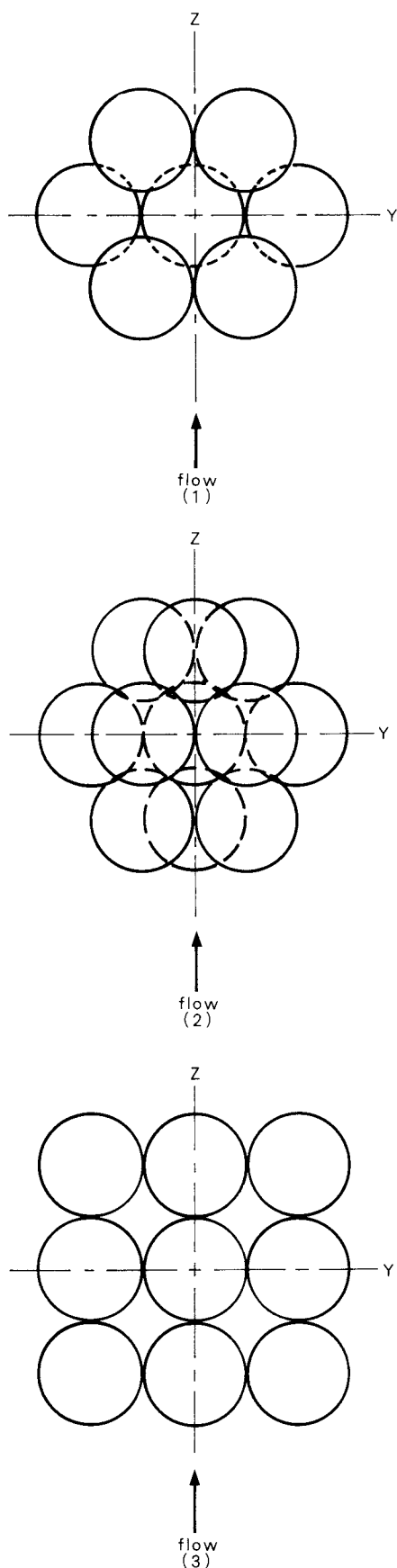


Fig. 6 Array of spheres in the packed bed

symbols were obtained at a velocity  $u$  less than 1.5 cm/s. The disagreement observed at low velocities came from the effect of gravity, as has been mentioned. The specific weight of benzoic acid is larger than 1 (1.2659 at 15°C). Therefore, when the flow approaches the sphere upwards at very low velocities, the dissolved material tends to fall down along the surface of the sphere, indicated by the large values of  $\theta$ . This phenomenon was observed by the naked eye as well. Based on the above result, visualization at velocities less than 2 cm/s was avoided in the present experiment.

### 3. 2 Packed bed

Generally, particles in an actual bed have a variety of sizes and shapes. Also, the geometrical position of particles with respect to each other is irregular. However, the present study dealt with only three cases where spheres of a constant diameter were packed regularly, as shown in Fig. 6. Cases (1) and (2) have the same packing structure, called tetrahedral or rhombohedral packing, but these are treated separately in this work because flow fields in them differ depending on the relative direction of the uniform flow to the bed. Case (3) is called cubic packing. The number of contacts of the sphere is 12 in cases (1) and (2), and it is 6 in case (3).

The present bed consisted of 4 or 5 layers, and the test sphere were set in the third layer from the front facing the uniform flow. The coordinate system used in this paper is shown in Fig. 7, where  $\Theta$ ,  $\Phi$  and  $R$  are the components of the spherical coordinate, and  $Z$  is the vertical axis with the downward direction which is

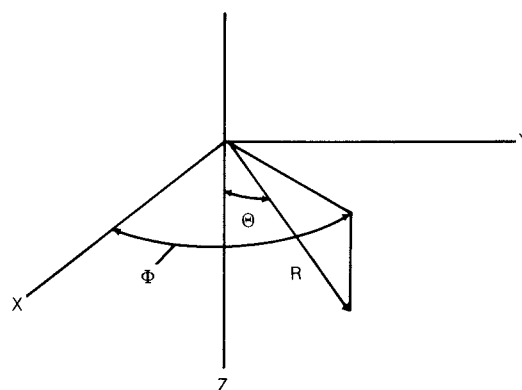


Fig. 7 Coordinate system

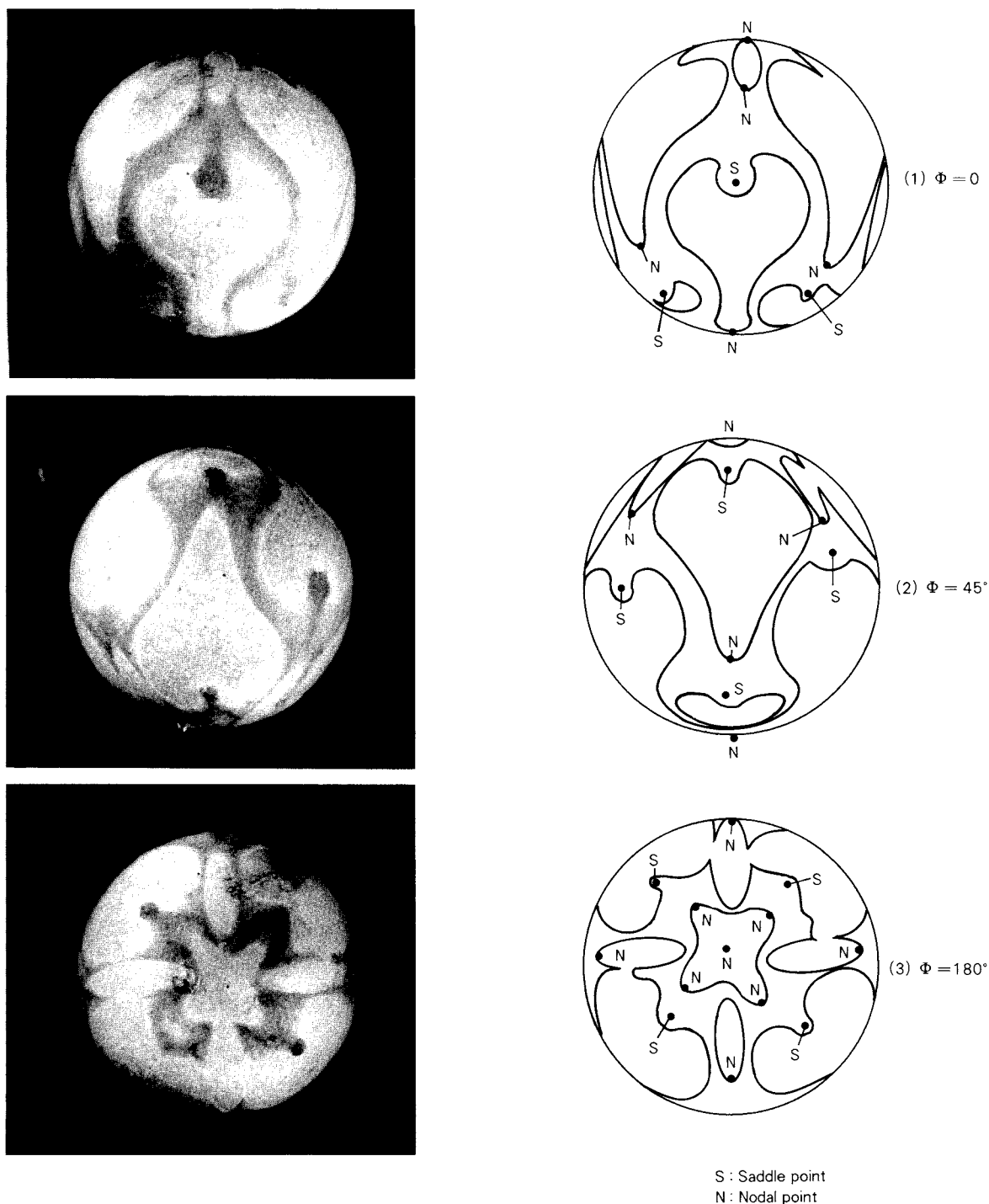


Fig. 8 Results of visualization in the case of Fig. 6 (1)

positive. The direction perpendicular to the paper is chosen as the X-axis.

Figure 8 shows the results of case (1). Wegner et al.<sup>2)</sup> also presented the results of this case. Figs. 8 (1) and (2) are side-views observed from the position  $\Phi = 0$  and  $45^\circ$ , while Fig. 8 (3) is a

picture seen from the top  $\Theta = 180^\circ$ . For convenience of explanation, a sketch is given for each photograph. The dark parts correspond to the places of much benzoic acid. It is found from these pictures that a characteristic flow field which is closely related to three-dimen-

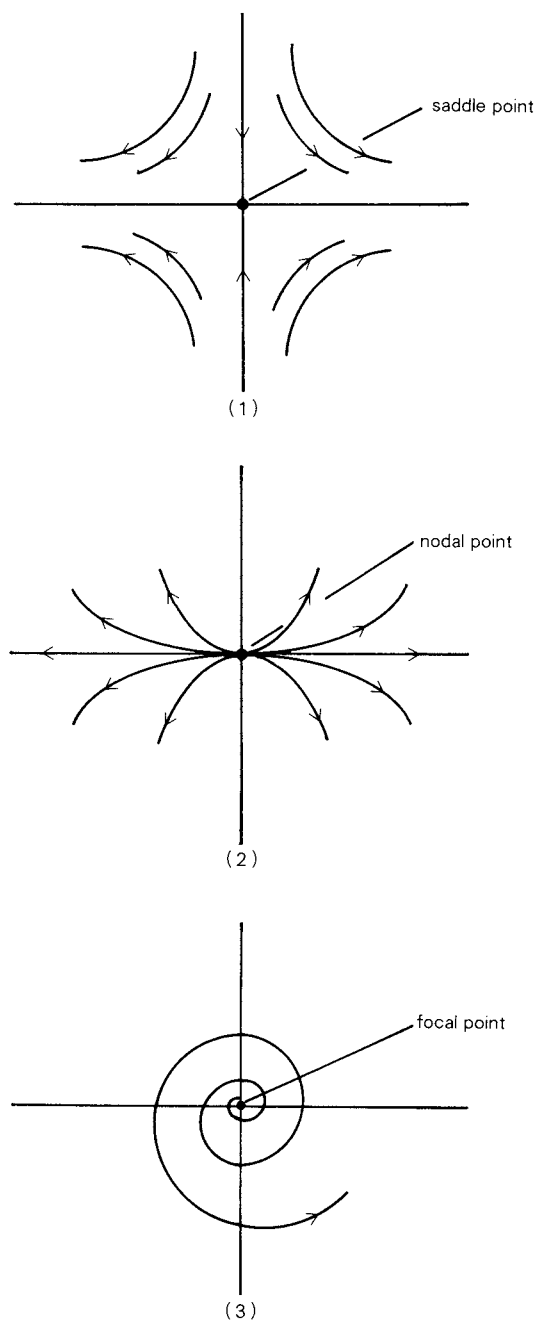


Fig. 9 Singular points of separation in three dimensional flow

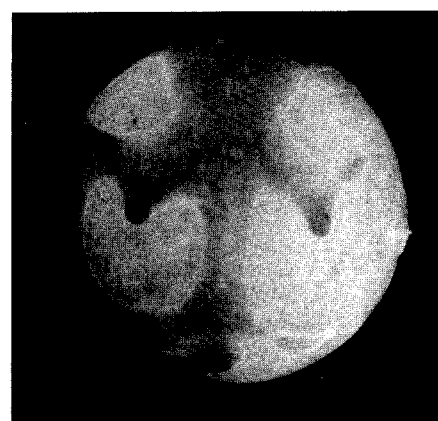
sional separation of the boundary layer is established in the bed.

Let us consider points and lines where the surface shear stress becomes zero. For a single sphere, the shear stress is zero at two apices and along the separation line, as shown in Figs. 3 and 4. The sphere in the packed bed has several points of zero shear stress besides the two apices. These are identified as singular points in the theory of three-dimensional separation.

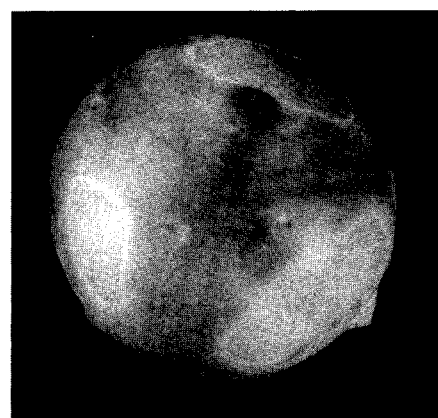
Such singular points are classified into some groups by analyzing the trajectories of a fluid particle on the limiting stream line. The sphere in the bed has the singular points shown in Fig. 9. This figure schematically presents the trajectories of the fluid particle near the singular points. Lighthill<sup>4)</sup> defined the line running from a saddle point to a nodal point as the line of separation of the three dimensional flows. The saddle, nodal and focal points



(1)  $\Phi = 0$



(2)  $\Phi = 45^\circ$



(3)  $\Phi = 180^\circ$

Fig. 10 Results of visualization in the case of Fig. 6(2)

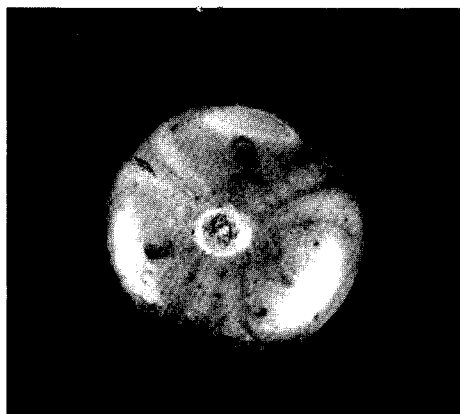


Fig. 11 Visualized result near the top of the sphere  
(The central part is a scar due to the string.)

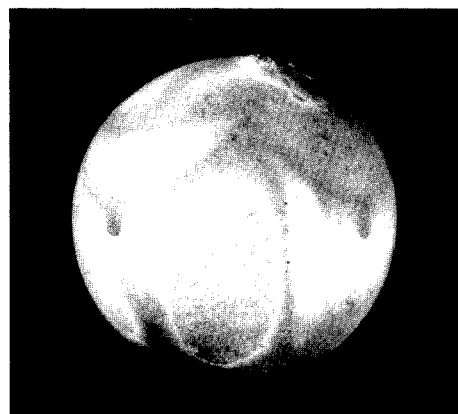


Fig. 12 Result of visualization in the case of Fig. 6(3)

indicated by Wegner et al.<sup>2)</sup> are shown in the sketches of Fig. 8. The present flow pattern is almost the same as Wegner's results except that the focal point cannot be observed in this work. What is noted here is that the benzoic acid remained in the form of curved streaks connecting separation zones. This means that the shear stress is so small along these streaks that a separation of the three dimensional boundary layer occurs there. The visualization for case (1) was made at a Reynolds number of from 210 to 380, in which the patterns obtained were the same as those in Fig. 8.

The results for case (2) in Fig. 6 are shown in Fig. 10. The patterns are quite different from those in Fig. 8. Neither the focal point nor the nodal point can be observed clearly in the pictures. Experiments on this packing were made at the Reynolds number  $R_e = 70 \sim 460$ , but the results were almost the same within this range. However, at a high Reynolds number, several streaks were observed near the apex, as shown in Fig. 11. It is not clear at this stage in the present work whether these streaks are characteristic of such high Reynolds numbers or of the sort of packing.

Figure 12 shows the results of cubic packing. A curve catenary-like is observed around the central part. A line similar to this was sketched by Karabelas et al.<sup>3)</sup>. Figure 12 shows that longitudinal streaks appear alternatively from the bottom to the central part. These streaks were not observed in Karabelas' experiment where the cubic bed consisted of only one layer.

#### Nomenclature

$d$	: diameter of sphere	[mm]
$R_e$	: Reynolds number $ud/\nu$	[—]
$u$	: fluid velocity	[cm/s]
$\theta$	: separation angle	[degree]
$\Theta, \Phi, R$	: spherical coordinates	[degree, degree, mm]

#### References

- 1) Jolls, K.R. and T.J. Hanratty: *Chem. Engng. Sci.* **21**, 1185 (1966).
- 2) Wegner, T.H., A.J. Karabelas and T.J. Hanratty: *Ibid.*, **26**, 59 (1971).
- 3) Karabelas, A.J., T.H. Wegner and T.J. Hanratty: *Ibid.*, **28**, 673 (1973).
- 4) Lighthill, M.J.: "Attachment and Separation in Three Dimensional Flow, in *Laminar Boundary Layers*", p. 72, Oxford Univ. Press, London (1963).
- 5) Taneda, S.: *J. Phy. Soc. Japan*, **11**, 1104 (1956).

**Hiroshi Komiyama**\*

*Department of Chemical Engineering  
University of Tokyo\**

**Hisatsugu Kaji**

*Kureha Chemical Industry Co., Ltd.\*\**

## 1. Introduction

Chemical Vapor Deposition (hereafter referred to as CVD) forms a thin film on a substrate by means of a thermo-chemical reaction. The growth rate of the film thickness depends on the conditions of the reaction. However, a rate of 10 microns per hour is the maximum value found in conventional CVD methods. Therefore, industrial applications of CVD methods are limited to production of thin films for the VLSI and to coating to improve the mechanical properties or corrosion resistance of some matrix materials, wherein films of just a few microns in thickness are produced. If the rate of the formation of thin films by CVD can be increased by 100 times, as described in this paper, it would enable not only the formation of CVD films in one-hundredth of the time of conventional processes but also the synthesis of a thin plate 1 mm in thickness. This is the first significant variable needed to increase the rate of the CVD method.

Consider the manufacturing processes of ceramics (broadly speaking) from a different viewpoint. There are two principal categories of technologies: one covers those for conventional ceramics based on the process of producing and sintering powders; the other relates to those for directly synthesizing ceramics from the gas phase, a typical one being the

CVD method. One feature of conventional ceramic production methods is high productivity, whereas CVD methods are easier to control. On the other hand, problems with conventional ceramics methods include poor controllability, while CVD methods also have low productivity. Because of the above reasons, silicon nitride, used as mechanical materials, is produced by conventional ceramic technology, and that used for VLSI is synthesized by CVD methods. Therefore, this field, requires sophisticated conventional ceramic technology as well as a high productivity CVD method. In the conventional ceramics industry, the synthesis of superior powders and an appropriate sintering process has been accomplished in order to achieve and integrate macroscopic properties (typically, shape and dimensions), while ensuring superior microscopic structure (typically, composition and grain boundary). These developments tend to improve the controllability of conventional ceramic technologies.

The CVD method, when speed up is realized, is superior to conventional ceramics technology in terms of the purity of the products it produces. The conventional ceramics process inevitably includes factors, such as the contamination of powder surfaces and additives used in the sintering process, which reduce purity. Also, the CVD process can produce materials having a high chemical bonding force, which is expected to become more and more important in the future. Sintering such materials is more difficult, and this fact can easily be understood when one considers the sintering of a diamond. The authors believe that both the CVD method and the ceramics technique should be developed in a supplementary manner, however, studies on the CVD method should be promoted more vigorously than is the current inclination in this field.

\* 7-3-1, Hongo, Bunkyo-ku, Tokyo, 113  
TEL. 03 (812) 2111

\*\* 1-9-11, Horidome-cho, Nihonbashi, Chuo-ku, Tokyo, 103  
TEL. 03 (662) 9611

† This report was originally printed in *Monthly Semiconductor World*, 8, 42-49 (1986) in Japanese, before being translated into English with the permission of the editorial committee of the Press Journal Co., Ltd., Japan.



## 2. Factors limiting the CVD rate

Since CVD is based on a chemical reaction, the temperature and concentration may be increased in order to speed up the reaction rate. The actual film growth rate, however, has a maximum value at a specific temperature and concentration, and in most cases, the rate decreases when the temperature and concentration are higher than the optimal values. A variety of mechanisms are thought to be the causes of this phenomenon; for instance, some radicals are produced to etch the growing film when halogenated materials (ex. silicon chloride) are used; This phenomenon may be caused by the dynamics of absorption observed in a gas-solid catalytic reaction. However, the essential cause, irrespective of the system used, is the competitive relationship between particle formation in the gas-phase and film growth.

In an ordinary CVD process, a substrate heated to a high temperature is placed in a reactive gas. The temperature of the fluid is lower than that of the substrate surface, or the temperature is set so as to rise in the direction of the substrate. If the temperature of the substrate is increased in order to speed up the reaction rate, the temperature of the fluid in the adjacent area also rises, thereby generating particles in the gas-phase. If particles should be formed, reactant molecules will deposit either onto the substrate surface or on the particle surface. Nucleation in the homogeneous phase is often discussed using a physico-chemical nucleation theory having a free energy barrier. In a chemical reaction system having an original system of high free energy, the above theory may not be applicable. It may be considered that the particles are produced by gas-phase polymerization<sup>1)</sup>. That is, it is not reasonable to consider an energy barrier in gas-phase nucleation. It may also be considered that increasing the concentration is advantageous for the nucleation and growth of particles in the gas-phase. Therefore, film growth on a substrate by means of the CVD process is a competitive reaction to generate particles that can be controlled based on a very delicate balance. Therefore, it can easily be understood that the process for increasing film growth rate while avoiding particle formation is inevitably accompanied by many difficulties.

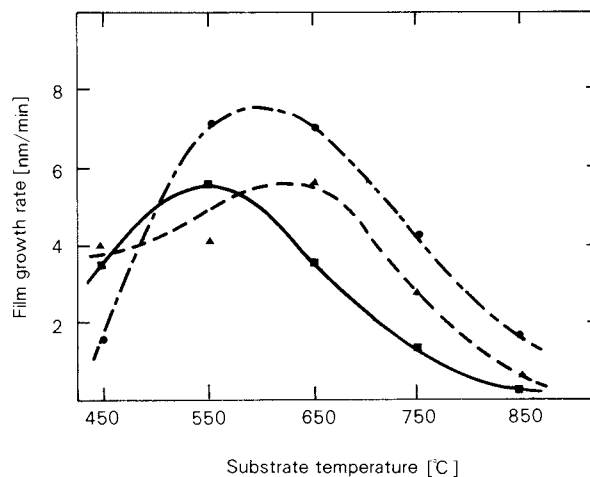


Fig. 1 The relationship between the film growth rate and substrate temperature<sup>12)</sup> (AlN, The film growth rate is reduced by increasing the substrate temperature so it is higher than a specific value.)

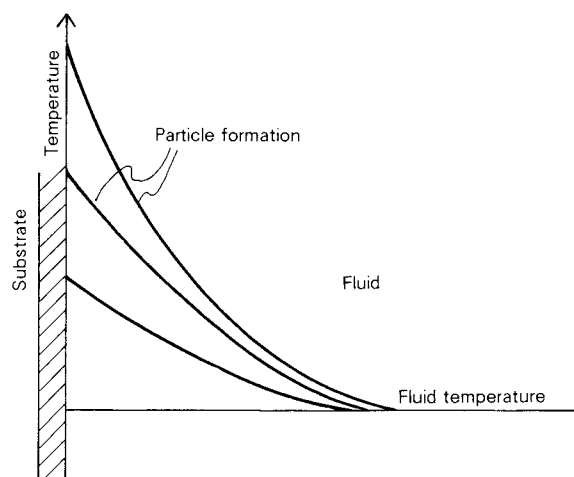


Fig. 2 The temperature distribution in an area adjacent to the substrate in an ordinary CVD process

## 3. Particle-precipitation aided CVD

If increasing the speed of the CVD process inevitably encounters the problem of particle formation in the gas-phase, one can formulate what kind of process can permit high speed film growth while allowing particle formation. If the CVD process is likened to falling frost, that is, a phenomenon wherein water molecules in a gas-phase directly precipitate onto the substrate, one might ask if it is possible to make snow fall? If yes, the fallen snow flakes should accumulate using themselves as nuclei in order

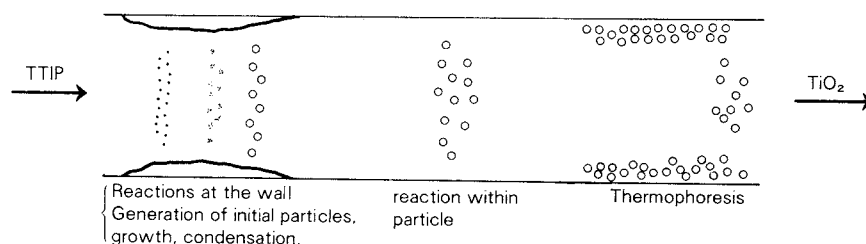


Fig. 3 A schematic drawing explaining the particle formation mechanism in tubular reaction equipment (for titania synthesis<sup>7)</sup>)

to produce a dense film because the density of the fallen snow is low. It is a well-known fact that particles can be synthesized in a gas-phase by means of the same reaction as in the CVD process. Particles formed at this time grow by colliding with each other or causing a surface reaction<sup>1)</sup>. That is, film growth may be realized by gathering the particles formed in the gas-phase onto the substrate and by providing an atmosphere in which the particles can grow.

### 3. 1 Importance of thermophoresis

The substrate faces upward in order to gather the particles formed in the gas-phase. One may wonder if this is effective. Gravity and inertia only slightly effect ultra-fine particles. The sedimentation speed of ultra-fine particles is very slow and negligible. Excluding static electric force and magnetic force, the sole force effectively working on particles smaller than 0.1 micron is the energy of motion caused by colliding molecules. Thermophoresis and diffusion based on Brownian motion are effective. Thermophoresis means a directional Brownian motion, wherein particles in a temperature gradient receive net forces that are the difference between the energy of motion received from the molecules colliding at the higher temperature and that received from the molecules on the lower temperature side, and migrate in the direction from the higher temperature area to the lower. The velocity of thermophoresis is given by the following:

$$V = \frac{3}{4(1 + \pi\alpha/8)} \frac{\mu}{\delta T} \frac{dT}{dX} \quad (1)$$

The velocity depends on the temperature gradient, viscosity ( $\mu$ ), and density ( $\delta$ ). A par-

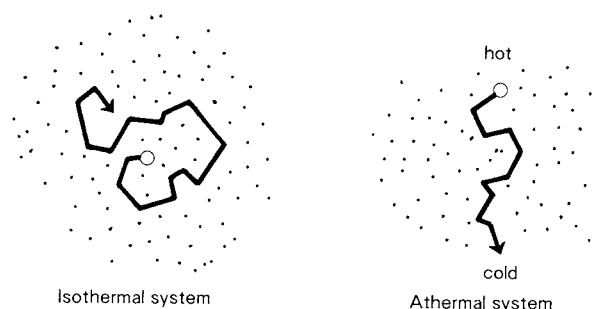


Fig. 4 Brown movements of ultra-fine particles in an isothermal system and in an athermal system

ticle velocity of several mm/s can easily be obtained at atmospheric pressure, and a velocity of several cm/s can be obtained under reduced pressure because the velocity is inversely proportional to the pressure. The value is large enough to accumulate particles formed in the area adjacent to the substrate.

Diffusion is also important, and a significant diffusion speed can be obtained, especially when the particle size is 100Å or smaller, thus exceeding the thermophoresis speed in some cases depending on the conditions. The diffusion coefficient decreases with the increase in particle size. However, the velocity of the thermophoresis does not depend on the particle size if the particle is smaller than the mean free path of the gas. Therefore, thermophoresis is important in order to gather ultra-fine particles onto the substrate.

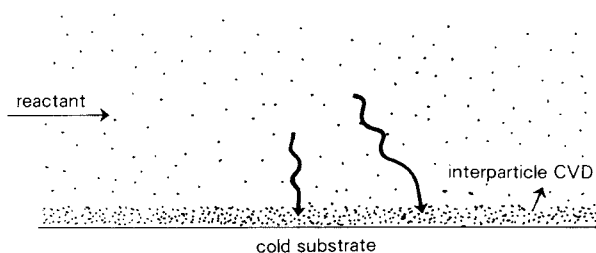
### 3. 2 The concept of particle-precipitation aided CVD<sup>2)</sup>

Three important factors of particle-precipitation aided CVD are as follows:

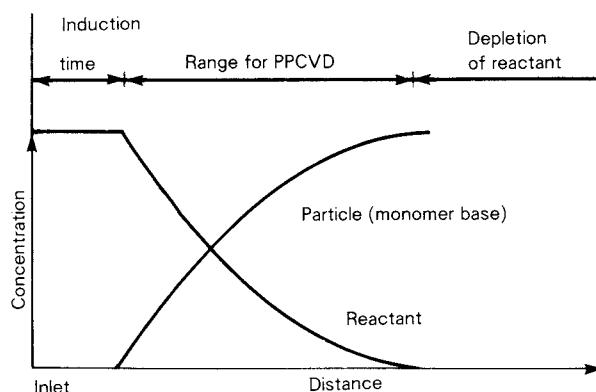
- (1) To generate ultra-fine particles by maintaining the gas-phase temperature and con-

- centration at high levels.
- (2) To accumulate particles onto the substrate with thermophoresis and in some cases, due to the dual effect of thermophoresis and diffusion by maintaining the temperature of the substrate at a point lower than that of the gas-phase.
  - (3) To maintain the temperature of the substrate at a point sufficiently high to accelerate the CVD reaction, and to position the substrate in the area where the raw material gas sufficiently exists.

**Figure 5**, a conceptual drawing, illustrates particle-precipitation aided CVD, and **Fig. 6** shows the spatial area used in this method. Qualitatively consider the conditions needed to synthesize a dense film using this method. First, the growing rate of film in the thickness, or the piling rate of particles, may be thought of as proportional to the temperature gradient, that is the difference between the temperatures of the gas-phase and the substrate, according to Eq. (1). On the other hand, the rate to make



**Fig. 5** A schematic drawing showing the concept of particle-precipitation aided CVD



**Fig. 6** A schematic drawing showing the concept of particle-precipitation aided CVD . . . . Conditions for the coexistence of particles and the raw gas-phase

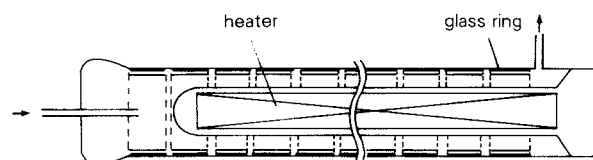
the particle layer dense is governed by the reaction rate at the surfaces of the deposited particles, and therefore it is believed that the higher the temperature of the substrate, the more dense the film becomes. One guideline for speeding-up this CVD process is to note that the higher the temperature of the substrate, the more advantageous it is to make the film more dense. Also, the larger the difference between the temperatures of the substrate and the gas-phase, the higher the growing rate of the film.

Viewing this process from another angle, though the growth surface of the film in the ordinal CVD process is a two-dimensional plane, this process can make the surface three dimensional by creating a particle layer.

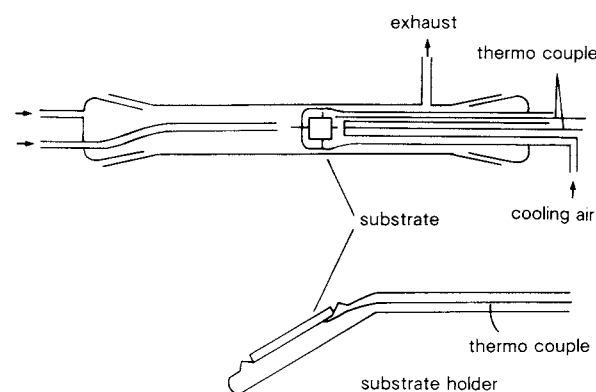
#### 4. Application to rapidly forming an AlN or TiO<sub>2</sub> film

##### 4. 1 The CVD apparatus

Various types of reaction apparatus are conceivable. However, the two experimental types shown in **Fig. 7** were used. One is a coaxial cylinder type having a heater inside the inner tube. Substrate rings are inserted so that they touch the external tube, and the temperature



(a) Coaxial cylinder type



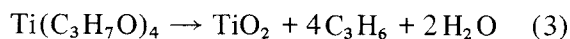
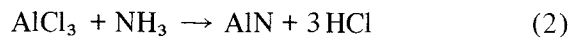
(b) External heater type

**Fig. 7** The experimental CVD apparatus for particle-precipitation aided CVD

of the external tube is controlled so that the temperature of the substrates is maintained at a proper value. Thus, a temperature gradient is generated in the radial direction of the coaxial cylinder from the center of the substrate. In this way, ultra-fine particles formed in the gas-phase flowing between the internal and external cylinders deposit onto substrates by thermophoresis (**Fig. 7 (a)**). In the other apparatus, reactive gas is heated by an external heater, and the substrates are cooled by air flowing through the substrate holder (**Fig. 7 (b)**). The CVD apparatus shown in **Fig. 7 (a)** has a concentration distribution of the raw material gas and particles as shown in **Fig. 6**. Therefore, in the apparatus there is a possibility that an ideal condition can be realized at one of the many equipped rings. It is a desirable apparatus for roughly determining the reaction conditions of a new reaction system in this new CVD process, which has many controlling variables, such as the temperature of the gas-phase and substrate, concentration in the raw gas-phase, and the position of the substrate. On the other hand, the apparatus shown in **Fig. 7 (b)** is suitable for obtaining a homogeneous film by a reaction system the process conditions of which have already been determined to a some extent.

#### 4. 2 Experimental confirmation of the concept<sup>3),4)</sup>

Experiments for synthesizing AlN or TiO<sub>2</sub> film according to the following reactions are described next.



AlN and TiO<sub>2</sub> films were synthesized using the CVD apparatus shown in **Fig. 7 (a)** and **(b)**, respectively. **Figure 8** shows SEM photographs which suggest that thermophoresis aided CVD is achieved based on the above mentioned concept. Both photographs illustrate the cross sections of the formed films at a right angle to the substrates. As shown in **Fig. 8 (a)**, a layer of AlN particles of several hundreds Å formed in the gas-phase and just deposited by the thermophoresis effect is observed on the side in contact with gas flow during the synthesizing process. The particle sizes gradually increase in the direction of the substrate, and a completely densified layer is observed in the area adjacent to the substrate. The growth mechanism of the film thus constructed is theorized as follows: Our calculated results revealed that molecules of AlCl<sub>3</sub> or NH<sub>3</sub> can diffuse at a sufficient rate in the deposit layer on the substrate and

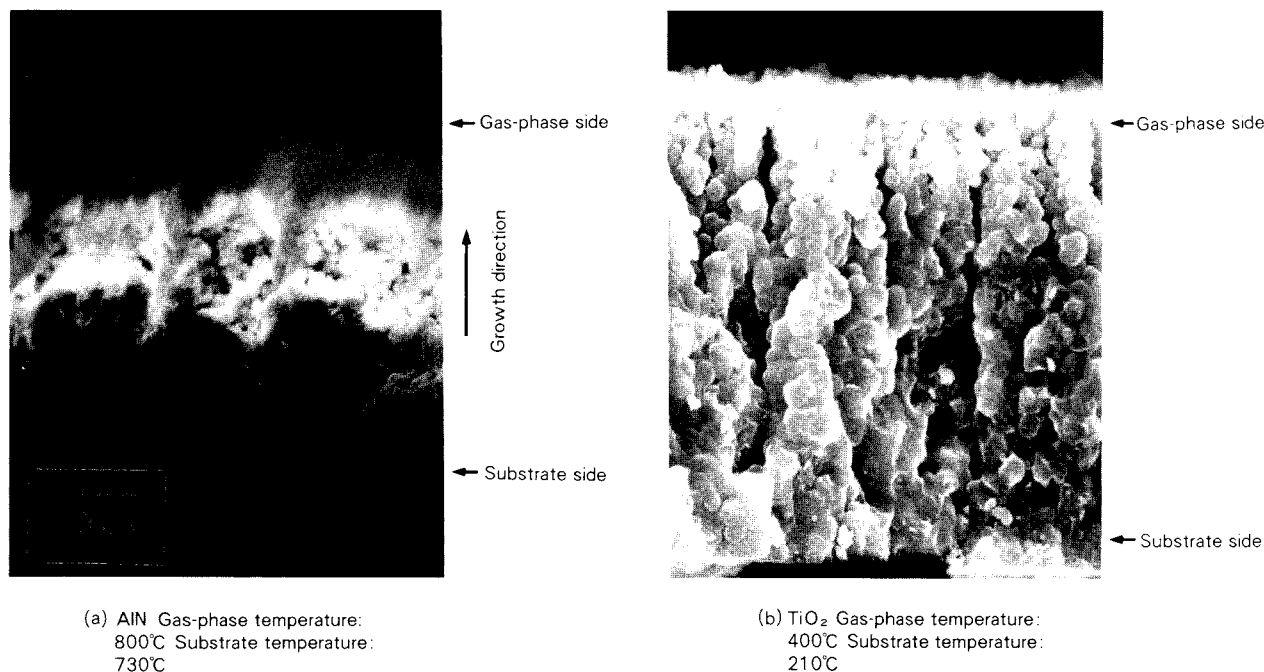
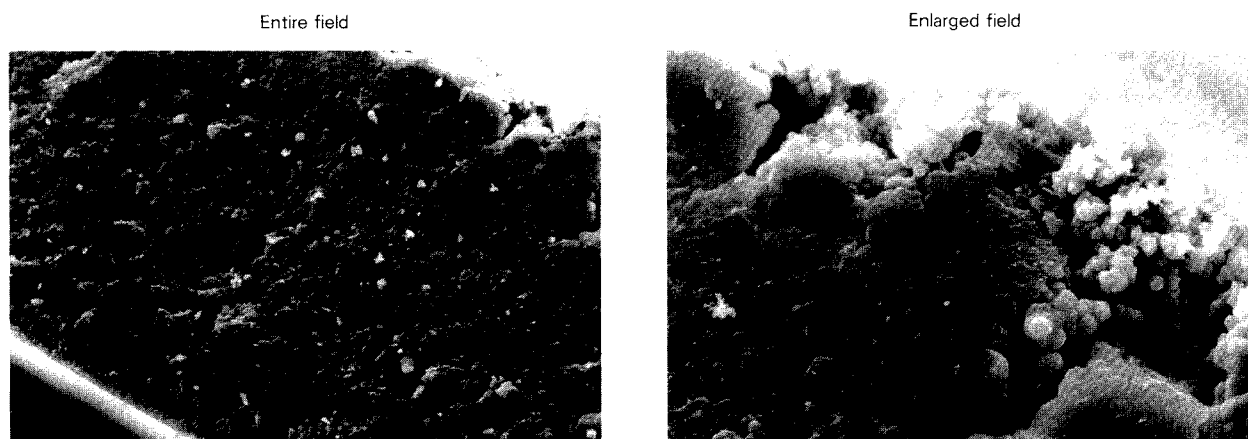
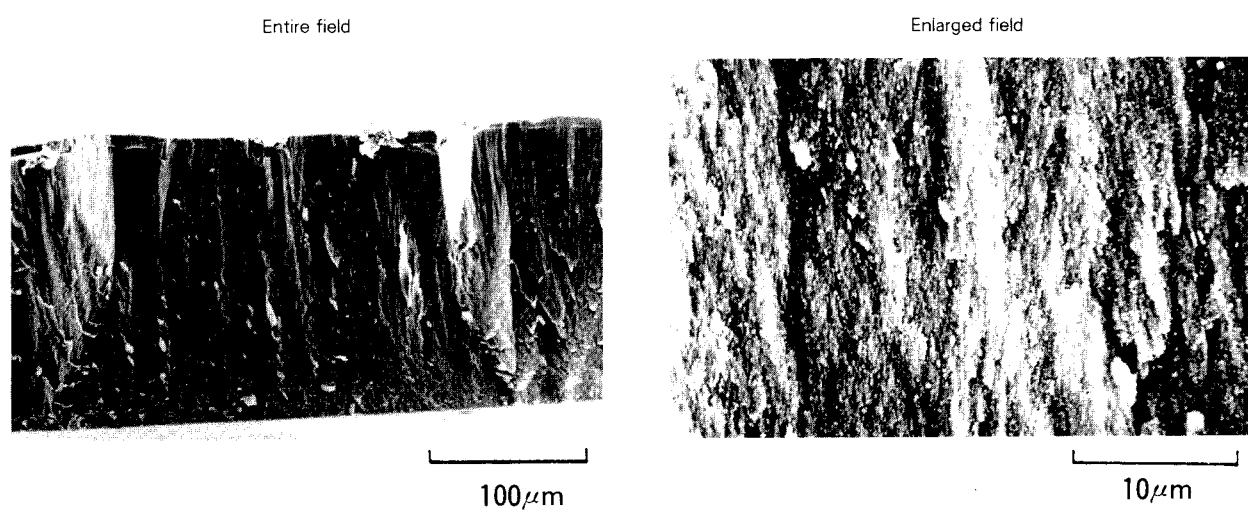


Fig. 8 Experimental confirmation of particle-precipitation aided CVD

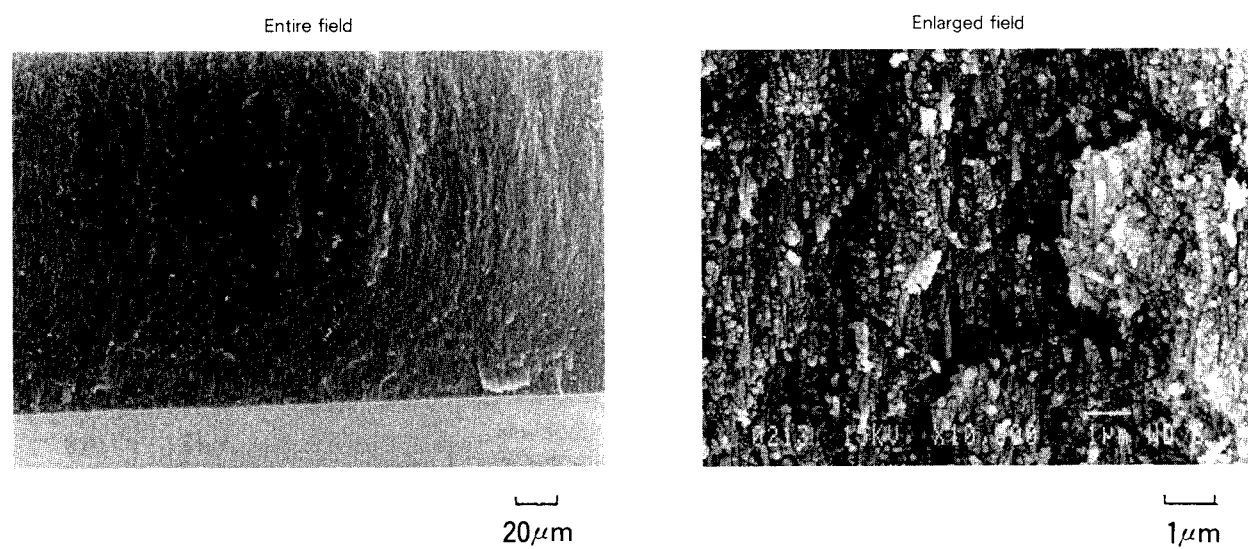




(a) Gas-phase temperature: 750°C Substrate temperature: 725°C



(b) Gas-phase temperature: 800°C Substrate temperature: 786°C



(c) Gas-phase temperature: 900°C Substrate temperature: 888°C

Fig. 9 Examples of dense synthesized AlN films



reach the area adjacent to the substrate. Therefore, the particles deposited onto the substrate at the earliest stage of the CVD process were exposed to the reaction atmosphere for the longest period and grew sufficiently to fill the cavities between the particles, thereby increasing the density of the layer. The intermediate layer consisting of particles with a large diameter are shown during the process of growth to become a dense layer. The above observation was for AlN film formation. However, a qualitatively similar structure was obtained when forming a TiO<sub>2</sub> film, as shown in Fig. 8(b). The TiO<sub>2</sub> film was formed by the same mechanism. The point that should be emphasized in this observation is that the TiO<sub>2</sub> film was obtained by the CVD apparatus shown in Fig. 7(a), wherein the amount of deposition on the wall of the inner cylinder was significantly smaller than the film obtained on the substrate. That is, when the reactive gas flow between the two surfaces of high and low temperature, an overwhelming amount of ceramics were formed on the lower temperature surface. Although it

appears inconsistent, this phenomenon can clearly be understood by following the above explanation. The total surface area on the lower temperature side is significantly increased by the deposition of ultra-fine particles formed in the gas-phase on the lower temperature wall. As a result, the effect of the surface area overcomes the effect of the temperature.

In these two experiments, the densification rate of the particle layer is slower than the growth rate. To obtain a densified film, it is supposed that the temperature of the substrate was too low or the temperature difference between the substrate and gas-phase was too large. However, the results of these experiments reveal that the concept of particle-deposition aided CVD can be achieved by choosing more appropriate conditions.

#### 4. 3 The synthesis of dense film (thin plate)

Figure 9 is SEM photographs showing the cross sections of AlN films synthesized by setting the temperature difference between the gas-phase and substrates at approximately 20°C, and by setting the temperature of the gas-phase at 750°C, 800°C, and 900°C, respectively. Figure 10 shows the XRD spectrum of AlN powder and the films produced above. These photographs reveal that the densification of AlN steadily proceeded especially in films synthesized at 800°C and 900°C. These extremely pure films are colorless, and transparent, semi-transparent or white. Table 1 lists the film growth rates using particle-precipitation aided CVD, while the same rates by a conventional CVD are listed in Table 2. The film growth rate achieved by using particle-precipitation-aided CVD was approximately 100 times higher than that of conventional CVD. A thin plate of 0.4 mm could be pro-

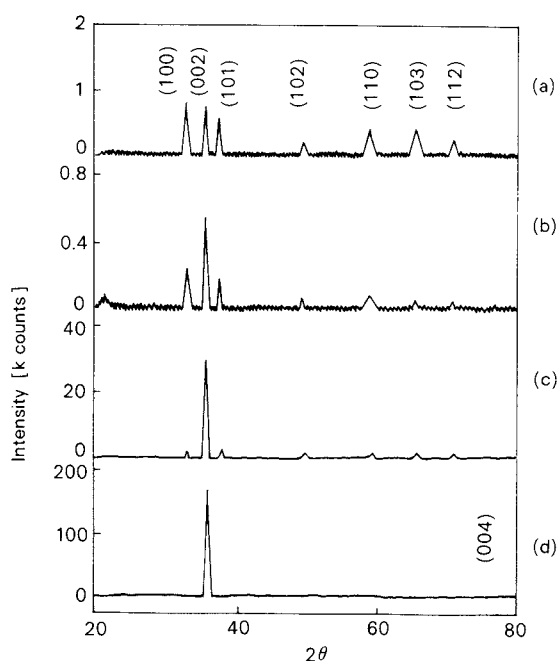


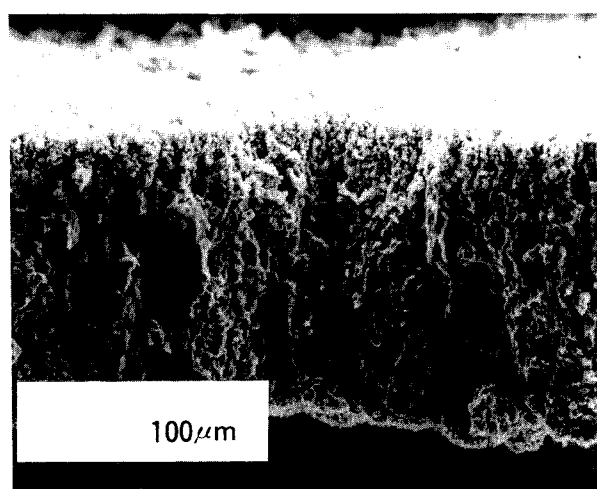
Fig. 10 An XRD spectrum of an AlN thin plate (a) powder, (b), (c) and (d) correspond to films shown in Figs. (a), (b), and (c), respectively.

Table 1 Synthesizing conditions for the AlN and film growth rates

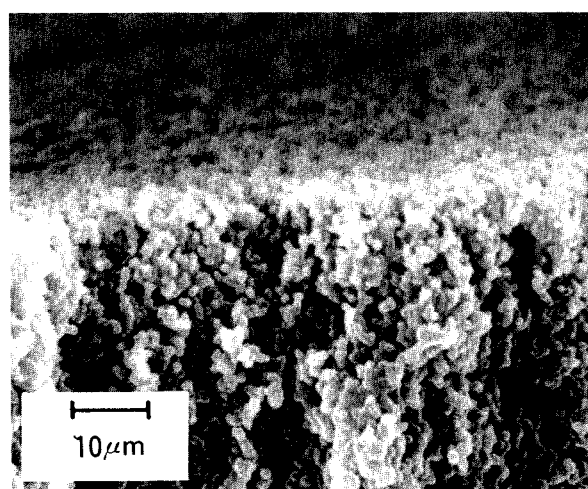
Symbols in Fig. 9	Gas-phase temperature [°C]	Substrate temperature [°C]	Film growth rate [mm/h]
(a)	750	725	0.22
(b)	800	786	0.36
(c)	900	888	0.30

Table 2 Film growth rate by references

Material	Temperature [K]	Film growth rate [mm/h]	References
$\text{NH}_3, \text{AlCl}_3$	1173 ~ 1623	$4 \sim 12 \times 10^{-3}$	8)
$\text{NH}_3, \text{AlCl}_3$	973 ~ 1573	$0.6 \sim 60 \times 10^{-3}$	9)
$\text{NH}_3, \text{AlCl}_3$	1273 ~ 1373	$12 \sim 15 \times 10^{-3}$	10)
$\text{AlCl}_3 \cdot 3\text{NH}_3$	1073 ~ 1473	$0.54 \sim 1.0 \times 10^{-3}$	11)
$\text{NH}_3, \text{AlBr}_3$	673 ~ 1173	$2.0 \times 10^{-3}$	12)



(a) Thin plate gas-phase temperature: 350°C  
Substrate temperature: 269°C



(b) Porous film Gas-phase temperature: 350°C  
Substrate temperature: 189°C

Fig. 11  $\text{TiO}_2$  thin film and porous film synthesized using raw materials of  $\text{Ti}(\text{C}_3\text{H}_7\text{O})_4$

duced every hour.

Surprisingly, the orientation of crystals which is observed in a film produced by usual epitaxial growth was found in the films synthesized by the above CVD process, as shown in the XRD spectrum. This orientation corresponds to the columnar structure in the growth direction as clearly shown in the fine structure observed by SEM. Only the mechanism, wherein the particles deposit and the cavities between each are filled, cannot explain the observed orientation of the crystals. It is now thought that the sizes of depositing particles are very fine, perhaps most of them are  $50\text{\AA}$  or smaller, and amorphous or the crystallinity is very low. While these particles or clusters crystallize on the substrate, an orientation is generated. These are our assumptions, and their experimental confirmation will follow.

Figure 11 shows SEM photographs of  $\text{TiO}_2$  dense and porous films. These are both amorphous, and most of them include micropores smaller than  $20\text{\AA}$ . These were obtained at a synthesis temperature lower than the crystallization temperature ( $380^\circ\text{C}$ ) of amorphous  $\text{TiO}_2$ . A temperature higher than this point produces a film with an Anatase structure similar to the oriented film of  $\text{AlN}^{(6)}$ . Films or thin plates having a basically similar structure were rapidly synthesized by two systems having different reaction conditions and a different reaction apparatus. This fact suggests that the thermophoresis-aided CVD process possesses the possibility of becoming a technology widely applied to various fields. Moreover, this CVD process permits the production of a porous film, which itself could be an important sensor or separation film.

## 5. Conclusion

This paper introduced the concept and experimental results for increasing the speed of the CVD process, applied to ceramics, such as aluminum nitride and titania. Other processes for increasing the speed of CVD are introduced in the references<sup>13)</sup>. Synthesizing ceramics by means of conventional ceramic processes have been actively developed. Thus, various breakthroughs may be expected. On the other hand, the CVD process has the attractive advantage of being essentially free from contamination or additives. In addition, the materials for the application of this process come from a very wide ranges, of from ceramics to metals or organic compounds, and material selection allows the process a wide range of reaction conditions. However, many problems must be solved in order to make the method for increasing the speed of CVD a more important subject in the field of material science. The important points from the engineering standpoint are as follows: The degree to which the process control of the microstructure and thus the quality of the film can be achieved, and the range within which the process can cover film shape, such as thickness and area. To appropriately respond to these points, first, the mechanism for creating film should be studied in greater detail. Second, the spatial and temporal distributions of temperature, concentrations of raw materials, cluster, or particles, and the flow rate of gas in the gas-phase and the surface of substrates should be investigated to reveal the relationship between the distributions of these factors and the distribution of the thickness and quality of films. In other words, the chemical engineering approach is especially important. We expect that the CVD process, which is a mass production means having superior microstructure controllability, will be more intensively developed.

## References

- 1) Komiyama, H.: KAGAKUSOSETSU No.48 "Ultra-fine Particles . . . Science and Application".
- 2) Komiyama, H.: Preprint of the 19th Autumn Meeting of the Soc. of Chem. Engrs., Japan, SA309 (1985).
- 3) Komiyama, H. and T. Osawa: "Rapid Growth of AlN Films by Particle-Precipitation-Aided Chemical Vapor Deposition", *Jpn. J. Appl. Phys.*, **24**, pp. 795-797 (1985).
- 4) Shimogaki Y. and H. Komiyama: "Preparation of TiO<sub>2</sub> Films by Thermophoresis-Aided Chemical Vapor Deposition", *Chem. Lett.*, pp. 267-268 (1986).
- 5) Komiyama, H., T. Osawa, H. Kaji and T. Konno: "Rapid Growth of AlN Films by Particle-Precipitation-Aided Chemical Vapor Deposition", 6<sup>th</sup> International Conference on High Tech Ceramics, Milan, Italy, p. 23-28, June (1986).
- 6) Shimogaki, Y. and H. Komiyama: *Yogyo Kyokai-shi (J. of Ceramics Soc., Japan)* **95**, pp. 70-75 (1987).
- 7) Kirkbir, F. and H. Komiyama: *Can. J. Chem. Engng* (in press).
- 8) Noreika, A. J. and D. W. Ing: "Growth Characteristics of AlN Films Pyrolytically Deposited on Si", *J. Appl. Phys.*, **39**, pp. 5558-5581 (1968).
- 9) Bauer, J., L. Biste and D. Bolze: "Optical Properties of AlN Prepare by Chemical and Plasmachemical Vapor Deposition" *Phys. Status Solid a*, **39**, pp. 173-181 (1977).
- 10) Yim, W. M., E. J. Stofko, P. J. Zanzucchi, J. I. Pankove, M. E. Henberg and S. L. Gilbert: "Epitaxially Grown AlN and Its Optical Band Gap" *J. Appl. Phys.*, **44**, pp. 292-296 (1973).
- 11) Chu, T. I. and R. W. Kelm, Jr.: "The Preparation and Properties of Aluminum Nitride Films" *J. Electrochem. Soc.*, **122**, pp. 995-1000 (1975).
- 12) Pauleau, Y., A. Bouteville, J. J. Hantzpergue, J. C. Remy and A. Cachard: "Composition, Kinetics, and Mechanism of Chemically Vapor-Deposited AlN Films" *J. Electrochem. Soc.*, **129**, pp. 1045-1052 (1982).
- 13) Hirai, T., K. Niihara and S. Hayashi: *Ceramics* **13**, pp. 861-867 (1978).

## Review

## The Angmill Mechanofusion System and its Applications

Tohei Yokoyama, Kiyoshi Urayama,  
Makio Naito and Masashi Kato

*Micromeritics Laboratory  
Hosokawa Micron Corp.\**

Toyokazu Yokoyama

*Department of Chemical Engineering  
Nagoya University\*\**

## 1. Introduction

In recent years, research on and the development of new-generation industrial materials have been done actively in various kinds of industries, including fine ceramics. It is well-known that most of the raw materials of new-generation materials are handled in a powdery form because the particulate state of the solid is the most suitable one for the development of new-generation materials.

The most characteristic aspect of the powder is the size of the component particles. Today, a growing interest is being taken in ultrafine particles on the order of an angstrom, as well as in submicron size particles.

On the other hand, the creation of new-generation materials by combining different powder materials has been of great importance as indicated by the successful development of various composite materials and functional devices.

The authors, who have been studying this subject for many years, developed an ultrafine "Angmill" grinding system making the best use of the most effective mechanism for fine grinding (1983)<sup>1)</sup>. Furthermore, the authors discovered that the Angmill system is also useful in powder treatment techniques. They introduced some of its applications in August 1986<sup>2)</sup>.

Lately, they have succeeded in developing a "Mechanofusion system" resulting from research on the application of the high-powered mechanical energy of the Angmill system to powder treatment.

"Mechanofusion" treatment is defined as the technique of creating particulate materials with new physical properties by mechanochemical<sup>3)</sup> surface fusion as a result of the strong mechanical force acting on the surface of different kinds of particles. Some typical examples from the numerous possible combinations of the materials handled by this system and the consequent change in powder properties will be discussed in this report.

## 2. The Angmill principle

The Angmill system was originally developed as an ultrafine grinding system with a simple structure based on attrition under strong compression. Prior to discussing the mechanofusion effect, its grinding mechanism will be briefly explained.

The main grinding chamber of the Angmill system rotates at a high speed. At the center of the mill, the inner pieces are fixed with a certain clearance against the inside wall of the chamber. The head of the inner pieces have

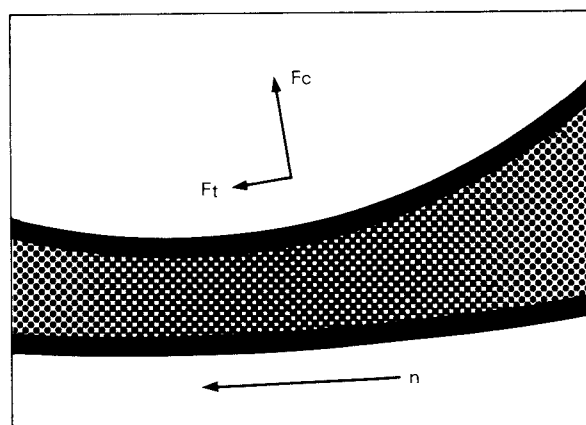


Fig. 1 The principle of the Angmill

\* No.9, Shoudai Tajika 1-chome, Hirakata, Osaka, 573

\*\* Furo-cho, Chikusa-ku, Nagoya, Aichi, 464

Received September 7, 1987

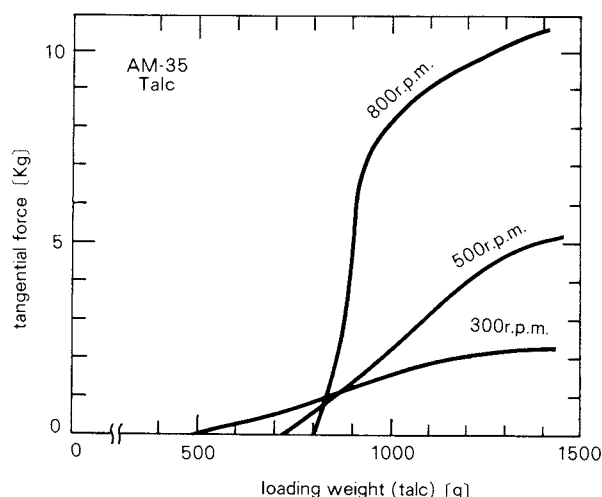


Fig. 2 Variation in the tangential force acting on the inner piece tip with loading weight

a smaller radius of curvature than that of the chamber. The material compacted by centrifugal force onto the inside wall of the chamber is compressed into the clearance and receives complicated forces in various states, such as compression, attrition, shearing and rolling (Fig. 1).

Figure 2 shows the variation in the tangential force acting on the tip of the inner piece with the loading weight at various rotation speeds. The result was obtained using a smaller type of mill having a chamber diameter of 350 mm and a talc powder with an average size of 44 microns as the feed to be ground. As seen from the figure, the point of increase of the tangential force on the inner piece depends upon the rotation speed.

Figure 3 shows the bulk density of the talc powder in the rotating chamber, which was calculated from the loading weight at the high point in Fig. 2 and the annular volume between the inner piece tip and the inside wall of the rotating chamber. It is understood that at 800 r.p.m. the talc powder has a higher bulk density than the packed bulk density obtained by a tapping of  $1.4 \text{ g/cm}^3$ . The ground product has an average size of  $0.5 \mu\text{m}$ .

On the other hand, the loading weight at the high point did not depend upon the rotation speed in polystyrene beads having an average size of about  $450 \mu\text{m}$ . Besides, the apparent volume of the material was almost the same as the above-mentioned annular clearance volume in the rotating chamber.

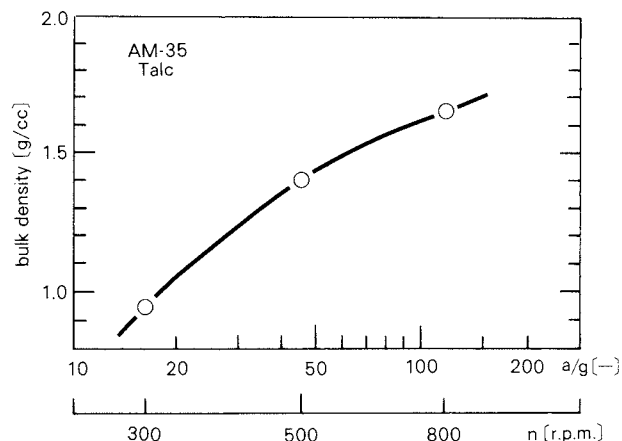


Fig. 3 The bulk density of the material under a centrifugal force

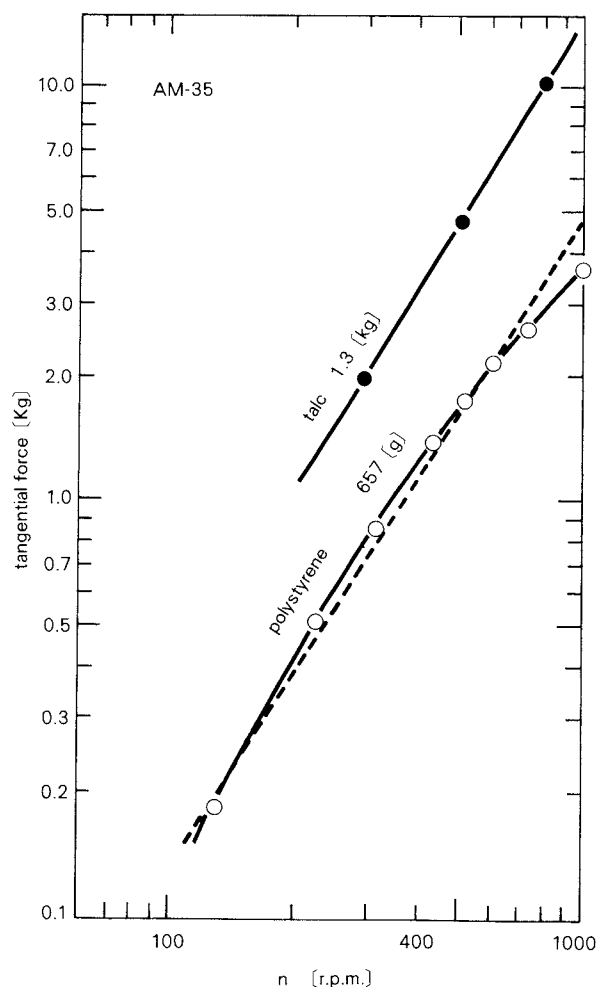


Fig. 4 Variation with rotation speed in the tangential force acting on the inner piece tip



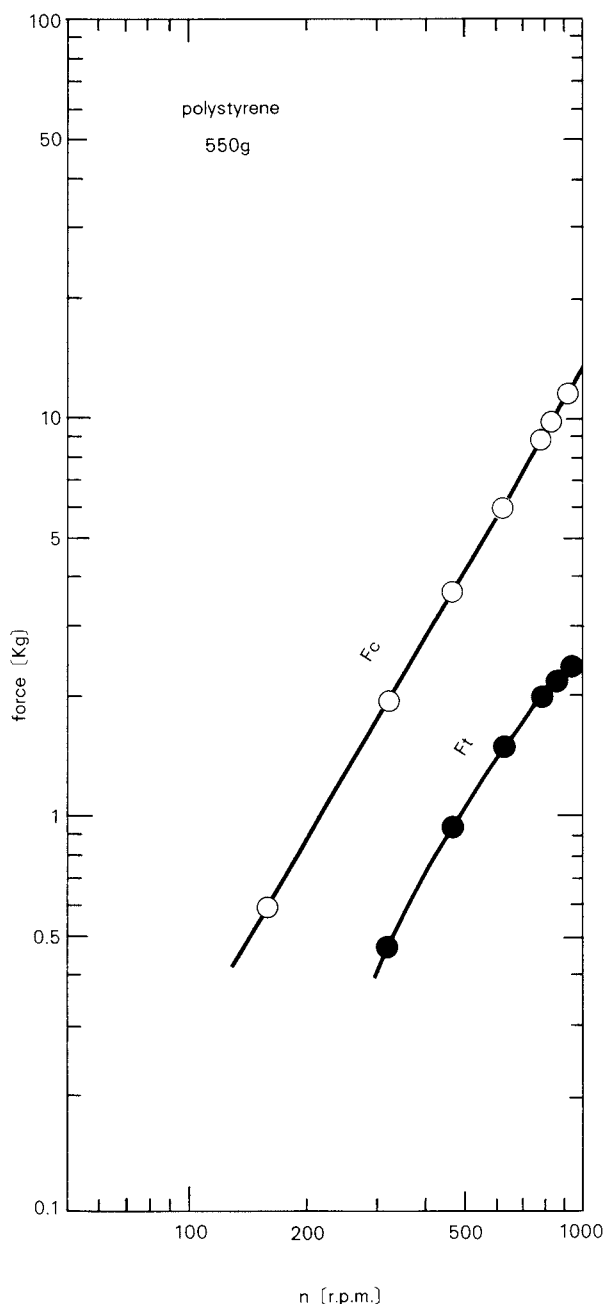


Fig. 5 Variation with rotation speed ( $n$ ) in the radial and tangential forces acting on the inner piece tip

Figure 4 shows the relationship between the rotation speed and the tangential force acting on the inner piece at the maximum charge of the material. The polystyrene beads were not ground at all under these conditions, though they are rather brittle among the plastic resins. In this case, the large amount of energy consumed was not utilized for size reduction but was converted into heat. The heat produced

by the intense attrition between the particles is supposed to be closely related with the mechanofusion effect, discussed in the next section.

In Fig. 4 is also shown the variation in the tangential force on the inner piece with the rotation speed at a certain charge of talc powder which was obtained from Fig. 2. The tangential force of talc at the same revolution speed was three times greater than that of polystyrene beads. This fact seems to be attributed to the difference in the physical properties of the feed material and would help to elucidate the mechanisms of fine grinding as well as of the mechanofusion effect.

Figure 5 shows the variation in the radial force acting on the inner piece as well as the tangential force measured independently at a charge of 550 g of polystyrene beads at the rotation speed using the same type of machine as the foregoing. The log-log plot of the radial force against the rotation speed shows a linear relationship, but that of the tangential force tends to be bent. The radial force is related to the compressive force working on each particle, while the tangential force is related to the shearing force or attrition.

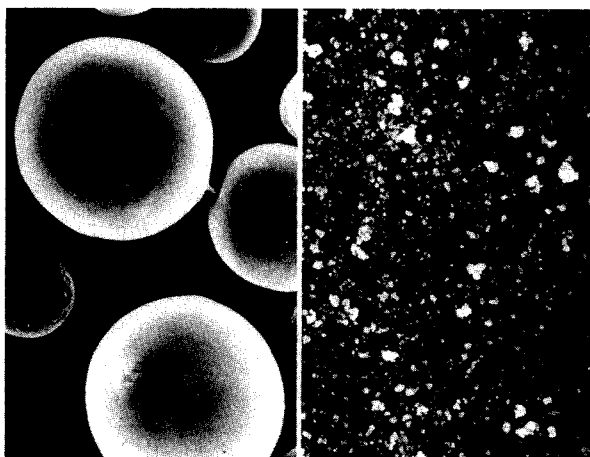
### 3. Examples of mechanofusion effects

Mechanofusion treatment is a technique to create new powder materials by the mechanochemical surface fusion of different particles. The authors have already investigated combinations of more than 100 kinds of materials, but there are still countless possible raw materials yet to study.

Several examples of mechanofusion will be reported later, though some of the material properties, the mixing ratio or the applications cannot yet be published in detail because most of them are new materials still under development. (The size after a material name indicates the average value.)

#### 3. 1 Polymethylmethacrylate (PMMA) (5 $\mu$ m) + TiO<sub>2</sub> (0.015 $\mu$ m)

By the treatment of the mixture of these two materials with the Angmill system, the finer TiO<sub>2</sub> particles are firmly fixed onto the surface of the PMMA spheres and do not separate even by violent agitation in the water.



PMMA ( $5\mu\text{m}$ )

TiO<sub>2</sub> ( $0.015\mu\text{m}$ )

Photo 1 Raw materials

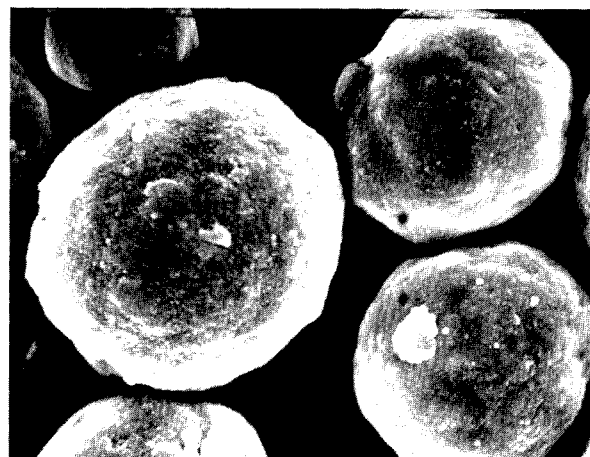


Photo 2 Treated materials  
(PMMA + TiO<sub>2</sub>)

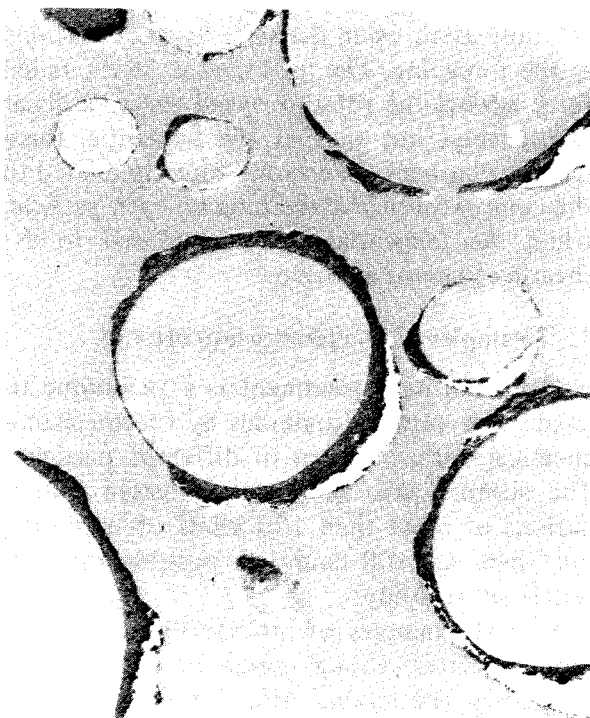


Photo 3 (a) The TEM picture of sliced treated particles.



Photo 3 (b) Thickness of the TiO<sub>2</sub> layer is about  $0.5\mu\text{m}$ .

This combination was the first object of our research on mechanofusion and brought to light interesting changes in various physical properties.

**Photo 1** shows the SEM picture of two kinds

of raw materials. The surface of the particles produced by mechanofusion treatment is shown in **Photo 2**. **Photos 3 (a)** and **(b)** are TEM pictures of the treated particles sliced with a microtome.

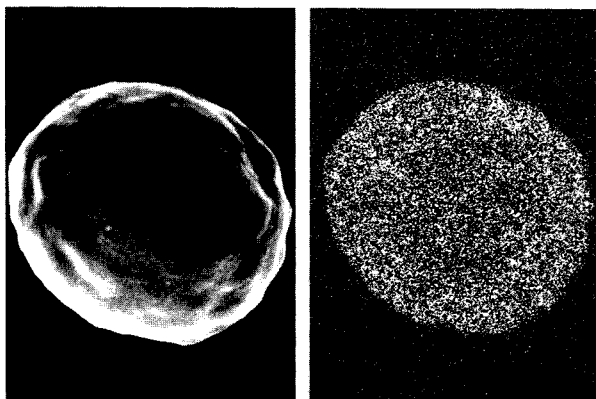


Photo 4 Mapping of Ti by X-ray Microanalyzer

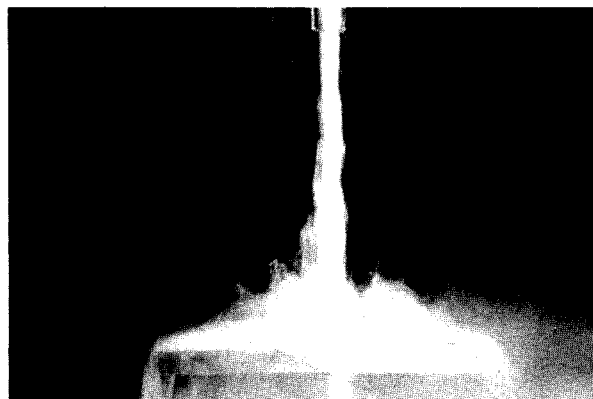
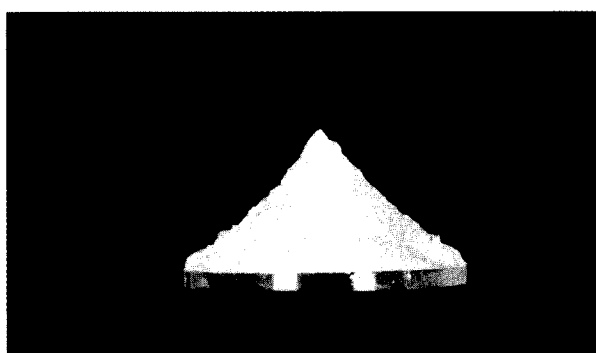
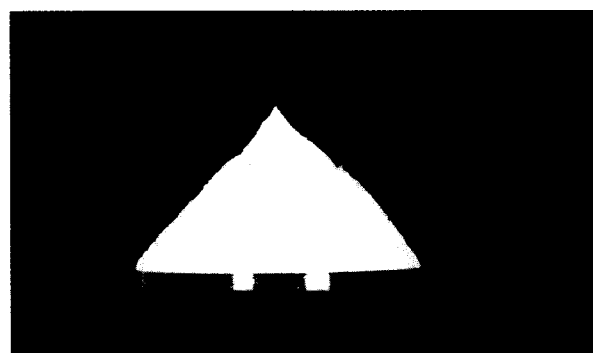


Photo 5 The treated powder flows like a fluid



(PMMA)



(TiO<sub>2</sub>)

Photo 6 The Angle of repose of both raw materials.

The mapping of the chemical elements with an X-ray microanalyzer (Photo 4) indicates that the element Ti is scattered uniformly on the surface of the PMMA particle.

The PMMA powder treated with TiO<sub>2</sub> by mechanofusion flows like a fluid, and the angle of repose becomes nearly zero (Photo 5), though both raw materials have very low flowability (Photo 6).

Figure 6 shows how the angle of repose of the product measured by an injection method with a Powder Tester changes as the content of TiO<sub>2</sub> increases. In the figure, the result of the product of mechanofusion treatment is compared with one that had undergone a several-hour coating operation using a pot mill. The angle of repose of the mechanofusion product decreased to nearly 0 degrees at a TiO<sub>2</sub> content of 10%, while that of the mixture processed with a pot mill did not change so much.

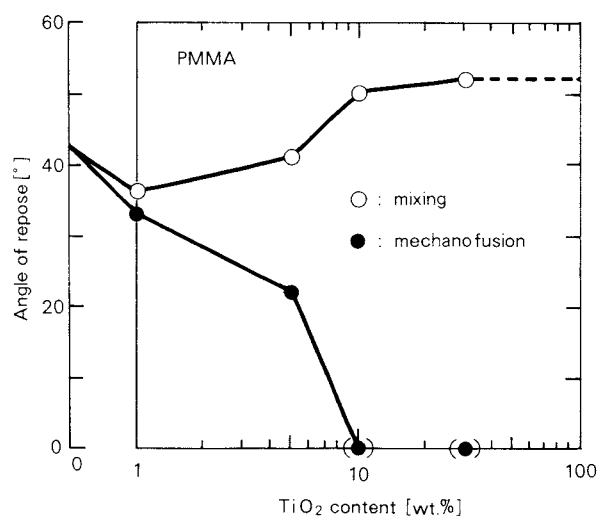


Fig. 6 The effect of TiO<sub>2</sub> content on the angle of repose

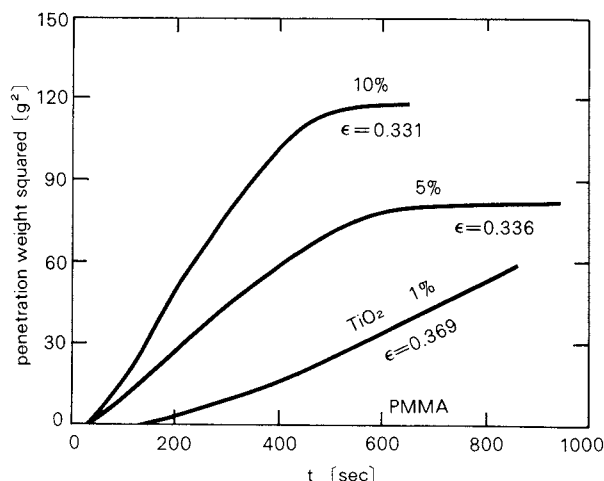


Fig. 7 Change in the penetration rate of PMMA powder with TiO<sub>2</sub> content

Figure 7 shows the variation in the rate of penetration into the powders obtained by mechanofusion. The penetration rate was measured with a Penet analyzer, which has been developed to evaluate the wettability of powders by measuring the penetration rate of a liquid into a powder bed. No water is sucked up into the hydrophobic PMMA powder. The results show that the wettability is improved by increasing the TiO<sub>2</sub> content. The PMMA powder mixed with 30% TiO<sub>2</sub> using a pot mill indicated a one-fifth penetration rate of the product by mechanofusion treatment containing 10% TiO<sub>2</sub>.

### 3. 2 Polystyrene resin (PS) + carbon black

A polystyrene resin was prepared to have an average size of about 10 μm by grinding and classification. The temperature control is the most important point in the mechanofusion operation. The ground particles having an irregular shape are rounded to improve their flowability by mechanofusion, as seen in the electron micrographs (Photo 7).

This combination could be applied to the development of materials for electrostatic copying machines.



Photo 7 upper : Ground polystyrene resin  
lower : Particle treated with carbon black.

### 3. 3 Ground PS (10 μm) + PMMA (0.5 μm)

Photo 8 shows the progress of the mechanofusion process with the lapse of time, where the PMMA spheres having an average size of 0.5 μm are being fixed onto the surface of the ground polystyrene particles used as a raw material in the above 3. 2. It is observed that the PMMA particles having a higher melting point are buried in the polystyrene spheres having a lower melting point.

### 3. 4 SiO<sub>2</sub> (1 μm) + TiO<sub>2</sub> (0.015 μm)

The cross-sectional electron micrograph of the particle obtained by the mechanofusion effect (Photo 9) displays the TiO<sub>2</sub> particles firmly fixed onto the surface of the SiO<sub>2</sub> sphere. The material treated by mechanofusion was not separated by agitation in water but settled out to leave clear water, while the mixture processed by a pot mill produced a turbid suspension containing fine TiO<sub>2</sub> particles separated from the SiO<sub>2</sub> spheres.



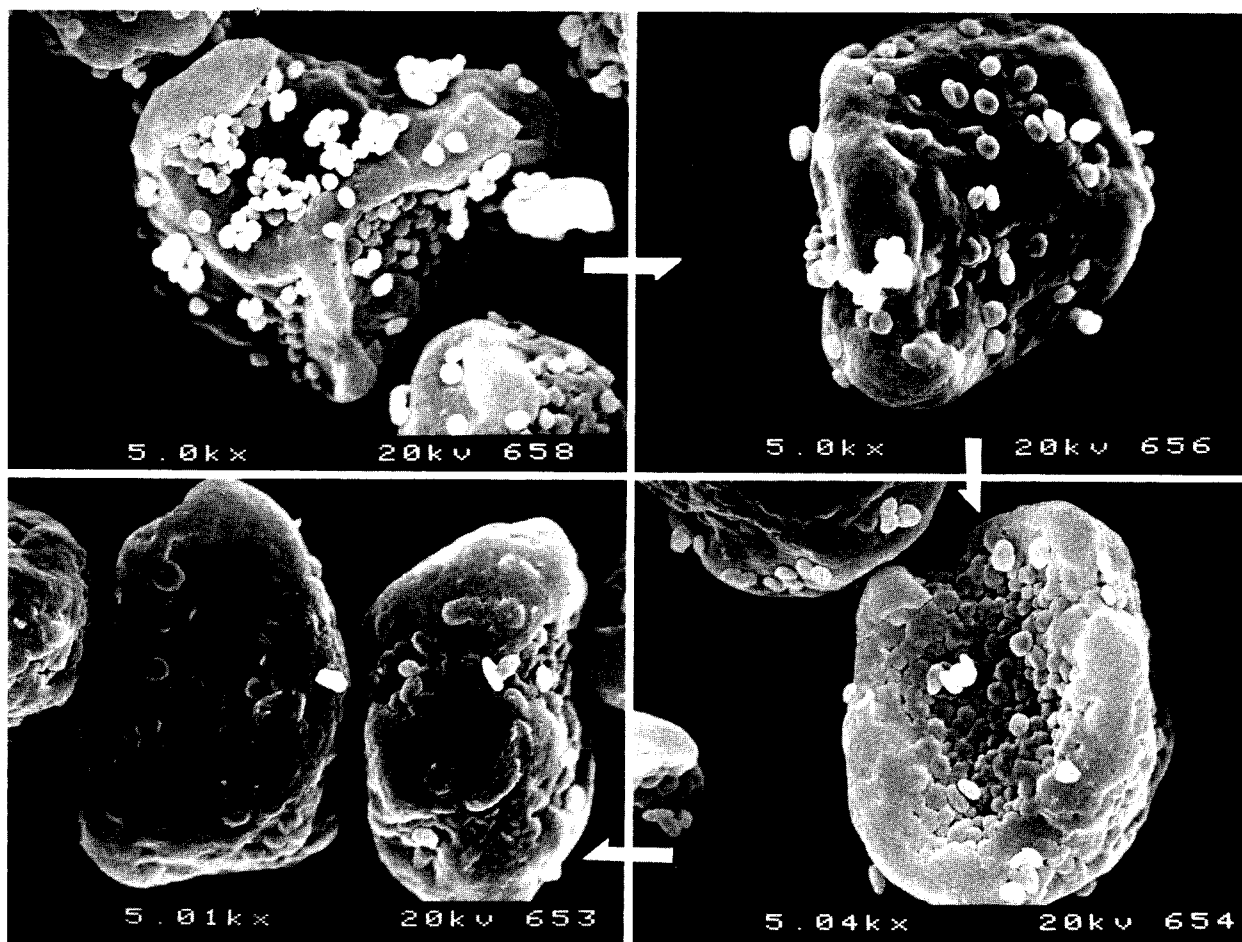
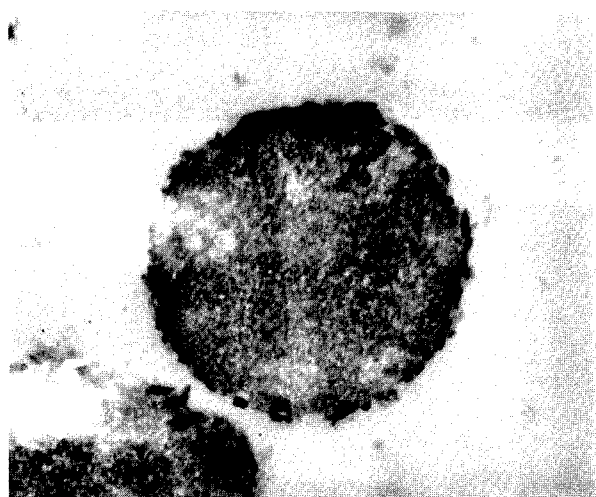


Photo 8 Polystyrene particles treated with PMMA spheres ( $0.5\mu\text{m}$ )



$\times 10,000$

Photo 9 Cross-sectional picture of the  $\text{SiO}_2$  sphere ( $1\mu\text{m}$ ) treated with the  $\text{TiO}_2$  particle ( $0.015\mu\text{m}$ )

### 3. 5 PMMA ( $5\mu\text{m}$ ) + PTFE ( $0.1\mu\text{m}$ )

The polytetrafluoroethylene (PTFE) material used for mechanofusion was a product ground by a jet mill and had an average size of about  $10\mu\text{m}$ . The magnified picture proves that the particles consist of firmly agglomerated spheres with an average diameter of about  $0.1\mu\text{m}$  (Photo 10 a). When the PTFE agglomerates were processed by the Angmill system with the PMMA powder in a certain ratio, they were dispersed to the single spheres and fixed onto the surface of PMMA particles by mechanofusion (Photo 10b).

Figure 8 shows the charge distributions of the raw material of PMMA and the treated product measured with an E-SPART analyzer (Particle Charge Spectroanalyzer). The PMMA particles were almost uncharged, while the PMMA treated with the PTFE spheres showed a strong negative polarity.



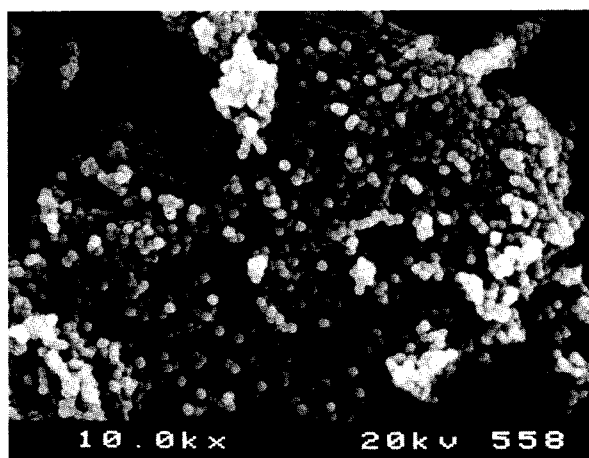
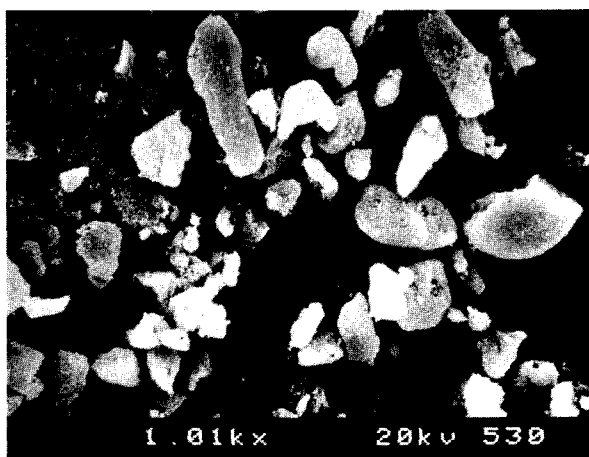


Photo 10 (a) Ground PTFE resin.  
upper :  $\times 1,000$   
lower :  $\times 10,000$

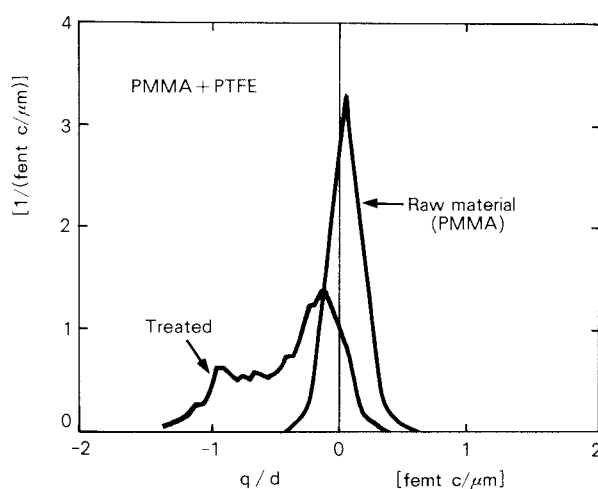


Fig. 8 Charge distributions of PMMA and the product treated with PTFE

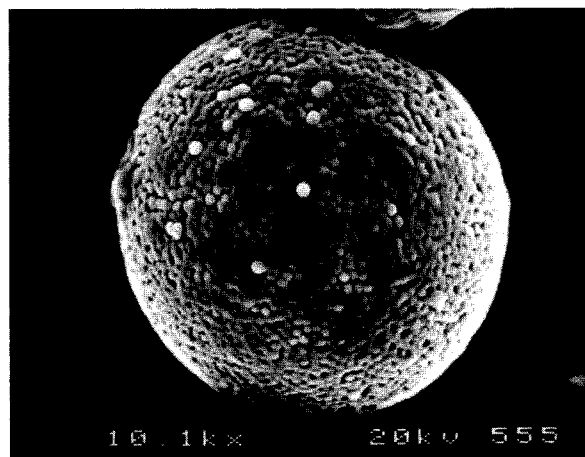


Photo 10 (b) Mechanofusion product of PMMA ( $10\mu\text{m}$ ) and PTFE ( $0.1\mu\text{m}$ )

### 3. 6 Mechanofusion of three kinds of powders

Photo 11 shows a polymer particle with an average size of about  $10\mu\text{m}$  covered with carbon black by mechanofusion. The treated polymer powder was further processed with PMMA particles ( $0.5\mu\text{m}$ ) to produce a three-layer structure (Photo 12).

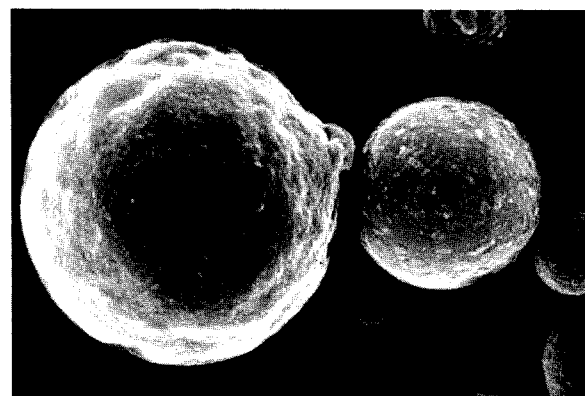


Photo 11 Polymer particles ( $10\mu\text{m}$ ) fixed with carbon black

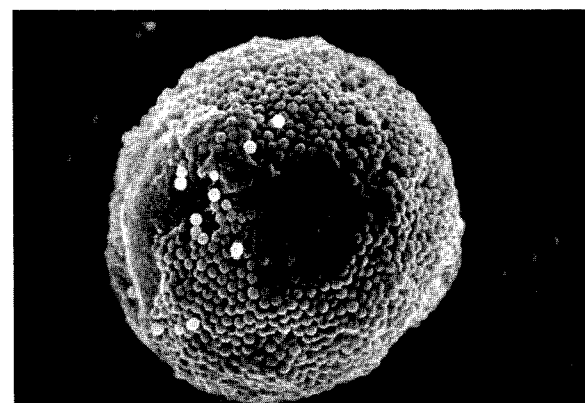


Photo 12 Polymer particle with double surface layers of carbon black and PMMA ( $0.5\mu\text{m}$ )

### 3. 7 Strong dispersion effect (Precision mixing)

As described in the foregoing section, the Angmill system achieved the complete dispersion of the agglomerates by inducing a powerful shearing force even on the submicron particles.

This mechanism can be applied to the precision mixing of fine powders, such as pigments and dyestuffs for paint materials.

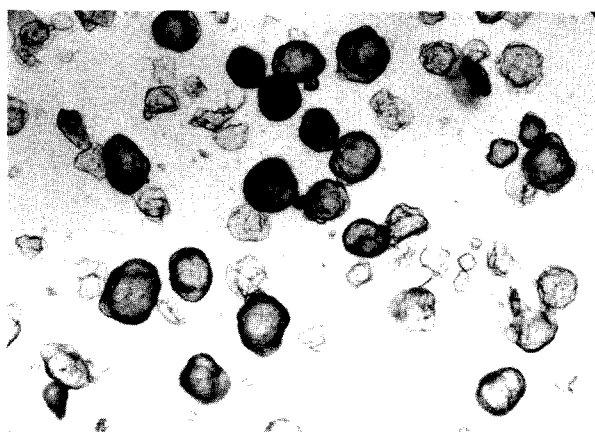


Photo 13 upper : Ground polymer  
lower : Treated product (about 15 $\mu$ m)

### 3. 8 Particle shape control (Sphericalization)

One of the remarkable features of this system is the rounding effect of the irregular particles, as shown in the foregoing polystyrene resin case. **Photo 13** shows the raw material of a polymer obtained by grinding and the treated

product. The latter consisted of roundish particles of nearly the same size. The fine fragments in the raw material seemed to be fused and combined with the coarser core particles.

### 4. Mechanofusion production system

**Figure 9** shows the flowsheet of the mechanofusion system. The raw materials are fed after weighing and mixing in a certain ratio into the treating machine using a modified Angmill system. In the machine, treatment is done in a batch operation for a certain time. Then the product is taken away swiftly from the main chamber and collected for delivery.

The entire system is controlled automatically with a computer.

### 5. Conclusions

The Angmill system has various functions, such as ultrafine grinding, mechanofusion, intense dispersion, sphericalization and so forth. These seem to be attributed to the strong compression and attrition forces, the accompanying heat as well as the electrostatic effect working in a complicated way on the individual fine particles in the range of several microns.

It is especially of great interest to be able to create new materials through mechanofusion as a consequence of the mechanochemical action on various powders having different physical properties.

A great deal of energy is consumed in the research and development of new-generation materials in both the academic and industrial fields. The mechanofusion technique is expected to be increasingly applied to the creation of new powder materials in the future.

### References

- 1) Yokoyama, T., K. Urayama et al.: "KONA", No. 1, 53 (1983).
- 2) Yokoyama, T.: Preprint for the 20th Forum on Powder Technology, P. 57, Tokyo, August 28 (1986).
- 3) Koishi, M.: *Journal of the Society of Powder Technology, Japan*, **20**, 772 (1983); *ibid.*, **24**, 18 (1987).

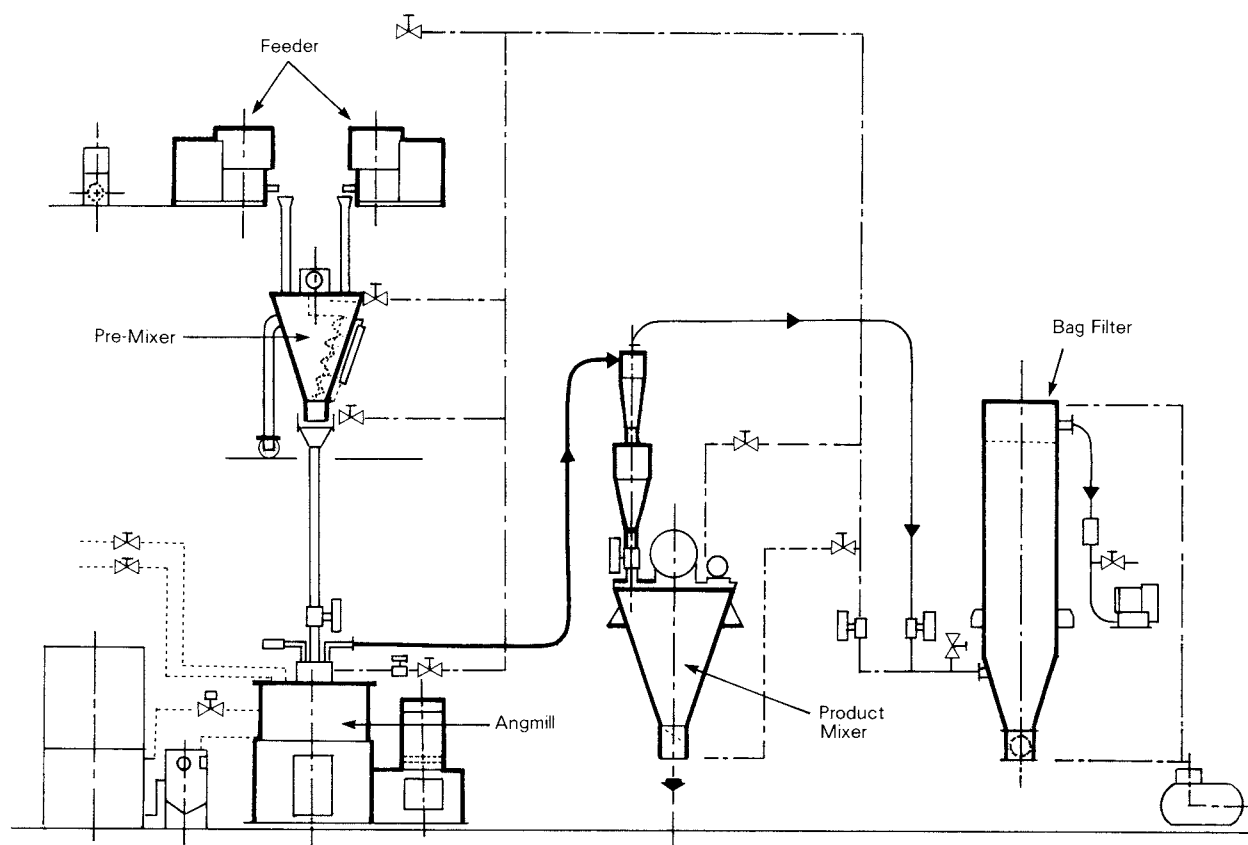


Fig. 9 The flowsheet of the Angmill Mechanofusion System

## Review

# Spherical Crystallization as a Novel Particle Design Technique for the Development of Pharmaceutical Preparations

Yoshiaki Kawashima

Gifu Pharmaceutical University\*

## 1. A particle design technique for the development of pharmaceutical dosage forms

To develop highly qualified solid dosage forms to assure accurate drug delivery, highly functional powdered materials and highly elaborated (stable and reliable) powder processing are required. The functional properties of powder are classified into three groups;

- 1) primary function: intrinsic properties of particles (e.g. crystalline form, particle size, particle shape, etc.)
- 2) secondary function: assemblage properties of massed particles (e.g. flowability, packability, etc.)
- 3) higher level multiple function: properties responsive to environmental factors (e.g. pH, humidity, heat, light, etc.)

Particle design is done to improve the properties of particles, to impart a new function to particle preparations, and to guarantee more stable and reliable powder processing. It is difficult to simultaneously design multiple functions of particles, so particle design has been conducted in several steps. A further modification of particle properties sometimes damages the already modified properties. The development of an efficient particle design technique has long been desired to simultaneously control both primary and secondary particle properties. The microencapsulation process<sup>1)</sup> is assumed to be one of the methods of accomplishing this object. In this process, the pre-design of the core particle to be encapsulated by modifying particle size, shape<sup>2)</sup> and surface property<sup>3)</sup> is necessary to optimize the encapsulation process. The author has been searching for a particle design technique to modify the primary and secondary functions

of particles in one step during the crystallization process as a last step in the preparation of particles. The spherical crystallization technique was developed as a particle design technique to meet such requirements.

In this review, the primary design of particles to improve their micromeritic properties and multiple design to develop a new dosage form of pharmaceuticals by using this technique are described. Recent developments in research on the multiple designs of powdered materials by conventional techniques are also reviewed. Finally, the activities of the division of Particulate Preparations and Designs of the Society of Powder Technology, Japan to develop particle design technology in Japan are introduced.

## 2. Primary design of particles by the spherical crystallization technique

### 2. 1 The spherical crystallization technique

The spherical crystallization technique is a novel multiple operation process including crystallization and agglomeration processes, by which the crystals produced are directly agglomerated into spherical forms. The primary and secondary functional properties of particles are controlled simultaneously by the crystallization and agglomeration operations of this technique, respectively. In this process, two or three partially miscible solvents are used as crystallization solvents. When a proper composition of the mixture is chosen, phase separation occurs and a small amount of solvent is liberated. This solvent preferentially wets the crystals produced and aggregates them into the agglomerated form. Using a three solvents system, a solvent, a non-solvent and a third solvent that is miscible with the former two solvents are chosen. For salicylic acid, water-chloroform-alcohol is a representative solvent combination. Spherical crystallization is carried out in the shaded region of the triangle phase

\* Mitahora-Higashi, Gifu 502  
TEL. 0582 (37) 3931

Received May 20, 1987

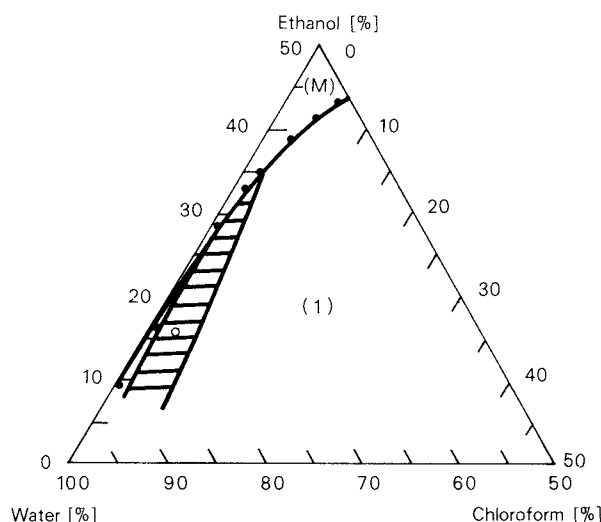


Fig. 1 Diagram showing the solubility of chloroform in the ethanol–water mixture. Chloroform was miscible (M) in the region above the solid line and immiscible (I) in the region below the solid line. Acceptable spherical crystallization occurred in the shaded region.

in Fig. 1, in which a small amount of liberated chloroform agglomerates the precipitated crystals. When the system is sheared, the aggregates of crystals transform into a spherical form. Therefore, this technique has been termed “spherical crystallization”<sup>4)</sup>.

In the spherical crystallization process, the mass growth rate of particles is proportional to the difference between the supersaturated and equilibrium concentrations of solute in the solvent. However, the linear growth rate of particles is independent of the degree of supersaturation of solute in the solvent. The particles still grow even after the mass growth rate becomes null. This phenomenon indicates that the particles grow by the agglomeration of crystals themselves as well as by crystallization, and they also grow by agglomeration alone after crystallization is finished<sup>5)</sup>. Spherical crystallization processes are classified into three groups, i.e. temperature decreasing, solvent change and salting out methods.

## 2. 2 Primary designs of particles by the spherical crystallization technique

The spherical crystallization technique can improve powder processing by modifying the poor micromeritic characteristics of crystals to the desired ones. It is difficult to directly compress salicylic acid crystals due to their charac-

Table 1 Micromeritic properties of primary crystals and agglomerates

Micromeritic properties	Agglomerates	Primary crystals
Angle of repose	36°	51°
$a^a$	0.0955	0.3397
$b^a$	0.0466	0.0295
$k^b$	0.0049	0.0092
Closest packing density	0.488 g/cm <sup>3</sup>	0.160 g/cm <sup>3</sup>
Tablet	Compressible <sup>c</sup>	Not compressible

<sup>a</sup> Parameter in Eq. 5. <sup>b</sup> Parameter in Eq. 6. <sup>c</sup> Tablet properties: diameter, 10.05 mm; thickness 4.14 mm; average weight, 0.382 g; weight variation, 2.56% (the maximum percentage difference from the mean weight).

teristic needle shapes, which are responsible for their poor flowability and packability. The spherical crystals designed by this technique can be directly compressed into tablets, due to their improved micromeritic properties, as shown in Table 1. The wettability of crystals can be improved by increasing the proportion of water in the mixed solvents of chloroform-ethanol-water<sup>6)</sup>.

The spherical crystallization technique can

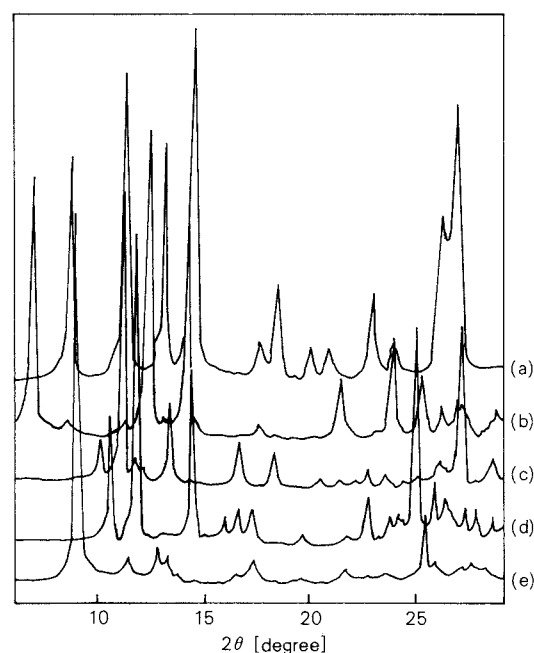


Fig. 2 X-ray powder diffraction patterns of agglomerates, anhydrous theophylline, theophylline monohydrate, and aminophylline. Key: (a) theophylline monohydrate: (b) anhydrous theophylline: (c)  $\alpha$ -form of agglomerates: (d)  $\beta$ -form of agglomerates, aminophylline: (e)  $\gamma$ -form of agglomerates.



Table 2 Effect of organic solvents used on spherical crystallization

Organic solvent	Water in the system, mL	Drug and water contents in the agglomerate, %			Average diameter of agglomerate, mm	Solubility of water <sup>a</sup>
		Theophylline	Ethylene-diamine	Water		
1-Hexanol	10.00	84.86	15.15	0.48	0.86	5.85
Isopropyl acetate	3.75	82.82	16.43	5.78	1.55	1.66
Isobutyl acetate	3.25	81.38	17.19	6.32	1.45	1.44
Isoamyl acetate	2.25	84.30	15.74	5.28	1.30	—
Benzene	1.95	83.78	15.79	4.98	0.81	0.0385
Toluene	1.60	83.65	16.27	5.31	0.90	0.0373
<i>n</i> -Hexane	0.25	82.04	17.46	6.19	1.40	0.0073
<i>n</i> -Heptane	0.13	83.17	16.77	5.57	1.35	0.00897
Chloroform	4.00	85.13	15.47	8.31	1.35	0.0118 <sup>b</sup>
Aminophylline <sup>c</sup>	—	83.39	14.39	4.21	5.52( $\mu\text{m}$ ) <sup>d</sup>	—

<sup>a</sup> Solubility in the organic solvent (v/v %) at 20°C. <sup>b</sup> Solubility at 22°C. <sup>c</sup> Prepared by a conventional method (4).

<sup>d</sup> Measured by a photographic counting method.

be applied to the reaction system as well as to the crystallization process. Spherically designed aminophylline crystals can be produced directly during the reaction of theophylline with ethylenediamine in the mixture of ethanol-organic solvent-water. In the conventional reaction system, absolute ethanol is used as the reaction solvent. The organic solvents employed in this process are listed in Table 2. Fifteen to thirty minutes after starting the reaction, the produced fine white crystals of aminophylline were transformed into spherically agglomerated crystals. The agglomerated crystals have three different crystalline forms, i.e.  $\alpha$ -,  $\beta$ - and  $\gamma$ -forms, depending on the type of organic solvents used. The X-ray diffraction patterns of the polymorphs are shown in Fig. 2. The  $\beta$ - and  $\gamma$ -forms have 1 and 2.5 moles of water of crystallization, respectively, but the  $\alpha$ -form has none. Aminophylline synthesized by the conventional method corresponds to the  $\beta$ -form. In Table 2, the agglomerates with water contents of 0.48%, 4.21~6.32% and 8.31% are identified with the  $\alpha$ -,  $\beta$ - and  $\gamma$ -forms, respectively<sup>7)</sup>. The agglomerates are directly compressible microspheres, the diameters of which can be controlled easily by changing the agitation speed of the system and the amount of water in the reaction system, as shown in Fig. 3<sup>8)</sup>.

This technique can be adapted to the multiple crystallization system including two pharmaceuticals to produce a new molecular complex. When indomethacin ( $\gamma$ -form) and epirizole (anhydride) are crystallized in the mixture of ethanol-water system, a spherically crystallized

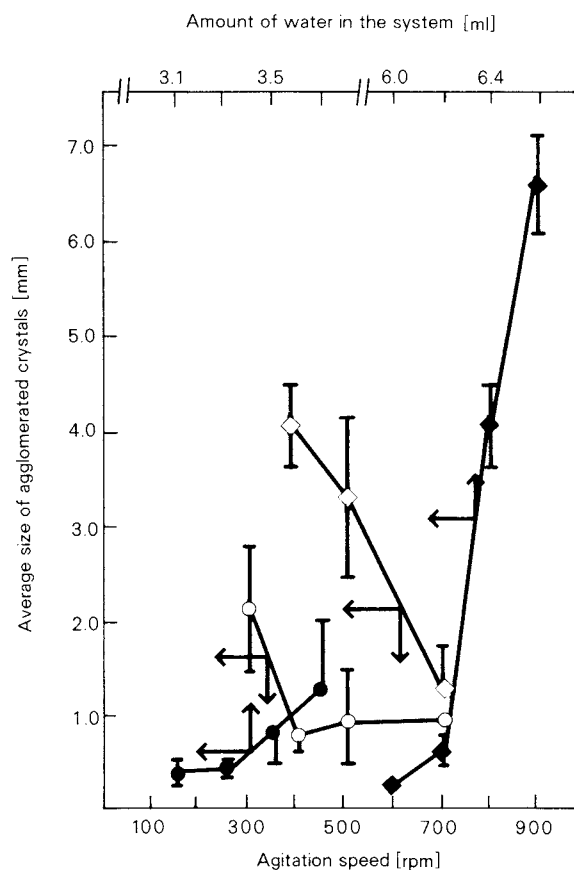


Fig. 3 Effects of agitation speed and amount of water in the system on average size (50%) of agglomerated crystals. The size range between 16 and 84% is described by deviation bars. The medium for agglomeration is methanol ( $\circ$ ,  $\bullet$ ) or ethanol ( $\diamond$ ,  $\blacklozenge$ ). The residence time is one hour after removal of the agglomerates adhering to the vessel.

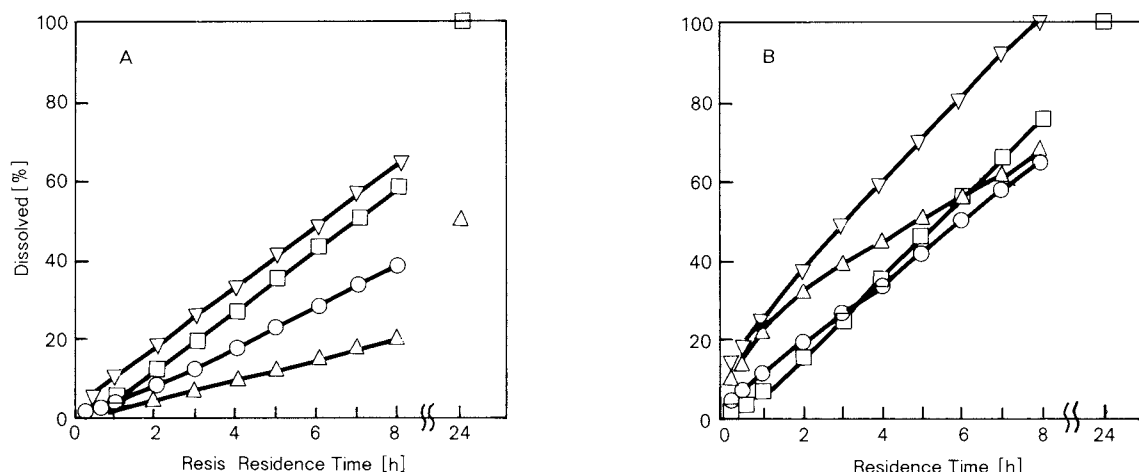


Fig. 4 Dissolution profiles of indomethacin (A) and epirizole (B) in JPX disintegration test solution 2 at 37°C by a rotating disk method.  
 Key: ( $\circ$ ) physical mixture of  $\alpha$ -indomethacin-epirizole; ( $\nabla$ ) physical mixture of  $\beta$ -indomethacin-epirizole; ( $\Delta$ ) physical mixture of  $\gamma$ -indomethacin-epirizole; ( $\square$ ) spherically agglomerated crystals prepared by method 2.

polymorphic mixture of indomethacin ( $\beta$ -form) and epirizole (amorphous) is produced. In the ethylacetate-water mixture, a new molecular complex of indomethacin and epirizole with a molecular ratio of 2:1 is formed at the loading of epirizole > 65%. The process of the dissolution of indomethacin in the agglomerate of the new complex is described by zero-order dissolution kinetics. The rate of the dissolution of indomethacin of the complex is three times faster than that of the metastable  $\beta$ -form of indomethacin. The dissolution kinetics of epirizole in the complex is also represented by the zero-order rate process, as seen in Fig. 4.

An improved therapeutic effect of the new complex might be expected, since it was reported that co-administration of epirizole reduced the adverse effects of indomethacin and improved its therapeutic action<sup>9</sup>.

### 3. Highly qualified designs of particles by spherical crystallization

The primarily designed particles are usually further modified to impart more sophisticated functions to them to produce highly qualified powder preparations. This process is termed the highly qualified design of particles. The spherical crystallization technique can design

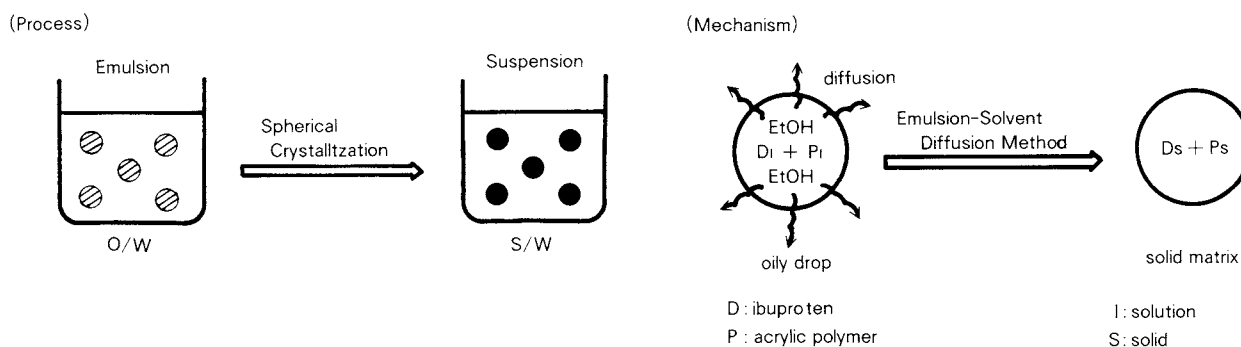


Fig. 5 The procedure for preparation and the mechanism of microspheres

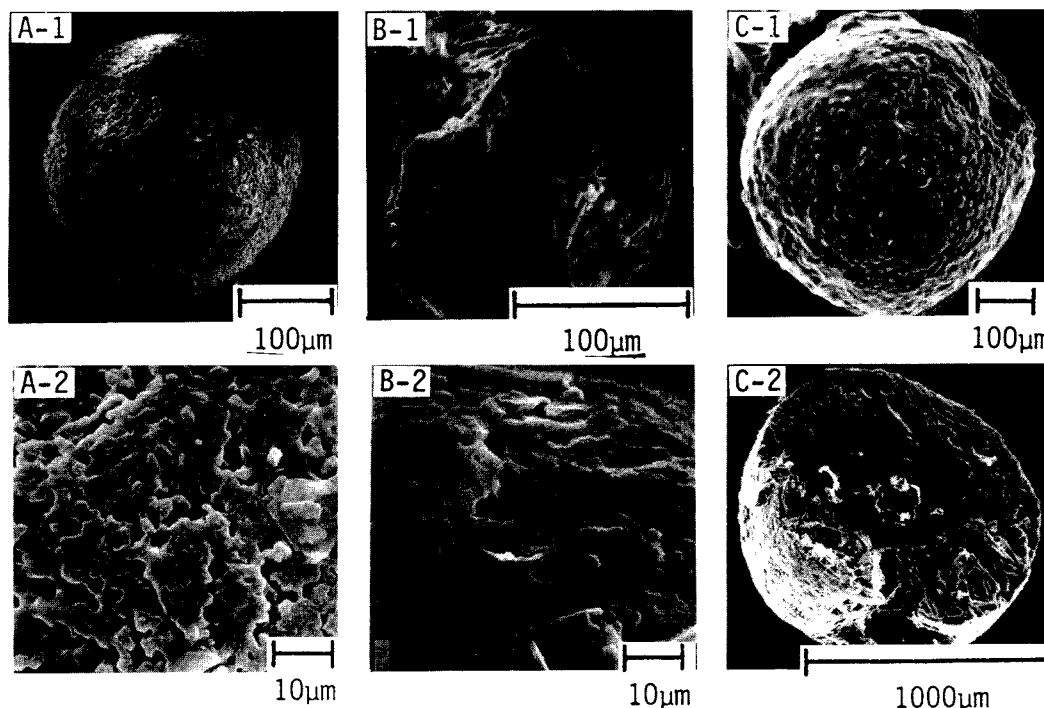
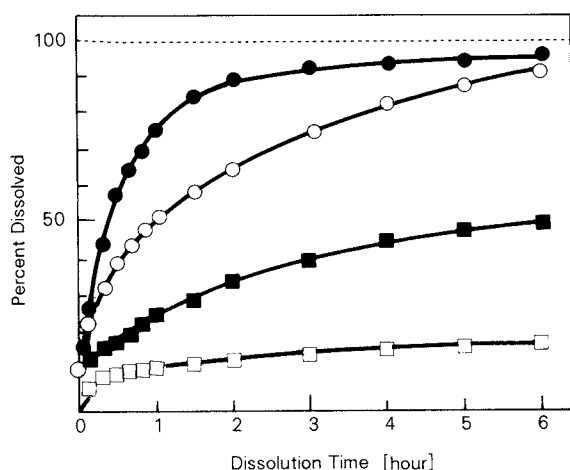


Fig. 6 Scanning electron microphotographs of microspheres  
A: Formulation No. 1 (Ibu: S100=10:1)  
B: Formulation No. 2 (Ibu: L100-55=10:1)  
C: Formulation No. 6 (Ibu: RS100=2:1)



Key	Formulation	Ibu: Eud	Dissolution medium
○	No. 1	S100 (10:1)	JPX No. 2 Water
□	No. 1	S100 (10:1)	Water
●	No. 2	L100-55 (10:1)	JPX No. 2 Water
■	No. 2	L100-55 (10:1)	Water

Size fraction: ○, ●: -16+48mesh  
□, ■: -48+80mesh

Fig. 7 Dissolution profiles of microspheres

particles to be highly qualified at the same time in the primary design stage. In this paper, preparations of controlled release microspheres of ibuprofen with acrylic polymer are described. Ibuprofen is coprecipitated with acrylic polymer to be embedded in the polymer. The ethanol solution of ibuprofen and the polymer is poured into water with agitation. In the initial stage, the ethanol solutions of drug and polymer are dispersed in water in the form of fine droplets. The ethanol is diffused out of the droplets, and water enters them. During this procedure, the droplets are solidified through the coprecipitation of drug and polymer, by which matrix-like microspheres are produced. This mechanism is illustrated in Fig. 5. The diameter of microsphere is controlled by changing the agitation speed and the concentration of the surfactant added to the water. The surface topographies of the microspheres are shown in Fig. 6. When the concentration of polymer in the system is low, many micropores are produced on the surface of the microsphere. The pore diameter and the number of micro-

pores are reduced by increasing the polymer concentration. It is suggested that the drug release rate from the microsphere can be controlled by changing the polymer concentration in the system. The drug release rate is also determined by the characteristics of the polymer used, e.g. solubility depended on pH. Eudragit® RS is useful in retarding the drug release rate. Eudragit® S and L100-55 can be used as an enteric coating polymer, as shown in Fig. 7<sup>10)</sup>.

#### 4. The multiple design of particles by conventional methods

To accomplish successful multiple designs of particles, highly qualified materials and elaborate equipment should be selected. With respect to materials, the development of highly functional excipients and polymers is required. From the viewpoints of safety and reliability, the modification of widely used materials is preferable. New modified materials, such as partially pregelatinized corn starch, microcrystalline cellulose and carboxymethylcellulose sodium and lactose for direct compression, have been produced<sup>11)</sup>. Chitosan and purlan are expected to be used as novel biomaterials<sup>12)</sup>. Biodegradable polymers have been extensively researched to develop new dosage forms which can be implanted or injected<sup>13)</sup>. With regard to coating polymers, aqueous coating polymers have been developed to avoid the use of organic solvent.

The development of new equipment for multiple particle designs has been desired. New mechanics which can simultaneously design the primary properties of particles should be introduced. The application of fluidized and spouted beds to coat discrete particles may meet the requirement<sup>14)</sup>. The system of coating in a vacuum may present another way<sup>15)</sup>.

#### 5. Activities of the Division of Particulate Preparations and Designs of the Society of Powder Technology, Japan and the Division of Particulate Modification Technology of the Association of Powder Process Industry and Engineering in Particle Design Technology

The Division of Particulate Preparations and Designs of the Society of Powder Technology, Japan was founded in 1985 to systematize the techniques for particle designs developed in

various fields, such as pharmaceutical, chemical, agricultural and food industries, as one field of powder technologies, e.g. particle design technology. Particle design technology should be directed towards needs-oriented science to establish a new system of developing multifunctional particulate preparations. To accomplish this object, knowledge and experience in various fields, including applied chemistry, chemical engineering, electronics, material science and biopharmacy, etc., should be systematically accumulated. Such information should be open to the public so it will be available for applications in industries. The division of Particulate Preparations and Designs (Chairman: Prof. Y. Kawashima, Gifu Pharmaceutical University) sponsors a symposium on particulate preparations and designs every year co-sponsored by other academic societies and associations, such as pharmacy, chemical engineering, ceramics, material science, food, etc. October 29 and 30, 1987, the 4th symposium will be held in Atami. Prof. D. Duchêne, Université de Paris-sud, and Prof. M. Okazaki, Kyoto University will be invited as special lecturers. Another activity of this division is to standardize the materials, formulations and processing of agglomeration (Chairman of the working group: Prof. H. Sunada, Meijo University).

The division of Particulate Modification Technology was founded in the Association of Powder Process Industry and Engineering in 1985 (Representative, Dr. T. Yokoyama, Hosokawa Micron Corp., Coordinator Dr. Y. Funakoshi, Kyoto Powder Research Laboratory) to stimulate and to link the academic activities of powder process industries. This division sponsors academic meetings, exhibitions and factory tours for engineers. They are usually held three times a year. It also co-sponsors the symposium on particulate preparations and designs.

Both divisions of the Particulate Preparations and Designs and the Particulate Modification Technology cooperate closely to promote the science and technology of particle design in powder technology in Japan.

#### Acknowledgement

A part of this study was supported by a

Grant-in-Aid for General Scientific Research (Grant No. B-62490014) of The Ministry of Education, Science and Culture.

## References

- 1) Deasy, P. B. (Ed.): "Microencapsulation and Related Drug Processes", Marcel Dekker, Inc., New York (1984).
- 2) Koida, Y., M. Kobayashi and M. Samejima: *Chem. Pharm. Bull.*, **34**, 3354 (1986).
- 3) Okada, J.: The Proc. of the 1st Symposium on Particulate Preparations and Designs, p.65 (1984).
- 4) Kawashima, Y., M. Okumura and H. Takenaka: *Science*, **216**, 1127 (1982).
- 5) Kawashima, Y., M. Okumura and H. Takenaka: *Powder Technol.*, **39**, 41 (1984).
- 6) Kawashima, Y., M. Okumura, H. Takenaka and A. Kojima: *J. Pharm. Sci.*, **73**, 1535 (1984).
- 7) Kawashima, Y., S. Aoki, H. Takenaka and Y. Miyake: *J. Pharm. Sci.*, **73**, 1407 (1984).
- 8) Kawashima, Y., S. Aoki and H. Takenaka: *Chem. Pharm. Bull.*, **30**, 1900 (1982).
- 9) Kawashima, Y., S. Y. Lin, M. Ogawa, T. Handa and H. Takenaka: *J. Pharm. Sci.*, **74**, 1152 (1985).
- 10) Kawashima, Y., T. Handa, H. Takeuchi and T. Niwa: The 4th International Conference on Pharmaceutical Technology, Paris, June 3-5, 1986.
- 11) Takeuchi, H., T. Handa and Y. Kawashima: *J. Pharm. Pharmacol.*, 1987 accepted.
- 12) Kawashima, Y., T. Handa, A. Kasai, H. Takenaka, S. Y. Lin and Y. Ando: *J. Pharm. Sci.*, **74**, 264 (1985).
- 13) Oppenheim, R. C.: *Int. J. Pharm.*, **8**, 217 (1981).
- 14) Fukumori, Y., T. Fukuda, Y. Takeuchi and Y. Osako: The Proc. of the 3rd Symposium on Particulate Preparations and Designs, p.71 (1986).
- 15) Kawata, M. and S. Goto: The Proc. of the 2nd Symposium on Particulate Preparations and Designs, p.33 (1984).



# The Evaluation of Activity and Reactivity of Mechanically Treated Fine Powdered Materials

Mamoru Senna

Faculty of Science and Technology  
Keio University\*

## 1. Introduction

Being the theme of an international symposium, and for the last two years also that of an international journal, the reactivity of solids is currently one of the most important issues in the research and development of materials.

Although remarkable progress has been made in the last two decades, the quantitative characterization of reactivity is still very limited. There are two reasons for this. The first one is the limited possibility of the direct measurement of the activity, either from a structural (crystallographical) or energetic (thermodynamic) point of view, in spite of the recent development of instrumental analyses. Another one is the diversity of the parameters and their cross terms included in the reactivity. These make the correlation between the specific parameters of activity and reactivity complicated and ambiguous.

In the first issue of this Journal, the present author made a contribution entitled, "Criteria for the Activation of Powdery Materials by Preliminary Mechanical Treatment<sup>1)</sup>", where the factors affecting the rate of transformation of gamma ferric oxide were discussed.

As a result of several recent additional experiments obtained, some generalization now seems to be possible. Thus, a second contribution is being made here which concentrates on: (1) answering the question, what should an appropriate measure or a criteria for the activity of fine powders be; (2) designating the reactivity of finely divided solids; and (3) pointing out the problem of interconnecting the activity and the reactivity. Two important concepts, "effective surface area", and "the availability

of the stored energy" are introduced. Detailed and classified discussion will not be made here but only cited as reference material.

## 2. Excess enthalpy

Excess enthalpy,  $\Delta H^*$ , is understood as one of the standard measures of the activity of solids<sup>2,3)</sup>. Since  $\Delta H^*$  is assessed from the difference in the heats of reaction between activated and intact materials, its determination is also well defined. Experimental methods for determining  $\Delta H^*$  using dissolution calorimetry were explained elsewhere<sup>4)</sup>. Detailed techniques for partially dissolved material were also discussed<sup>5)</sup>.

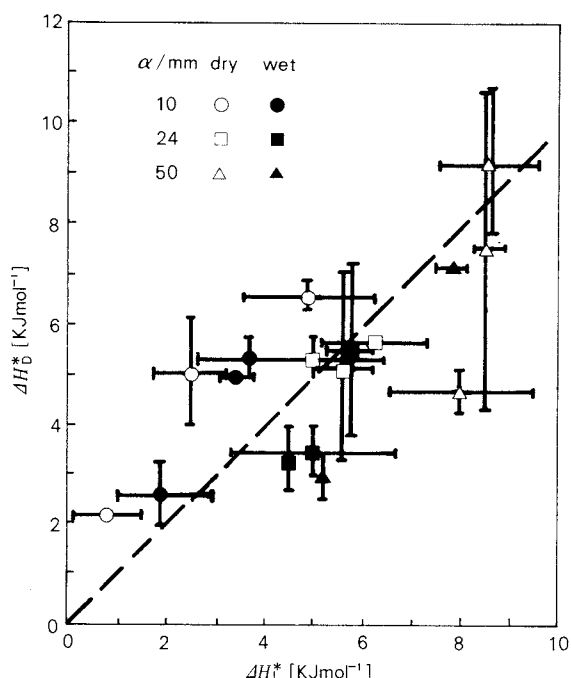


Fig. 1 The relationship between excess enthalpies obtained from dissolution calorimetry,  $\Delta H_D^*$ , and thermoanalysis,  $\Delta H_L^*$ .

\* 3-14-1, Hiyoshi, Kohoku-ku, Yokohama, Kanagawa, 223  
TEL. 044 (63) 1141

Received April 15, 1987

It is also possible to determine the excess enthalpy from decomposition or other heats of reaction, by using thermoanalytical techniques<sup>6)</sup>. An example was given where two excess enthalpies, one from the heat of dissolution and the other from the heat of decomposition, were compared. As shown in Fig. 1<sup>7)</sup>, they tallied fairly well. The problem of the temperature dependence of  $\Delta H^*$ <sup>8)</sup> and related arguments on the role of the entropy term, however, continue to persist. As a case study, the correlation between  $\Delta H^*$  and the rate of decomposition of mechanically activated  $\text{PbCO}_3$  is given below<sup>9)</sup>.

Mechanically activated  $\text{PbCO}_3$  of known excess enthalpy,  $\Delta H^*$ , is subjected to subsequent thermal decomposition. First-order kinetics was applied to the first stage of the isothermal decomposition,  $\text{PbCO}_3 \rightarrow (1/3)(\text{PbCO}_3 \cdot \text{PbO}) + (2/3)\text{CO}_2$ , in an  $\text{N}_2$  flow at temperatures between 523 and 573K. Correlation between the rate constant of decomposition,  $k_p$ , and  $\Delta H^*$  was examined in Fig. 2. Grinding in cyclohexane or with a smaller amplitude brought about a comparable or even higher rate constant, compared at the same network done or the same relative noncrystallinity, in spite of smaller excess enthalpy.

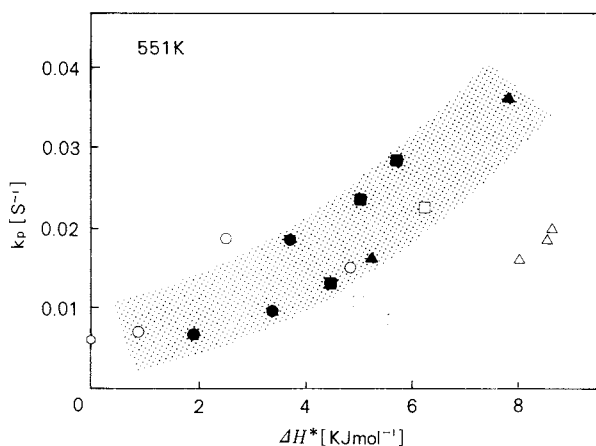


Fig. 2 The relationship between the rate constant of decomposition of preliminary activated  $\text{PbCO}_3$  under different conditions<sup>9)</sup>. Open and filled symbols denote samples ground in air and in cyclohexane, respectively. Circles: ground with an amplitude of 10 mm, squares: 24 mm, and triangles: 50 mm.

### 3. Effective surface area

The equivocal correlation between the excess enthalpy and the rate constant of the reaction discussed above requires some additional parameters other than overall enthalpy, to predict the reactivity of active powdery materials. The concept of "effective surface area" is now introduced as one of typical extensive parameter, for "normalizing" the rate constant of the reaction. A case study is given next<sup>10)</sup>.

Decomposition and dissolution kinetics of vibro-milled  $\text{Mg}(\text{OH})_2$  were studied to elucidate the dominating factors in each reaction<sup>10)</sup>. The specific surface area measured either by air permeability,  $S_p$ , or by BET adsorption,  $S_B$ , decreased after vibro-milling, as shown in Fig. 3. Again, first-order kinetics was applied to the isothermal decomposition reaction in air at temperatures ranging from 583K to 643K. The rate constant of the decomposition,  $k_p$ , increased with increasing grinding time, as shown in Fig. 4. A similar analysis was carried out for

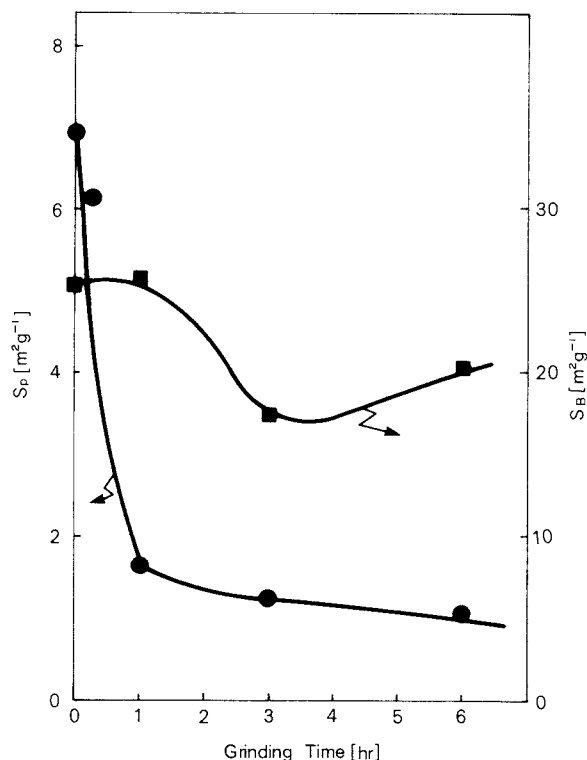


Fig. 3 The variation in surface areas of  $\text{Mg}(\text{OH})_2$  obtained by the air permeability method,  $S_p$  and by the BET method,  $S_B$  with grinding time<sup>10)</sup>.

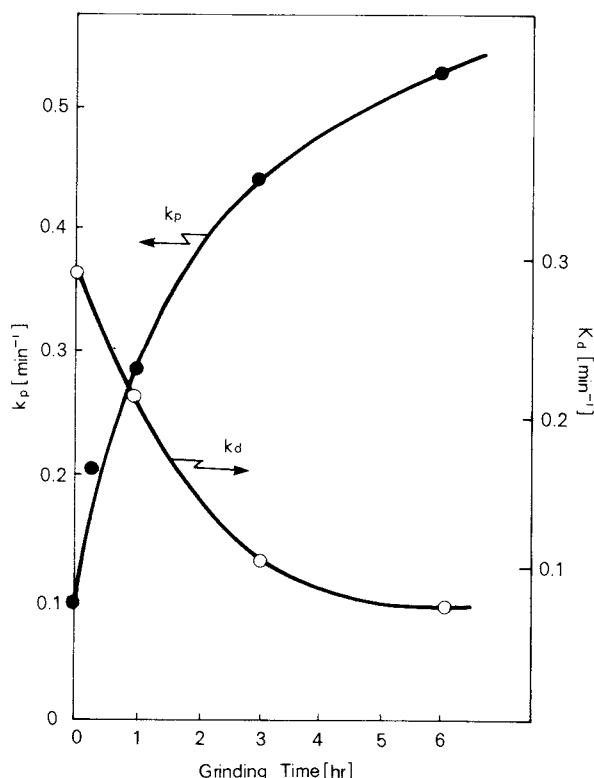


Fig. 4 The variation in the rate constants of decomposition,  $k_p$ , and dissolution,  $k_d$  of  $\text{Mg}(\text{OH})_2$  with grinding time<sup>10</sup>.

the reaction of dissolution into 0.1M EDTA, to which contract sphere model kinetics was applied. In contrast to the case of  $k_p$ , the rate constant of the dissolution,  $k_d$ , measured at temperatures between 283K and 313K, decreased with increasing grinding time, as also shown in Fig. 4.

The difference in the change of reactivity between decomposition and the dissolution reaction seems to be attributed mainly to the difference in the effective surface area of each reaction. Each rate constant divided by an appropriate surface area showed a steep increase with a quick levelling off or slow decrease as the time of activation increased, as shown in Fig. 5. This was similar to the change in the X-ray amorphous portion,  $1-I_f$  as shown in Fig. 5<sup>10</sup>. As shown above, dividing  $k_d$  by  $S_p$  normalized the rate constant. It seems therefore safe to assume that the specific surface area measured by the air permeability method, standing for the characteristics of highly aggregated particles is one of the dominant extensive parameters for the rate of the dissolution reaction. On the other hand, the hypothetical

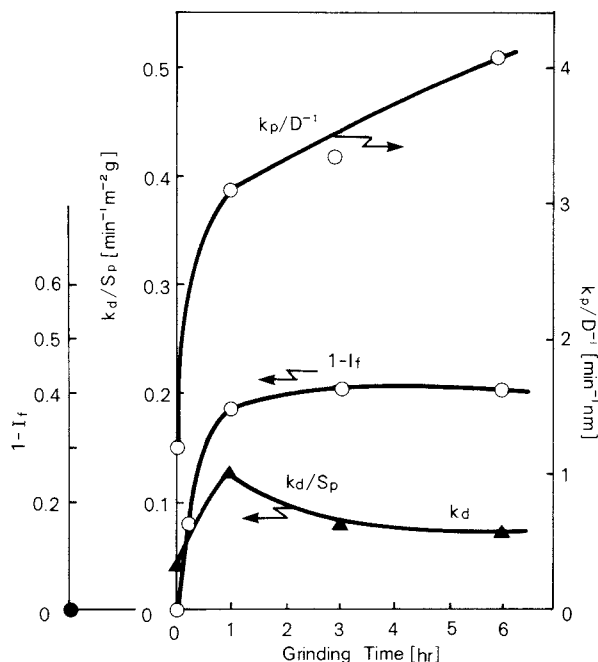


Fig. 5 The variation of  $k_p/D^{-1}$ ,  $k_d/S_p$  as well as  $1-I_f$  of  $\text{Mg}(\text{OH})_2$  with grinding time<sup>10</sup>.  $D$  denotes the crystallite size.

boundary surface of the crystallite seems to play an important role in the decomposition reaction.

#### 4. Availability of stored energy

As mentioned in Section 2, the increase in the reactivity due to mechanical activation cannot always be correlated uniquely with the calorimetric parameter. Although the effective area, mentioned above, serves as a "hidden parameter", which could further explain the correlation between activity and reactivity, it is insufficient.

For mechanically activated materials, one of the main factors in enhanced reactivity is the higher availability of excess free energy for subsequent chemical reactions. The concept of availability includes the feasibility and efficiency of utilizing excess free energy. Factors dominating availability are related to the kinds as well as the distribution of structural imperfections<sup>11</sup>. To quantify and elucidate the above-mentioned availability is one of the most important tasks for better understanding and for the application of mechanical activation.

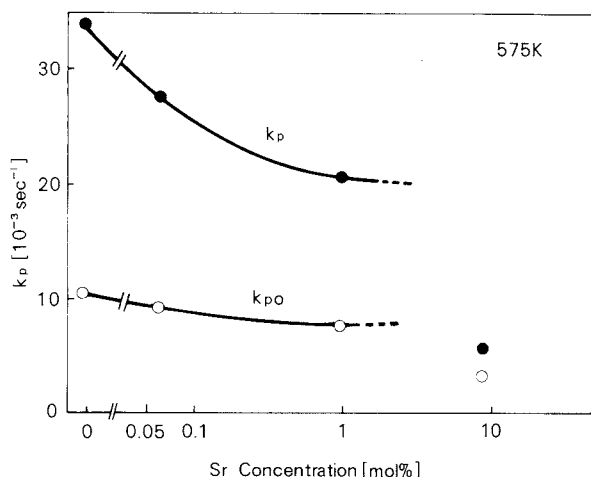


Fig. 6 The variation in the rate constant of decomposition,  $k_p$  for activated (filled symbols) and non-activated lead carbonate with a concentration of doped Sr<sup>12)</sup>.

A third case study given below deals again with the thermal decomposition of  $\text{PbCO}_3$  doped with 0.1 ~ 10 mol % Sr, with and without mechanical activation by vibro-milling<sup>12)</sup>. Excess enthalpy,  $\Delta H^*$ , imparted to the activated materials, remained almost constant, ir-

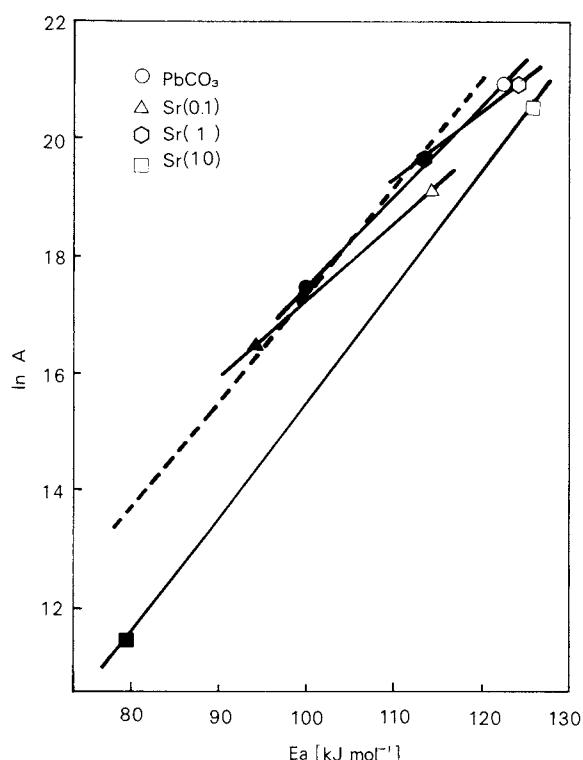


Fig. 7 The relationship between  $\ln A$  and  $E_a$  for the decomposition of Sr-doped lead carbonate<sup>12)</sup>, where  $A$  and  $E_a$  denote the frequency factor and the activation energy.

respective of Sr concentration. The first-order rate constant of isothermal decomposition,  $k_{p0}$ , of the doped materials without mechanical activation decreased only slightly with the increase in the concentration of Sr. For the mechanically activated materials, however,  $k_p$  significantly decreased with the increase in the concentration of Sr, as shown in Fig. 6.

A quasi-linear relationship was found to exist between the apparent activation energy,  $E_a$ , and the logarithm of the pre-exponential factor,  $\ln A$ , of the decomposition, as shown in Fig. 7. This enables the determination of the characteristic temperature,  $T_x$ , at which the Arrhenius plots cross each other, for each group of samples with different Sr concentrations. At  $T = T_x$ , the excess free energy was assumed to become null<sup>3)</sup>. The relationship between  $T_x$  and the decomposition temperature,  $T_D$ , determined from the DSC profile is shown in Fig. 8. The extent of excess free energy dissipated during the decomposition reaction was suspected to decrease due to Sr doping, since it is

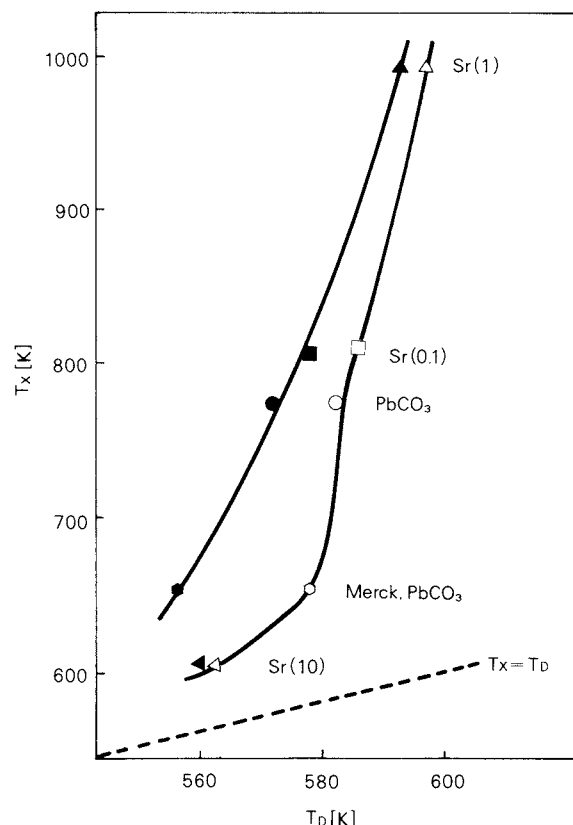


Fig. 8 The relationship between  $T_x$  and  $T_D$  for Sr-doped lead carbonate. Open and filled symbols denote the non-activated and activated materials, respectively.

expected from Fig. 8 that the utility of the stored energy decreases with increasing amounts of doped Sr. The structural imperfection of the decomposed products is one evidence of the above idea. This is an example of the change in availability due to foreign materials.

## 5. Topochemical aspects of mechanical activation

One of the factors closely related to availability is the topochemical distribution of active centers. An attempt was also made to obtain experimental information about the topochemical distribution of active sites on and in mechanically activated  $\text{PbCO}_3$ <sup>13)</sup>. Vibro-milled  $\text{PbCO}_3$  was dissolved into dilute aqueous solutions of acetic acid. For a series of partially dissolved samples, particle size, shape, surface structure and morphology were observed by an SEM.

Finer primary particles on the surface of

aggregates preferentially dissolved and disappeared. With an increase in the extent of partial dissolution,  $X$ , activity parameters,  $\Delta H^*$ , decreased monotonically and approached the values of as-received  $\text{PbCO}_3$ , as shown in Fig. 9. This is obviously attributed to the preferential dissolution of finer and more active particles during acid leaching.

When the same amount of the net mechanical work done was applied to the materials in a vibro-mill with different amplitudes, a difference in the distribution of the active center arose. When the total network done was kept constant, a larger number of smaller impacts were applied to the material when ground at a smaller amplitude. Conversely, the mechanical effect could reach deeper into the interior of the particle when ground at a larger amplitude, the number of hits being smaller. This kind of difference was discussed in conjunction with the effects of different grinding machines<sup>14,15)</sup>. The former inevitably causes a more even distribution of active centers near the surface of the particle.

## 6. Summary

Excess enthalpy, which will eventually be substituted for excess free energy, is experimentally determined from conventional calorimetry or thermal analysis. In spite of being a good and appropriate measure of the activity, a terminology distinct from the definition in thermodynamics, the increase in the rate constants of thermal decomposition of dissolution due to mechanical activation, cannot be correlated uniquely with the excess enthalpy. This is attributed to its dependence on the effective surface area, and to the difference in its availability.

A simple positive correlation between the surface area and the degree of mechanical activation cannot always be expected either, particularly in cases where significant agglomeration takes place due to severe mechanical treatment. The introduction of the concept of effective surface area and its specification serves to better elucidate mechanical activation.

For further elucidation, discussion from a microscopic point of view, as well as detailed analysis of real structure, particularly in the region finer than the limit of X-ray diffraction, seem to be of the utmost importance.

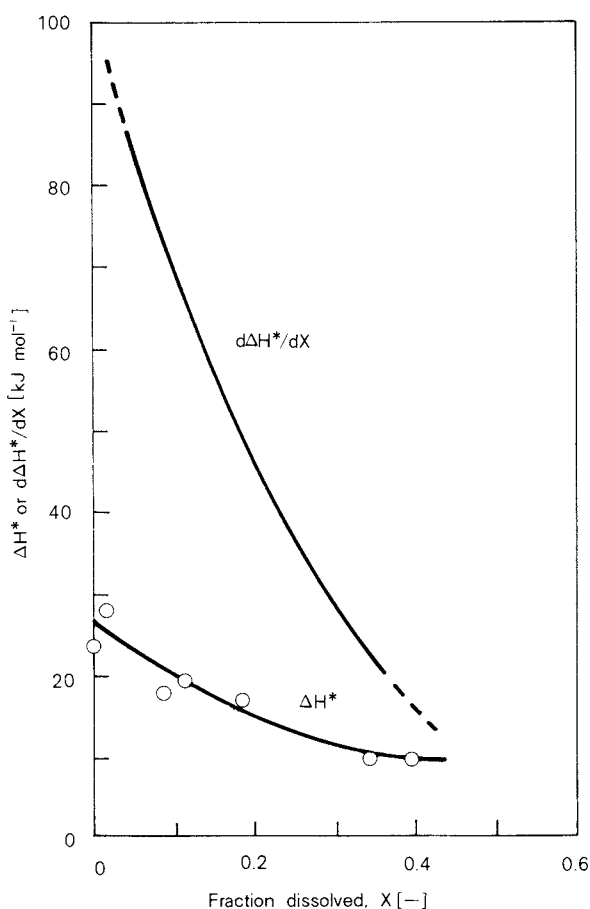


Fig. 9 Change in the excess enthalpy,  $\Delta H^*$  and  $\Delta H^*/dX$  with  $X$ , for mechanically activated lead carbonate.



## References

- 1) Senna, M.: *Kona, Powd. Sci. Technol.* **1**, 48 (1983).
- 2) Hüttig, G.F.: *Handbuch der Katalyse*, Schwab, G.M. (ed.) Band IV, p. 318, Springer, Wien 1943.
- 3) Torkar, T.: *Reactivity of Solids*, Proc. Int. Symp. deBoer, J.H. (ed.) p. 400, Elsevier, Amsterdam 1961.
- 4) Heegn, H.-P.: *Untersuchungsmethoden zur Charakterisierung mechanisch aktivierter Festkörper*, Juhász, Z. (ed.), p. 138, Közdök, Budapest, 1978.
- 5) Tkáčova, K. and H.-P. Heegn: *Banické Listy*, **9**, 43 (1984).
- 6) Imai, H. and M. Senna: *J. Appl. Phys.* **49**, 4433 (1978).
- 7) Miyasaka, K. and M. Senna: *Thermochim. Acta*, **83**, 225 (1985).
- 8) Schrader, R. and B. Hoffmann: *Z. anorg. allgem. Chem.*, **363**, 41 (1969).
- 9) Miyasaka, K. and M. Senna: *React. Solids*, **2**, 135 (1986).
- 10) Inoue, S. and M. Senna: (to be published).
- 11) Boldyrev, V.V., M. Bulens and B. Delmon: *The control of the reactivity of solids*, p. 10, 24, Elsevier, Amsterdam 1979.
- 12) Miyasaka, K. and M. Senna: *React. Solids*, (in press).
- 13) Senna, M., K. Ito and M. Machida: *Izv. Sib. Otd. Akad. Nauk USSR. Seriya Khim.*, (in press).
- 14) Bernhardt, C. and H.-P. Heegen: *Freib. Forsch.-H.*, **A602**, 49 (1978).
- 15) Steinike, U. and E. Linke: *Z. Chem.*, **22**, 397 (1978).

## Informational Articles

### The Symposium on Powder Technology

*The Party of Powder Technology (Japan)* held its 20th symposium at Sunshine Prince Hotel in Tokyo on August 28th, 1986. The Symposium was given on the theme of "The Recent Trends in Powder Technology".

Many participants (about 220) listened and discussed eagerly to the lectures for over 6 hours. The details of the lectures are listed below.

#### Session 1 Measurement of Electrostatic Charge on Particulate Materials

Chairmanship : Akira Suganuma (Science University of Tokyo)

- |  |  |
|--|--|
| • Measurement of electrostatic charge on particulate materials   | Hideo Yamamoto<br>(University of Tokyo)            |
| • Development of the instrument for particle size and electrostatic charge distribution on fine particle | Toyokazu Yokoyama<br>(Hosokawa Micromeritics Lab.) |

#### Session 2 Separation according to Particle Shape

Chairmanship : Kei Miyanami (University of Osaka Prefecture)

- |  |  |
|--|--|
| • Continuous separator of particles according to shape on (an inclined) rotating disc and its separation characteristics | Masunori Sugimoto<br>(Toyama University)                                       |
| • Shape classification of granular materials by (an inclined) rotating cylinder with blades                              | Keishi Gotoh and Masami Furuuchi<br>(Toyohashi Institute of Tech. and Science) |

#### Session 3 New Trends in Fine Grinding

Chairmanship : Toshio Inoue (University of Tokyo)

- |  |   |
|--|---|
| • Possibility and limitations in fineness in ultrafine grinding<br>– Recent trends of works of fine grinding – | Genji Jimbo<br>(Nagoya University)              |
| • Ultrafine grinding and particle preparations and design using Angmill  | Tohei Yokoyama<br>(Hosokawa Micromeritics Lab.) |



---

## Public Meeting Concerning Powder Technology Recently Held in Japan

---

### 22nd Technical meeting

promoted by the Society of Powder Technology, Japan  
held at Tokyo on June 24–25, 1987

Recent information concerning the drying operation and various problems regarding the associated field were reported and discussed.

The meeting included 15 lectures, catalogs and brochures were also displayed. The main lectures were:

- |  |  |
|--|--|
| • Drying stress on shrinkage material when dried                           | (Shinkichi Yamaguchi, Toyama University) |
| • Air-flow behavior in the spray dryer                                     | (Yuji Sano, Yamaguchi University)        |
| • Surface diffusion of adsorptive gas within porous materials              | (Morio Okazaki, Kyoto University)        |
| • Drying of granular materials using the inclined, vibrating fluidized bed | (Masanobu Hasatani, Nagoya University)   |

### 23rd Summer seminar

promoted by the Society of Powder Technology, Japan  
held at Kannami in Shizuoka prefecture on July 20–22, 1987

This seminar focused on interface phenomenon in connection with powder processing (in-

cluding 20 lectures). The main lectures were:

- |  |  |
|--|--|
| • Various problems concerning surface phenomenon                           | (Genji Jimbo, Nagoya University)                     |
| • Gas-solids interface phenomenon and particle properties                  | (Masatoshi Chikazawa, Tokyo Metropolitan University) |
| • Dispersion and aggregation of colloid in water                           | (Shinnosuke Usui, Tohoku University)                 |
| • Characteristics and application of fine-particle/liquid dense dispersoid | (Mamoru Senna, Keio University)                      |

### 3rd symposium on medicine production and particle design

promoted by the Society of Powder Technology, Japan (Particle preparation and Design Dept.)  
and  
the Association of Powder Process Industry & Engineering (Division Meeting on Particulate Modification Technology)  
held at Kobe on Nov. 27–28, 1986

This symposium focused on materials and apparatuses for particle design, and technologi-

cal development and its application (including 16 lectures). The main lectures were:

- |   |  |
|---|--|
| • Application using starch and enzymes  | (Yoshio Tsujisaka, Hayashibara Corp.)                          |
| • Preparation and application of micro-porous materials   | (Tadao Nakajima, Industrial Laboratory of Miyazaki Prefecture) |
| • Dry coating   | (Masumi Koishi, Science University of Tokyo)                   |
| • Particle-design engineering in the development of medicine production, focusing on the development of the spherical crystallization technique | (Yoshiaki Kawashima, Gifu Pharmaceutical University)           |

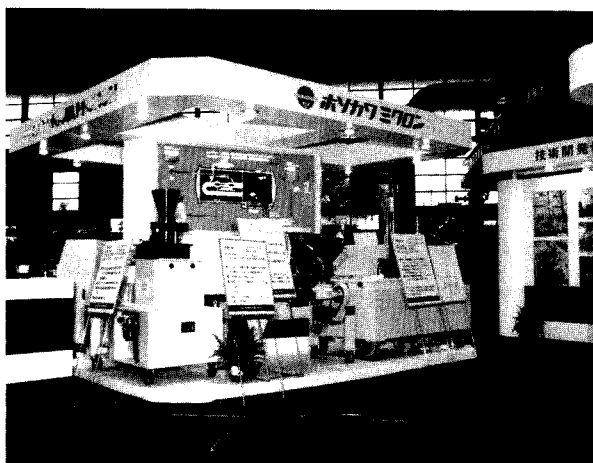
## Powdertec Japan '86

The 6th Powdertec Japan, the biennial exposition of powder processing apparatuses and equipment, was held at the International Trade Center in Harumi, Tokyo on September 16 through 20. A total of 164 exhibitors displayed their products in 635 booths – the biggest Powdertec ever held. A total of 75,000 people visited the exposition. At this show, many new and noteworthy products were displayed in specially laid-out booths, focusing on apparatuses and equipment for instrumentation measurement, and control.

On September 16 through 19, the Powder Technology Congress '86 was also held at Hotel

Urashima, located near the exhibition center, to discuss the following 6 categories in 6 individual sessions.

1. Production technology of fine particles and its trends
2. Molds for powder molding
3. Applications of ultrafine particles and the production method presently employed
4. Measurement of particle size distribution of submicron particles
5. Precision-feeding technology for the "fine technology age"
6. Worldwide trend of powder technology



Photos: Powdertec Japan '86

---

**Academic publication concerning powder technology in Japan (printed in 1986)**

---

**Journal of the Society of Powder Technology, Japan Vol. 23 (1986)**

Title	Author(s)	Page
• Optimum Radiographing Conditions Related to Powder Bulk Density	K. Makino, K. Kuramitsu, M. Yamada and J. Hidaka	3–10
• Model Bin Loads (1) The Effect of Rates of Charge on Static Wall Pressure	T. Yahiro, N. Hayano, T. Jotaki and J. C. Williams	11–17
• Noncrystallization of Chloramphenicol Palmitate Crystals by Grinding and Its Mechanism	M. Otsuka and N. Kaneniwa	63–67
• Countermeasure for Dust Deposited in a Sampling Tube	N. Kogure, H. Yoshiyama, I. Tamori, T. Saito and K. Watanabe	68–75
• The Optimum Design of a Solid-Solid Reaction System	Y. Hao and T. Tanaka	152–155
• Measurement of Powder Yield Locus by the Constant Volume Type Direct Shear Tester	T. Nomura and Y. Misaki	156–163
• Model Bin Loads (2) The Effect of Discharge Rates on Dynamic Pressure	T. Yahiro, N. Hayano, T. Jotaki and J. C. Williams	231–239
• The Fundamental Equations of the Dynamic of Granular Materials with Intergrain Adhesive Forces	T. Nagao	240–249
• Mechano-chemical Effect of One-dimensional Explosively Shocked Treatment on the Characteristics of $\text{Si}_3\text{N}_4$	F. Ikazaki, K. Kamiya, K. Uchida, A. Goto, M. Kawamura, K. Tanaka and S. Fujiwara	250–257
• Development of a Continuous Tumbling Fluidized Bed Coater and Its Characteristics	E. Abe and H. Hirose	319–325
• Spontaneous Ignition of Dust Deposits – Ignition Temperature and Induction time –	H. Liang, T. Tanaka and Y. Nakajima	326–331
• Morphological Characteristics of $\text{Si}_3\text{N}_4$ and SiC Raw Powder for Sintering	K. Suzuki and Y. Kuwahara	401–407
• A Technique for Measuring Wide Size Ranges of Aerosol Particles by the Laser Beam Scattering Method Combined with Condensation Nuclei	S. Okuda, H. Takano and T. Iwamoto	408–414
• Correction for Particle Concentration in Centrifugal Sedimentation Method	K. Takeuchi	415–421
• Measurement of Zeta Potential of Fine Particles by Microelectrophoresis and TV-Visualization System	T. Niida, M. Yamada, Y. Kouno and Y. Kousaka	422–429
• Development of a New Measuring Method for Size Distribution of Fine Powder Using Pressure Difference Sensor	G. Jimbo, J. Tsubaki, Q. Zhao, H. Tanaka, and Y. Sakurai	430–436
• The Effect of a Flat Plate Held Normal to the Wall on Solid Particle Motion	H. Ueno and Y. Kano	487–492
• The Effect of the Wake Behind a Flat Plate Normal to the Flow of Solid Particle Motion (for Kármán vortex)	H. Ueno and Y. Kano	493–499
• The Effect of an Ultra-Fine Solid Additive on the Tensile of a Powder Bed	M. Naito, N. Kato, G. Jimbo and T. Yokoyama	500–506
• Experimental Research on Critical Bridging Span for Silo – Part 2: Test Report on Coal with Large Model Silo –	M. Kato, T. Yamada, T. Tamura and H. Haze	561–570
• The High Density Pneumatic Conveyance of Solid Plugs (1st Report Friction Force)	H. Ueno and Y. Kano	571–577



Title	Author(s)	Page
• The High Density Pneumatic Conveyance of Solid Plugs (2nd Report Powder Efficiency)	H. Ueno and Y. Kano	578–584
• The Performance of a Cyclone with an Eccentric Outlet Pipe	H. Yamamoto and R. Utsumi	585–591
• The Evaluation of Mixedness by Run Length between Sought Particles	H. Watanabe and E. Obata	629–635
• Flocculation Studies of Agglomerated Stearylalcohol Particles on the Surface of the Water	H. Sunada, Y. Hirai and A. Otsuka	636–640
• The Friction Coefficient of Fused Alumina Due to Wall Material	H. Yamamoto, R. Utsumi and A. Kushida	641–646
• Electric Resistance as a Measure for Estimating the Randomness of a Finary Solid Particles System (Parallelism)	H. Iyi and Y. Yoshimura	647–654
• The Influence of an Additive Amount of Colloidal Silica on the Flowability and Drift Characteristics of Solid Formation	H. Hirosue, E. Abe and N. Yamada	655–660
• The Effect of Shape and Diameter of Particles on the Frictional Behavior of a Powder Bed	M. Hirota, T. Ishihara, A. Sugai and T. Oshima	661–664
• The Preparation of Ultrafine Zirconium Carbide Powder from Zirconium Oxide by Reduction with Magnesium	K. Yamane, S. Kida, T. Mori, T. Iida and T. Mitamura	665–670
• The Preparation of Antimony-doped Stannic Oxide Ultrafine Particles Using a Gas-phase Chemical Reaction	K. Kim and A. Yoshizawa	671–677
• Comparing the Flow Properties of Bulk Solids by Tri-axial Shear Tests, Unconfined Yield Tests and Direct Shear Tests	H. Tsunakawa, D. Kunii, F. Takagi, M. Sugita, T. Tamura and H. Haze	678–684
• Computer Simulation of Agglomeration with Compaction	Y. Kawashima, T. Handa, H. Takeuchi, K. Niwa, H. Sunada and A. Otsuka	685–689
• The Dust Collection Performance of a Return Flow Long-body Cyclone	N. Kimura	713–718
• The Agglomeration Mechanism of Phenytoin (Antiepileptic) by a Novel Agglomerated Crystallization Technique	Y. Kawashima, T. Handa, H. Takeuchi and M. Okumura	719–729
• The High Density Pneumatic Conveyance of Solid Plugs (3rd Report Horizontal Bend)	H. Ueno and Y. Kano	730–737
• The High Density Pneumatic Conveyance of Solid Plugs (4th Report Inclined Pipe)	H. Ueno and Y. Kano	775–783
• The Transitional Behavior of the Mechanical Properties of a Powder Bed Prepared by Various Compressive Histories	H. Kamiya, N. Kishi, J. Tsubaki and G. Jimbo	832–838
• Porosity Estimation for a Multi-Size-Component Mixture	N. Ouchiyama and T. Tanaka	839–844
• The Capillary Rising Mechanism in a Packed Bed of Spherical Particles	M. Nakagawa, M. Furuuchi, K. Miwa and K. Goto	845–849
• On the Stress Distribution of Granular Materials Conically Piled on the Field	T. Nagao, Y. Hatamura, T. Takeuchi and N. Nakajima	850–856
• Spectral Analyses of the Pressure Wave Generated by the Flow of Granular Materials – A Case Study on a Small Scale Silo –	H. Okamoto	857–864

Title	Author(s)	Page
• Mixing and Flow Characteristics of Alumina – Thermoplastic Resins – Effect of the Change of Resin Properties during Heating and Mixing –	M. Takahashi and S. Suzuki	865–870
• Particle Size Segregation to Enhance Gas Permeability in a Bed of Iron Ore-Sintering Machine	S. Mizukami, T. Maehana and H. Murata	871–876
• The Packing Structure of Dry Pressed $\text{Si}_3\text{N}_4$ Powder	K. Suzuki and Y. Kuwahara	877–881
• The Stress-Strain Relationship in Powder	S. Yuu, S. Nakamura and T. Furusawa	882–888
• The Influence of the Packing Fraction on the Over-Pressure Ratio of Atomized Metal Powder Beds	K. Tanno and S. Yashima	889–895
• Pressure Fluctuation in a Coal Hopper	H. Murata and M. Wakabayashi	896–899

#### Funsai (The Micromeritics) No. 31 (1987)

Title	Author(s)	Page
• The Pressure Ride due to Dust Explosion of Calcium Silicide	X. Deng and J. Yan	4–10
• A New Instrument to Measure the Penetration Rate of the Liquid	M. Koishi, N. Kaya, T. Yokoyama and H. Kitai	11–14

#### Kagaku Kogaku Ronbunshu Vol. 12 (1986)

Title	Author(s)	Page
• Power Consumption and Flow Rate of a Three-Roll Mill	Y. Murakami, G. Chung, T. Tenda and Y. Akimoto	23–29
• Pulsating Wall Pressure Occurring at Hopper Section in a Bin	R. Moriyama and G. Jimbo	63–68
• Study on Application of Vibratory Motion to Conveying Granular Materials – Effect of Vibration on Movability of Granular Materials–	F. Takeuchi, T. Kano, R. Aiura and N. Shibata	97–101
• Study on Application of Vibratory Motion to Conveying Granular Materials – Effect of Vibration on Inclined Conveying Duct –	F. Takeuchi, T. Kano, T. Yamada and T. Maeda	102–106
• Effect of Ball Size on Grinding Rate of Planetary Ball Mill	M. Kuriyama, T. Honma and Y. Kanda	116–119
• Classification of Fine Particles by Sonic-Fluidized Bed with Stirrer	K. Kato, K. Ebara, S. Takahashi, M. Tanizawa and H. Ueno	140–145
• Generating Mechanism of Sound in Shear Flow of Granular Materials	J. Hidaka and S. Miwa	192–198
• Measurement of Mechanical Strength of Aggregates by Rod Penetration Method	N. Hayashi, M. Iwata, S. Uemura, T. Murase and M. Shirato	294–300

Title	Author(s)	Page
• Surface Profile and Internal Structure of Particle Bed Formed by Deposition of Aerosol Particles	S. Ikumi, H. Mori and and H. Masuda	382–387
• Improvement of the Estimation Method for the Yield Locus of Powders Based on the Powder Yield Model	M. Yamada, K. Kuramitsu and K. Makino	408–413
• Characteristics of Fluidized Bed under Oscillation	Y. Nishi	414–419
• Effect of Solid Additives on Displacement and Energy Required to Split Powder Bed	M. Naito, S. Usuda and G. Jimbo	495–497
• Particle Reentrainment by an Air Stream from Deposited Layer	S. Ikumi, H. Wakayama and H. Masuda	589–594
• Measurement of Particle Size Distribution by Numerical Values of Fluidization Curve	E. Obata, H. Watanabe, K. Mukaida, M. Akiyoshi and K. Ando	619–621
• Aperture Size in a Screen of Plain Dutch Weaves	H. Yamamoto, R. Utsumi and A. Kushida	635–639

**Journal of the Society of Material Science, Japan Vol. 35 (1986)**

Title	Author(s)	Page
• Submicron Grinding of BaTiO <sub>3</sub> by Ball Milling	K. Tanaka, K. Minai, K. Wakino and I. Uei	54–58
• Fine Particle Classification and Identification by Using Glow Discharge	T. Kurobe, O. Imanaka and M. Ikeno	664–668
• Continuous Mulling of Conductive Materials	K. Terashita, H. Tsukaguchi and K. Miyanami	1229–1233
• A Model of Mixing of Two Groups of Particles with Different Electric Resistance	Y. Fujihara and Y. Yoshimura	1240–1245
• Aggregate Structure of Fine Particles and Compacting Process	M. Arakawa, T. Kitamura, Y. Tokuoka, H. Morii and H. Kinoshita	1246–1250
• Mixing and Flow Properties of Alumina-Polypropylene Mixture System	M. Takahashi, S. Suzuki and H. Arai	1251–1256
• Surface-Treatment of Cermet Powder and its Surface Properties	N. Suzuki, A. Endo and H. Utsugi	1257–1262

**Journal of the Japan Society of Powder and Powder Metallurgy Vol. 33 (1986)**

Title	Author(s)	Page
• Refraction Condition of a Loose Bulk Density Zone through the Interface between Two Different Powders	K. Makino, M. Yamada, A. Higashiyama and K. Kuramitsu	232–239
• Change and Control of Sintering Behavior of Fine Alumina Powders by Preliminary Grinding	M. Kume and M. Senna	344–347

Hosokawa Micron Corp. presents three of its new products.

### MECHANOFUSION SYSTEM

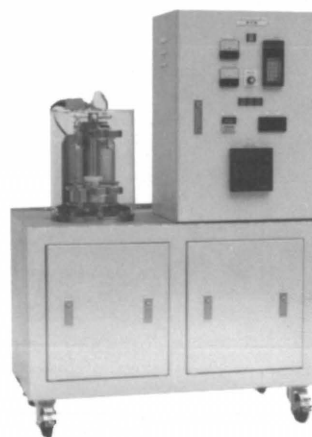
Mechanofusion® is a novelty technology for creation of new particulate materials. By generating mechano-chemical reaction upon two or more materials, they turn out to be a new material that has new physical and chemical properties. The Mechano-fusion process can be applied for a variety of combinations of particulate materials.

Power required : 1.5 – 55 kW

Capacity : 0.2 – 45 kg/Hr

Features:

- Producing functional particulate materials
- Powerful disintegration and blending
- Capable of controlling particle size and form



### E-SPART ANALYZER

Measuring apparatus for electrostatic charge distribution of particle

Measuring method : Laser Doppler method for simultaneous measurement of particle size and charge

Measurement range : 1.7 – 26  $\mu\text{m}$

Features:

- Capable of simultaneously measuring particle size and charge distributions quickly.
- Easy specimen replacement
- Bi-polarity data in one measuring sample
- An automatic calibration system



### MICRON SEPARATOR EXCELLENT

Classifier

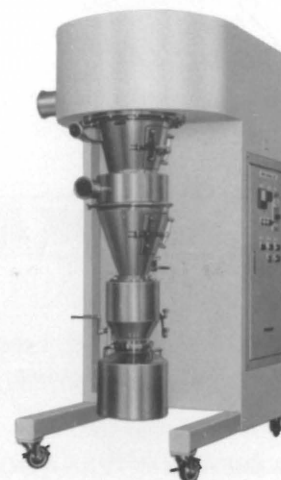
Power required : 0.75 – 37 kW

Capacity : 30 – 1000 kg/Hr

Classification range : 3 – 300  $\mu\text{m}$

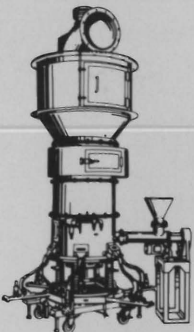
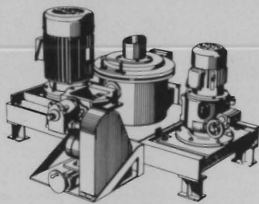
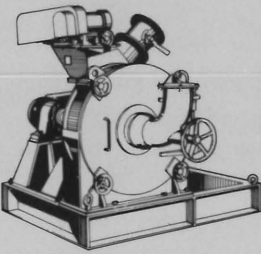
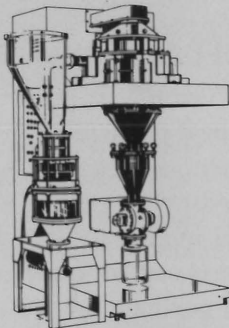
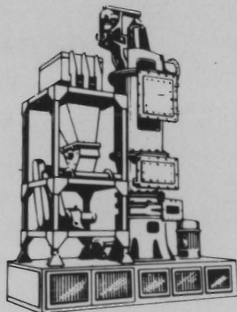
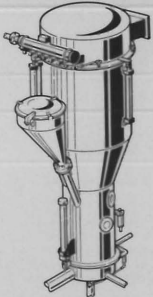
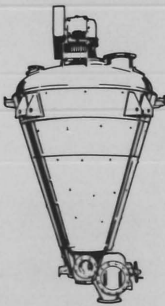
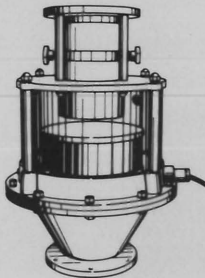

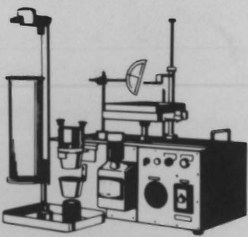
Features:

- Easy control of separation points
- Broad classification range for diversified products
- Accurate separation provides quick and efficient recovery of required products from process materials.



# LEADER OF POWDER PROCESSING TECHNOLOGY

# HOSOKAWA

				
Ultra-fine pulverizing Micron Jet	Fine-grinding ACM Pulverizer	Fine-grinding Fine Victory Mill	Classifying Super Separator	Drying Micron Dryer
				
Drying Fluid Bed Processor	Mixing/Drying Nauta Mixer-Reactor	Feeding/Discharging Flo-tron	Dust collection Pulsaire Collector	Measurements Powder Characteristics Tester

## From a Single Unit to Complete Treatment System

Hosokawa has specialized in powder processing technology for 70 years. Today, Hosokawa makes a complete line of advanced equipment for fine-grinding, classifying, drying, mixing, dust collection, measurement and so on. Yet, Hosokawa's most distinguished feature is its capability of

the system engineering that will satisfy a wide variety of industrial needs. Hosokawa has diversified marketing and manufacturing organizations located throughout the world. Whenever you have a problem, planning, or project relating to powders, first consult with Hosokawa.

## HOSOKAWA MICRON CORPORATION

### International Sales Division.

No. 9, 1-chome, Shoudai Tajika, Hirakata-shi, Osaka 573 Japan  
Telephone: 0720-56-6751 Facsimile: 0720-68-1309

**HOSOKAWA MICRON INTERNATIONAL INC.**  
780 Third Avenue, New York, NY 10017, U.S.A.  
Telephone: 212-826-3830 Facsimile: 212-826-6612

**HOSOKAWA MICRON EUROPE B.V.**  
Industriestraat 25, 7005 AN Doetinchem, Holland  
Telephone: 08340-4-1188 Facsimile: 08340-2-5662